

5-1999

The origin of brucite in hydrothermally altered limestone near Devil Peak, Nevada

Rhonda L. Knupp
University of Nevada, Las Vegas

Follow this and additional works at: <https://digitalscholarship.unlv.edu/thesesdissertations>



Part of the [Geochemistry Commons](#), and the [Geology Commons](#)

Repository Citation

Knupp, Rhonda L., "The origin of brucite in hydrothermally altered limestone near Devil Peak, Nevada" (1999). *UNLV Theses, Dissertations, Professional Papers, and Capstones*. 1450.
<http://dx.doi.org/10.34917/3434883>

This Thesis is protected by copyright and/or related rights. It has been brought to you by Digital Scholarship@UNLV with permission from the rights-holder(s). You are free to use this Thesis in any way that is permitted by the copyright and related rights legislation that applies to your use. For other uses you need to obtain permission from the rights-holder(s) directly, unless additional rights are indicated by a Creative Commons license in the record and/or on the work itself.

This Thesis has been accepted for inclusion in UNLV Theses, Dissertations, Professional Papers, and Capstones by an authorized administrator of Digital Scholarship@UNLV. For more information, please contact digitalscholarship@unlv.edu.

THE ORIGIN OF BRUCITE IN HYDROTHERMALLY ALTERED
LIMESTONE NEAR DEVIL PEAK, NEVADA

by

Rhonda L. Knupp

Bachelor of Science
Sonoma State University
1994

A thesis submitted in partial fulfillment
of the requirements for the

**Master of Science Degree
Department of Geoscience
College of Sciences**

**Graduate College
University of Nevada, Las Vegas
May 1999**

©1999 Rhonda Lee Knupp
All Rights Reserved



Thesis Approval
The Graduate College
University of Nevada, Las Vegas

April 8, 19 99

The Thesis prepared by

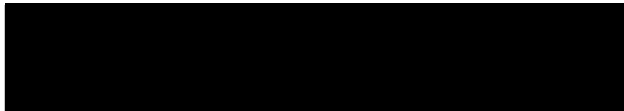
Rhonda Knupp

Entitled

The Origin of Brucite in Hydrothermally Altered Limestone near
Devil Peak, Nevada

is approved in partial fulfillment of the requirements for the degree of

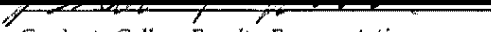
Master of Science in Geoscience


Examination Committee Chair


Dean of the Graduate College


Examination Committee Member


Examination Committee Member


Graduate College Faculty Representative

ABSTRACT

The Origin of Brucite in Hydrothermally Altered Limestone Near Devil Peak, Nevada

by

Rhonda Knupp

Dr. Rodney Metcalf, Examination Committee Chair
Associate Professor of Geology
University of Nevada, Las Vegas

Open-space brucite was identified in veins crosscutting hydrothermally altered limestone near the Devil Peak rhyolite plug in southern Nevada. The brucite occurs with serpentine, calcite, chalcedony, hydromagnesite, dolomite, and clinocllore.

Brucite usually forms as a replacement mineral, but textural evidence indicates that the brucite at Devil Peak precipitated in open space. The presence of chalcedony in veins indicates the temperature of the hydrothermal fluid was $< 180^{\circ}\text{C}$ during and after mineral deposition. Thermodynamic modeling shows this temperature is too low for replacement brucite to form, thus the low temperature of alteration may be a factor in this unusual occurrence of brucite.

Infiltration modeling of isotopically depleted wall rocks shows that the hydrothermal fluid was initially composed of a mixture of metamorphic and meteoric water, with $X_{\text{CO}_2} = 0.15\text{-}0.16$. Later, an influx of magmatic fluid or metamorphic water

mixed with the early fluid. Fluid inclusion analysis shows $X_{\text{CO}_2} < 0.01$ for the fluid mixture.

TABLE OF CONTENTS

ABSTRACT	iii
LIST OF TABLES	viii
LIST OF FIGURES	ix
ACKNOWLEDGMENTS	xii
CHAPTER 1 INTRODUCTION	1
Introduction and Purpose	1
CHAPTER 2 RESEARCH METHODS AND ANALYTICAL TECHNIQUES	5
Research Methods	5
Analytical Techniques	6
Thin Sections	6
Fluid Inclusion Analysis	7
Thermodynamic Modeling	7
Stable Isotope Studies	8
Whole-Rock X-Ray Fluorescence Analysis	10
X-Ray Diffraction Analysis	10
CHAPTER 3 GEOLOGY OF THE DEVIL PEAK AREA	13
Regional Geology	13
Lithology	13
Structure	14
Previous Work	14
Major Findings by Walker et al. (1980)	15
Geology of the Field Area	16
Lithology	16
Structure	18
Alteration	19
CHAPTER 4 PETROGRAPHY AND PARAGENESIS	26
Description of Vein Minerals	26
Relative Abundances of Minerals	27
Open-Space and Replacement Minerals at Devil Peak	27
Paragenetic Sequence	29

CHAPTER 5	FLUID INCLUSION ANALYSIS	35
	CO ₂ and Salt Content of the Fluid	35
	Homogenization Temperatures and P-T Behavior of the Hydrothermal Fluid	36
	Summary and Conclusions	38
CHAPTER 6	THERMODYNAMIC MODELING	43
	Estimation of Pressure, Temperature, and X _{CO2}	43
	Significance of Chalcedony	43
	Pressure and X _{CO2}	44
	Temperature-X _{CO2} Diagrams	44
	Mineral Stability Diagrams	46
	Conditions of Mineral Precipitation	46
	Hydrothermal Fluid Composition and Evolution	47
	Implications of Thermodynamic Modeling Results	48
	Summary and Conclusions	49
CHAPTER 7	STABLE ISOTOPE ANALYSIS	56
	Preliminary Interpretation of Results	56
	Sample Groups	56
	Relationships Among Sample Groups	57
	Mg-Metasomatism	57
	Possible Explanations for the Stable Isotope Signatures	57
	Possible Explanations for the Depletion Trend	57
	The Mass-Balance (Box) Model for Isotope Exchange During Infiltration	61
	Implications of Modeling Results for Origin of Vein Calcites	68
	Hydrothermal Fluid Source and Evolution	69
	Mg Source	71
	Summary and Conclusions	72
CHAPTER 8	SUMMARY AND CONCLUSIONS	91
	Hydrothermal Alteration at Devil Peak	91
	Presence of Open-Space Brucite at Devil Peak	91
	Conditions of Alteration at Devil Peak	92
	Temperature	92
	Hydrothermal Fluid Composition	92
	Hydrothermal Fluid Source and Evolution	93
	Possible Explanations for Rare Brucite Occurrence	93
APPENDIX I	SAMPLE LIST	95

APPENDIX II	CONSTRUCTION OF THERMODYNAMIC DIAGRAMs	99
	The Equation for Gibbs Free Energy at Elevated Temperature and Pressure	100
	Heat Capacity	106
	Fugacity	107
	Temperature- X_{CO_2} Diagrams	112
	Mineral Stability Diagrams	114
APPENDIX III	STABLE ISOTOPE MODELING	116
	Relationship Between F_{carbon} and F_{oxygen} in Silicate-Absent Rayleigh	
	Decarbonation	116
	The Mass-Balance Equation and Fluid-to-Rock Ratios	117
	Derivation of the Open System Equation for Fluid-to-Rock Ratios	117
	Infiltration Modeling	118
	Calculating the Depleted Signatures	118
	The Modeling Method	120
	Calculating the Isotopic Signatures of Hypothetical Vein Calcites	121
REFERENCES CITED		122
VITA		127

LIST OF TABLES

Table 3-1	Results of X-ray diffraction analysis of Devil Peak samples	25
Table 4-1	Mineral assemblages in vein thin sections that contain other minerals in addition to calcite	32
Table 5-1	Results of fluid inclusion analysis of DPL26.	39
Table 7-1	Results of C and O stable isotope analysis of Devil Peak samples	75
Table 7-2	Results of X-ray fluorescence analysis of Devil Peak limestone and altered limestone samples	78
Table 7-3	F_{carbon} (fraction of carbon) remaining in wall rock samples	80
Table 7-4	Stable isotope signature and X_{CO_2} of early infiltrating fluid estimated by mass-balance modeling	83
Table 7-5	Calculated $\delta^{13}\text{C}$ signatures of hypothetical vein calcites deposited by the modeled infiltrating fluids	85
Table 7-6	Calculated isotopic signatures of fluid in equilibrium with vein calcite samples at 100°C and 200°C	87
Table 7-7	Established ranges of $\delta^{13}\text{C}$ and $\delta^{18}\text{O}$ values for the three possible sources of hydrothermal fluid at Devil Peak	89
Table I-I	Sample list	96

LIST OF FIGURES

Figure 1-1	Location of Devil Peak, and other Tertiary volcanic and intrusive rocks in the Spring Mountains.	3
Figure 1-2	Location of Devil Peak and nearby geologic features.	4
Figure 2-1	(a) Typical fluid inclusion in sample DPL26, and (b) the growth-zoned calcite crystal that contains it	12
Figure 3-1	Boundary faults related to the intrusion of the Devil Peak plug	23
Figure 3-2	Thin dikes of gray rhyolite (Tvg) that intruded dolomitized limestone near the eastern adit	24
Figure 3-3	Large fault separates the gray rhyolite dike (Tvg) from the altered Monte Cristo Limestone (Mma)	24
Figure 4-1	Brucite laths	30
Figure 4-2	Vein containing banded chalcedony	30
Figure 4-3	Netlike texture in serpentine	31
Figure 4-4	Hydromagnesite needles	31
Figure 4-5	Photomicrographs of brucite replacement textures from Carpenter (1967). (a) Pseudomorph of "onion-skin" brucite after periclase. (b) Pseudomorph of platy brucite after dolomite	33
Figure 4-6	Brucite laths and hydromagnesite needles that grew in open space in a vug	34
Figure 4-7	Vug containing symmetrical bands of calcite and chalcedony, with brucite and hydromagnesite filling in the center	34
Figure 5-1	Final ice melting temperatures in fluid inclusions	41
Figure 5-2	Fluid inclusion homogenization temperatures	41

Figure 5-3	Sketch of growth-zoned crystal from chip A3, showing homogenization temperatures (in °C) from fluid inclusions in different growth zones	42
Figure 5-4	Sketch of growth-zoned crystal from chip B4, showing homogenization temperatures (in °C) in groups of fluid inclusions from different growth zones	42
Figure 6-1	T- X_{CO_2} diagram at P = 1 bar	51
Figure 6-2	T- X_{CO_2} diagram at 100 bars	52
Figure 6-3	Mineral stability diagram at 1 bar, X_{CO_2} = 0.01, and various temperatures	53
Figure 6-4	Mineral stability diagram at 100 bars, X_{CO_2} = 0.01, and various temperatures	54
Figure 6-5	Mineral stability diagram at 100 bars, X_{CO_2} = 0.1, and various temperatures	55
Figure 7-1	Results of stable isotope analysis of Devil Peak samples	76
Figure 7-2	Important relationships among sample groups	77
Figure 7-3	Silicate-absent Rayleigh decarbonation trend calculated at 200°C, 300°C, and 500°C	79
Figure 7-4	Measured $\delta^{13}\text{C}$ and $\delta^{18}\text{O}$ depletion trends from 17 stable isotope studies	81
Figure 7-5	Curves representing modeled $\delta^{13}\text{C}$ and $\delta^{18}\text{O}$ depletions in wall rock signatures caused by infiltration at 300°C in (a) open and (b) closed systems	82
Figure 7-6	Decrease in curvature of modeled wall rock signatures with increase in X_{CO_2} of infiltrating fluid	84
Figure 7-7	Comparison of isotopic signatures of vein calcite samples with the signatures hypothetical vein calcites would have if deposited by the modeled infiltrating fluid at low temperatures	86
Figure 7-8	Modeled isotopic signature range of infiltrating fluid that depleted the wall rock, and calculated isotopic signature range of the fluid that deposited the vein calcites	88

Figure 7-9	Possible sources of the hydrothermal fluid at Devil Peak	90
------------	--	----

ACKNOWLEDGMENTS

I am indebted to the Geological Society of America and the UNLV Graduate Student Association for the financial support that made this thesis possible. Bernada E. French (Scholarship), the Scroungers (Scholarship), and the UNLV Graduate College (Barrick Fellowship) all provided subsistence funding, for which I am very grateful.

I wish to thank Dr. Rod Metcalf, my advisor, for his guidance and enthusiasm, especially during the numerous chats about the direction this thesis was taking, and for his valuable editorial comments on the endless drafts I handed him. I also wish to thank my other committee members, Dr. Jean Cline, Dr. Gene Smith, and Dr. Brett Riddle, for their guidance and helpful suggestions. A special thank you to Gene Smith for introducing me to my thesis topic, and to Jean Cline and Dr. Fred Bacchuber for finding me employment. Thank you to all of the UNLV professors and staff who always dropped what they were doing to answer my questions.

I am much obliged to Dr. Bill Blackburn of the University of Windsor, Ontario, for poring over the XRD samples I sent him and sorting out what they were, and to Dr. Andy Campbell and the rest of the folks at the New Mexico Tech Stable Isotope Lab, who cheerfully analyzed my samples even though I sent them only a few at a time. Thanks also to Dr. Clay Crow for helping me with the XRD at UNLV.

I'd like to thank Viceroy International Exploration and especially my friend Beth Scott for providing me with an interesting and valuable learning experience that also paid me money. For Beth's patient instruction and encouragement I am eternally grateful.

Thank you, Mom and Dad, for your continued encouragement and faith in me and for your financial support. Thanks also to my good friend Tom for all the fun times, and to the rest of the old Friday Lunch Club for those much-needed, jovial two-hour breaks.

And finally, thanks to my dearest friend Joe, who saw me through rough times (lost cats and broken-down trucks) and good times (camping and mineral collecting trips), and all the times in between.

CHAPTER 1

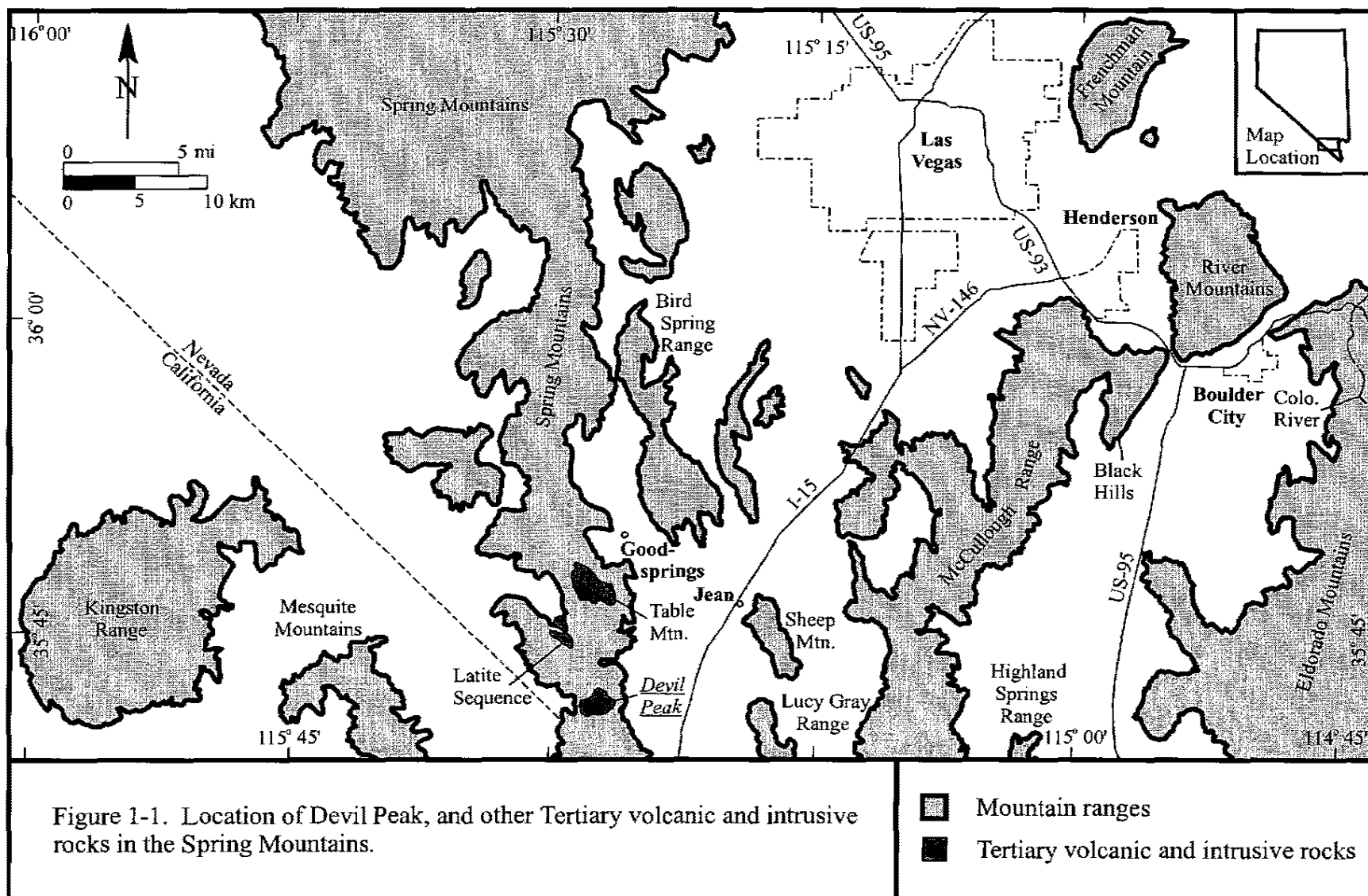
INTRODUCTION

Introduction and Purpose

Devil Peak is a mid-Miocene (12.6 Ma) shallow rhyolite plug that intruded Paleozoic carbonate rocks in the southern Spring Mountains near Jean, Nevada (Figures 1-1 and 1-2). A prominent fault trends northeast through the Mississippian Monte Cristo Limestone, subparallel to the southeast margin of the plug (plate 1). A large, northeast-trending rhyolite dike forms the hanging wall of the fault. Near the fault and dike, the Monte Cristo Limestone has undergone extensive hydrothermal alteration. Two relatively large areas and numerous small pods of limestone are bleached white. Within the large bleached areas, two small zones of limestone are densely fractured, dolomitized, and crosscut by mineralized veins containing brucite, calcite, serpentine, chalcedony, hydromagnesite, dolomite, and clinochlore.

Brucite ($\text{Mg}(\text{OH})_2$) is a rare mineral that is known to form by replacement of other minerals, but textural evidence in thin sections of the veins at Devil Peak suggests that the brucite precipitated directly from solution in open space. Occurrences of brucite that formed by precipitation are extremely uncommon, and literature describing open-space brucite is accordingly scarce. Most references either state that brucite is a secondary mineral, or do not address its origin.

The purpose of this study is to establish whether brucite at Devil Peak is an open-space or replacement mineral, determine the conditions under which open-space and replacement brucite form, characterize the hydrothermal system that deposited brucite and the other minerals in veins, and, if brucite is open-space filling, explain why it occurs at Devil Peak. The research will focus on describing the geologic setting of the hydrothermal system, as well as estimating the temperature, chemical and isotopic composition, and source of the hydrothermal fluid.



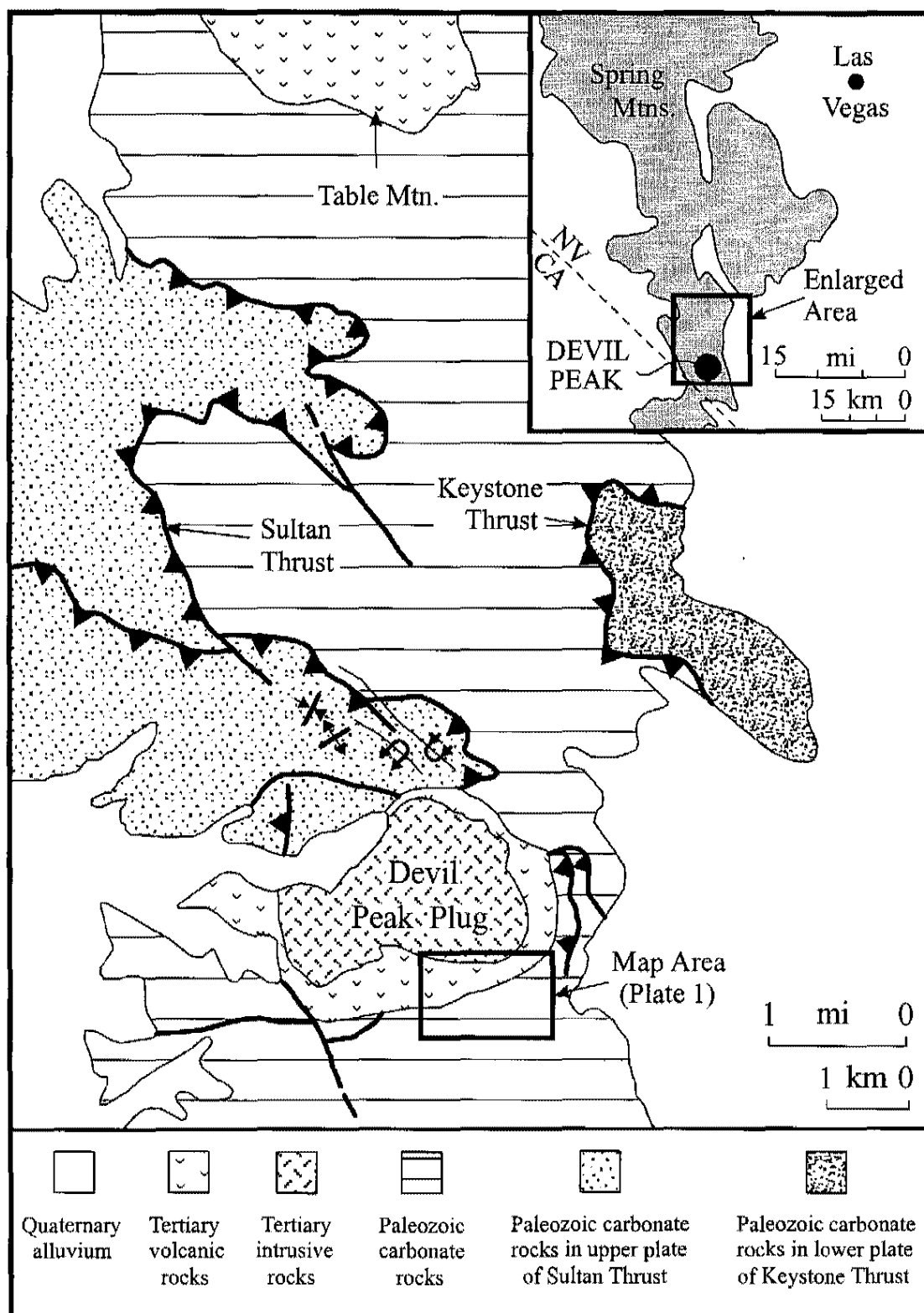


Figure 1-2. Location of Devil Peak and nearby geologic features. Modified from Walker et al. (1980).

CHAPTER 2

RESEARCH METHODS AND ANALYTICAL TECHNIQUES

Research Methods

To determine whether brucite is an open-space filling or replacement mineral at Devil Peak, thin sections of the veins were examined in detail for open-space filling and replacement textures. To determine the temperature, pressure, and fluid composition conditions under which open-space and replacement brucite form, temperature- X_{CO_2} diagrams and mineral stability diagrams were constructed from published thermodynamic data. The temperature- X_{CO_2} diagrams indicated the temperature, pressure, and X_{CO_2} conditions under which brucite replaces other minerals, and the mineral stability diagrams showed the pressure, temperature, and fluid composition conditions under which brucite precipitates from solution into open space. Characterizing the hydrothermal system that deposited the brucite and other minerals in veins at Devil Peak involved three major tasks, described in detail below.

- (1) Determining the areal extent of the alteration, locating any igneous rocks and structures in the area that may be responsible for or facilitate the alteration, and searching for possible sources of Mg^{2+} ; accomplished by detailed geologic mapping of

the southeast Devil Peak area at a scale of 1:6000, and by X-ray fluorescence spectrometry, which was used to monitor variations in Mg concentration with increasing alteration.

(2) Establishing the mineralogy and paragenetic sequence of the veins; accomplished by a petrographic study in conjunction with X-ray diffraction analysis.

(3) Determining the temperature, X_{CO_2} , and chemical composition and of the hydrothermal fluid; accomplished using thermodynamic modeling, fluid inclusion analysis, and stable isotope analysis. The temperature- X_{CO_2} diagrams and mineral stability diagrams showed the temperature and composition of the hydrothermal fluid required for the formation of the minerals present at Devil Peak. Fluid inclusion analysis provided additional insight into the temperature and X_{CO_2} of the hydrothermal fluid. Stable isotope analysis and infiltration modeling were also used to estimate the X_{CO_2} of the hydrothermal fluid, and to identify possible fluid sources.

Analytical Techniques

Thin Sections

Fifty-eight thin sections of unaltered limestone, partly altered limestone, highly altered limestone, highly altered veined limestone, and rhyolite were prepared and examined at the University of Nevada, Las Vegas.

Fluid Inclusion Analysis

Quality Thin Sections (QTS) of Tucson, AZ, prepared two doubly polished thick sections from sample DPL26, a calcite vein. Due to the cloudiness of the calcite, the sections are only 60 μm thick rather than the standard 100 μm . At the University of Nevada, Las Vegas, 47 fluid inclusions were analyzed using a Fluid, Inc. gas-flow heating and freezing stage on a Nikon Optiphot-2 microscope. The thick sections were broken into chips ≤ 0.5 cm in size for use in the stage. Synthetic CO_2 - H_2O fluid inclusions made by Syn Fline, Inc. were used to calibrate the stage at -56.6°C (solid CO_2 melting temperature) and 374.1°C (critical temperature of water). The stage was calibrated at 0.0°C using an ice and water mixture.

All inclusions measured were determined to be primary based on their presence within a growth zone (Figure 2-1). The inclusions all contained liquid and a small vapor bubble, had similar liquid to vapor ratios, and homogenized to liquid. Because ice crystals were not visible, the temperature of final ice melting was taken when the vapor bubble suddenly enlarged and did not shrink on refreezing. During homogenization and final ice melting temperature measurements, the cycling technique (Goldstein and Reynolds, 1994) was used to ascertain the physical change of the bubble.

Thermodynamic Modeling

The FORTRAN program THERMOCALC (Holland and Powell, 1990) was used to calculate most of the reactions on the temperature- X_{CO_2} diagrams. The mineral stability diagrams and one reaction on the temperature- X_{CO_2} diagrams were constructed using Excel and Mathematica with the Compensated Redlich-Kwong, or CORK, equation of

state of Holland and Powell (1991). To maintain internal consistency in the calculations, the thermodynamic data set that Holland and Powell used to calibrate the CORK equation was used whenever possible (Appendix II). THERMOCALC also uses the CORK equation of state.

Stable Isotope Studies

The mass-balance equations of Taylor (1974, 1977) were used to model isotopic changes in the wall rock caused by circulating hydrothermal fluid, and to estimate the X_{CO_2} and stable isotope signature of the hydrothermal fluid. The modeled isotopic signature of the fluid was then used to estimate the fluid source.

Eleven wall rock samples and three vein calcite samples were sent to the stable isotope lab of the New Mexico Institute of Mining and Technology for O and C stable isotope analysis of calcite. The results were reported relative to PDB for $\delta^{13}\text{C}$ and SMOW for $\delta^{18}\text{O}$. The standard deviation was $\leq 0.150\text{‰}$ for $\delta^{13}\text{C}$ and $\leq 0.164\text{‰}$ for $\delta^{18}\text{O}$. Ten of the wall rock samples were also sent to Chemex Labs for whole-rock, major element X-ray fluorescence analysis.

Sample Preparation

Fresh samples were broken to ≤ 4 cm in the field then placed into labeled Ziploc freezer bags. Portions of the sample that were exposed at the surface were removed and discarded in the field. In the lab, the sample was crushed to ≤ 0.5 cm using a Bico Chipmunk, then ground in a Bico Rotary Disk Mill with the plates adjusted approximately 2 cm apart. The resulting sample was poured into the top of a stack of 30 mesh, 60 mesh,

80 mesh, and 120 mesh sieves and a pan. The stack was placed in a Ro-Tap Testing Sieve Shaker for 10 minutes. Each size fraction was rinsed with acetone under a fume hood and placed into a brownie pan to dry. The dried sample was then placed into a labeled Ziploc freezer bag.

Samples DPL30 and DPUA22 were vein samples that contained a variety of minerals. Calcite was separated from the rest of the minerals in these samples using the following method. The <60 >80 mesh size fraction was poured into a burette filled with sodium polytungstate. Several ounces of distilled water were added to the burette, and the sodium polytungstate, sample, and water were mixed to create a density gradient. Sample DPL30 separated into 5 layers, with layer 3 grading into layer 4. Sample DPUA22 separated into 5 distinct layers. Each layer was drained into a funnel lined with labeled filter paper, washed with distilled water, then set under a fume hood to dry. The dried layers were placed into labeled glass vials. Inspection under the binocular microscope showed layer 4 from sample DPL30 and layer 3 from sample DPUA22 contained a majority of calcite crystals but were not pure calcite. Individual calcite grains were hand-picked under the binocular microscope using a moistened artist's paintbrush with most of the bristles removed. At least 50 milligrams of calcite were collected from each sample and placed in a labeled glass vial for transport to the New Mexico Institute of Mining and Technology.

The remaining samples contained almost pure calcite. The <60 >80 mesh size fractions from these samples were placed under a binocular microscope, and any impurities were removed by hand as described above. At least 50 milligrams of each

sample were placed in a labeled glass vial for transport to the New Mexico Institute of Mining and Technology.

Whole-Rock X-Ray Fluorescence Analysis

X-ray fluorescence analysis was used to monitor variations in Mg concentration with increasing alteration. All of the wall rock samples that were sent for stable isotope analysis (except for sample DPL30a) were also sent to Chemex Labs in Sparks, Nevada for whole-rock, major element XRF analysis. (The size fraction >30 mesh that was prepared for stable isotope analysis as described above was used.) The samples included five unaltered limestones, two partly altered limestones, and three highly altered limestones. The detection limit and precision for each element is 0.01% and 5%, respectively.

X-Ray Diffraction Analysis

Nineteen vein samples and two unaltered limestone samples were analyzed by X-ray diffractometry to identify the minerals present. Ten samples were analyzed at the University of Windsor, Ontario, Canada, and the other eleven were analyzed at the University of Nevada, Las Vegas. The detection limits at the University of Windsor, Ontario and the University of Nevada, Las Vegas are 1% and 10%, respectively.

Sample Preparation and Analysis at UNLV

In the lab, samples were broken by hand into chips ≤ 0.5 cm (using a rock hammer when necessary), then ground into a powder the consistency of flour in a diamonite mortar and pestle. The powder was placed into labeled glass vials.

Approximately 0.5 gram of the powder was placed into a plastic and aluminum sample holder and analyzed in a Philips-Norelco X-ray diffractometer with a Dapple-modified goniometer that is controlled by Dapple XRD software running on an Apple IIGS computer. Peaks were located and marked manually using the mouse and the strip chart image that appears on the computer monitor after each run. The minerals were identified manually using the Fink and Hanawalt methods with the JCPDS search manual (JCPDS, 1980a) and the JCPDS mineral file (JCPDS, 1980b).

X-Ray Diffraction at the University of Windsor

At least 5 grams of each sample were prepared and placed into glass vials as described above, then sent to Dr. William H. Blackburn at the University of Windsor, Ontario, for analysis in a Philips 1550 X-ray diffractometer controlled by Sietronics 122 automation hardware and software. Minerals were identified using the μ PDSM search/match identification program (Fein-Morquart and Associates) and the JCPDS mineral file (JCPDS, 1980b).

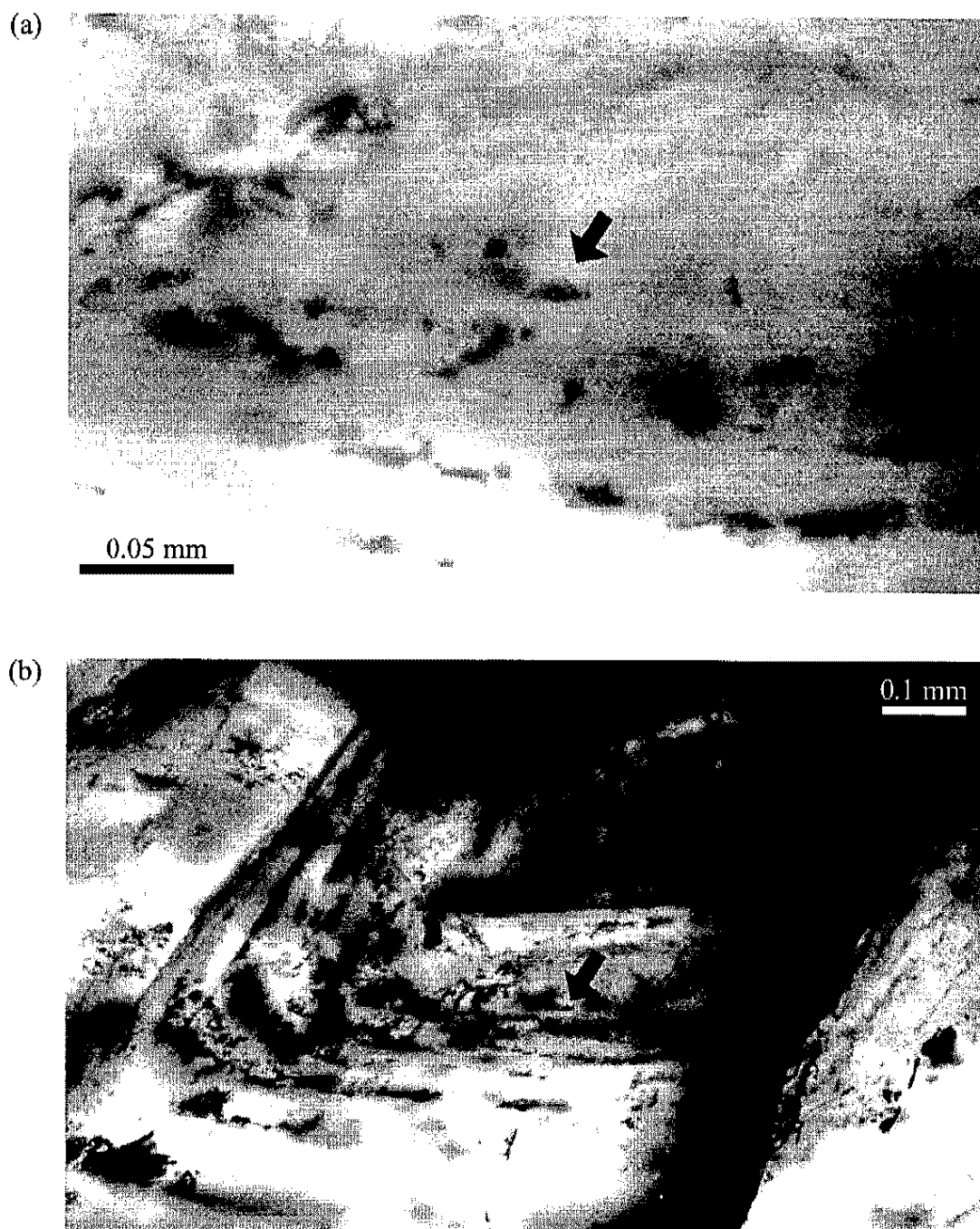


Figure 2-1. (a) Typical fluid inclusion in sample DPL26, and (b) the growth-zoned calcite crystal that contains it. (Plane polarized light).

CHAPTER 3

GEOLOGY OF THE DEVIL PEAK AREA

Regional Geology

Lithology

The southern Spring Mountains consist mainly of Paleozoic carbonate rocks and sparse Tertiary volcanic and intrusive rocks. The Paleozoic carbonate rocks include, from oldest to youngest, the Middle Cambrian to Devonian(?) Goodsprings Dolomite, the Devonian Sultan Limestone, the Mississippian Monte Cristo Limestone, and the Pennsylvanian to Permian Bird Spring Formation (Longwell et al., 1965; Walker et al., 1980; Carr and Pinkston, 1987). The Goodsprings Dolomite has been subdivided into four units, with unit 1, the oldest, at the base. Units 1 and 2 correspond to the Bonanza King Formation of Hazzard and Mason (1936)(Carr and Pinkston, 1987). The Cambrian parts of units 3 and 4 correspond to the Nopah Formation of Hazzard (1937), and the Ordovician part of unit 4 corresponds to the Mountain Springs Formation of Gans (1974)(Carr and Pinkston, 1987).

In addition to Devil Peak, Tertiary volcanic and intrusive rocks crop out in two other areas in the Spring Mountains (Figure 1-1). Table Mountain, located 8 km north of Devil Peak, consists of Tertiary tuffs and coalescing dacite domes (Longwell et al., 1965; pers. comm., E. I. Smith, 1995). A sequence of Tertiary latite flows, tuffs, and breccias

lies approximately 5 km northwest of Devil Peak (Longwell et al., 1965; pers. comm., E. I. Smith, 1995).

Structure

Major Mesozoic deformational structures within the southern Spring Mountains include the two easternmost faults of the Sevier overthrust belt, the Keystone thrust and the Sultan thrust. The Keystone thrust trends northeast through the Spring Mountains, placing Cambrian strata over Devonian to Jurassic strata (Burchfiel et al., 1974). Near Devil Peak, the Keystone thrust lies on the east side of the Spring Mountains and places the Cambrian Bonanza King Formation over the Permian Bird Spring Formation (Longwell et al., 1965). The Sultan thrust is structurally higher than the Keystone thrust and places the Mississippian Monte Cristo Limestone over the Permian Bird Spring Formation near Devil Peak (Longwell et al., 1965; Walker et al., 1980). The Sultan thrust generally trends northwest and crops out to the northwest of Devil Peak (Figure 1-2).

Previous Work

Previous work in the Devil Peak area includes reconnaissance studies by Hewett (1931, 1956) and Armstrong (1970), and a mapping project by Walker et al. (1980). In 1931 and 1956, Hewett described the general geology of the area while mapping the Ivanpah Quadrangle (1° x 1°) and the Goodsprings Quadrangle (40' x 11'). Hewett (1956) first recognized and described contact metamorphic aureoles to the southeast of Devil Peak. Armstrong (1970) published a whole-rock K-Ar date of 12.6 ± 0.3 Ma for the Devil Peak rhyolite as part of a regional geochronologic study of Tertiary igneous rocks in the eastern Basin and Range. Walker et al. (1980) mapped the Devil Peak area at a scale

of 1:10,500 and interpreted structures resulting from the intrusion of the Devil Peak plug as part of a Senior Thesis at the Massachusetts Institute of Technology.

Major Findings by Walker et al. (1980)

Structures mapped by Walker et al. (1980) include Mesozoic imbricate thrust faults with associated tear faults and folds as well as high-angle boundary faults related to the intrusion of the Devil Peak plug. Walker et al. (1980) suggest that imbricate thrust faults and associated east-vergent folds to the north and east of Devil Peak are related to the Mesozoic Sultan thrust (Figure 3-1). These workers also identified two high-angle boundary faults, one northwest and one southwest of Devil Peak, that separate rocks tilted during emplacement of the rhyolite plug from Paleozoic country rock that was relatively undisturbed by the intrusion (Figure 3-1). Walker et al. (1980) conclude that initial displacement on the southwestern boundary fault was north side up, but later displacement on the fault was north side down.

Walker et al. (1980) also identified and described a variety of volcanic and volcanoclastic units associated with the Devil Peak intrusion. The unit designations of Walker et al. (1980) were retained for this study, and the following units were added: altered Mississippian Monte Cristo Limestone (Mma), partly altered Mississippian Monte Cristo Limestone (Mmp), undivided Tertiary rhyolite (Tr), Quaternary talus (Qt), and man-made disturbance (Qm) (Plate 1).

Geology of the Field Area

Southeast of Devil Peak, near-horizontal beds of unaltered and altered Monte Cristo Limestone form a northeast-trending ridge. Devil Peak is separated from this ridge

by a large, northeast-trending wash. The mapped area covers a 1.5 km stretch of the large wash, and extends 260 m southeast into the Monte Cristo Limestone and 200 m northwest onto the Devil Peak plug (Figure 1-2, Plate 1).

Lithology

Rocks cropping out in the southeast Devil Peak area consist mainly of a stack of Paleozoic carbonate rocks intruded by the Devil Peak rhyolite plug and an associated rhyolitic dike (Plate 1). The carbonate rocks are mantled by volcanic and volcanoclastic rocks associated with the emplacement of the plug. In the vicinity of the contact with the igneous rocks, the carbonate rocks are bleached to varying degrees and locally crosscut by veins.

In the mapped area (Plate 1), the Mississippian Monte Cristo Limestone (Mm) is a dark blue-black, cliff-forming, thick-bedded carbonate mudstone that locally contains abundant crinoid fossils. Bed thicknesses range from 0.3 m to mostly 3 m or greater. Near the contact with the igneous rocks, the Monte Cristo Limestone is altered to a chalky, dolomitized marble that is bleached beige to white and commonly crosscut by numerous veins containing calcite and Mg-bearing minerals (Mma). In some areas near the igneous contact, the Monte Cristo Limestone is only slightly bleached to a mottled gray or light blue color, is recrystallized in some places, and contains only a few narrow (< 1 cm) calcite veins (Mmp). Three adits have been driven into the altered limestone. The eastern adit is located in the large area of altered limestone in the northeast, and the two western adits are located next to each other in the large area of altered limestone in the southwest.

A string of six outcrops of gray, aphanitic rhyolite (Tvg) trends northeast through the field area (Plate 1). The outcrops that are not predominantly obscured by Quaternary cover are elongated to the northeast. The outcrops are intrusive, as indicated by small brecciated dikes and pods of the gray rhyolite ranging from 6 cm to 0.5 m in width that intruded the limestones near the eastern adit (Figure 3-2). Some of these dikes and pods are hydrothermally altered. The rhyolite outcrops appear discontinuous because they are separated by Quaternary cover, but the enveloping surface defined by the string of outcrops suggests they comprise a single large dike that is at least 900 m long and 60 m wide. At the western end of the dike, the rhyolite contains bands of tiny, elongated, subparallel lithophysal cavities, approximately 1 mm x 2 mm.

Tertiary debris flows and flow breccias (Tvb) are ubiquitous in the map area (Plate 1). They are generally clast-supported, and contain varying amounts of pumice (from < 1% to \pm 40%). Clasts range in size from approximately 1 mm to 2 m, and are dominantly angular to subangular fragments of gray rhyolite (Tvg), with sparse fragments of red or brown rhyolite.

Seven small, isolated outcrops of undivided rhyolite occur in the map area (Plate 1). These rhyolites were not mapped by Walker et al. (1980) and are labeled Tr.

Cropping out in the southwest corner of the map area is a complex unit (Tru) consisting of basal rhyolite and rhyolite breccia that grades upward into brown rhyolite (Plate 1). The base of the unit is comprised of about 0.5 m of red flow-banded rhyolite that shows shearing adjacent to the contact with the underlying gray rhyolite (Tvg). Overlying the basal rhyolite is a 0.7 m section of red flow-banded rhyolite that contains a maximum of 40% angular gray rhyolite clasts up to 0.3 m in size. The clasts are generally

oriented parallel to flow banding. The flow-banded red rhyolite grades upward into a vesicular breccia containing angular clasts of red rhyolite and gray rhyolite in a yellowish-white matrix of devitrified, clay-altered rhyolite. The angular rhyolite clasts range in size from about 2 mm to 2 cm. This breccia layer varies in thickness, with a maximum thickness of about 1.3 m. The uppermost layer of this unit is brown flow-banded rhyolite that is locally brecciated and contains sparse small (≤ 2 cm) fragments of gray rhyolite. The layered nature of this unit, combined with the shearing along the basal contact, the incorporation of fragments of the underlying gray rhyolite, the brecciated and vesicular nature of the uppermost layer, and sub-horizontal flow banding in the uppermost layer indicate that it is composed of one or more flows.

Near the adits, waste rock has been assembled into huge piles. These piles and other areas with bulldozed waste rock are designated as man-made disturbance (Qm) (Plate 1). Quaternary alluvium is labeled Qa, and Quaternary talus is labeled Qt.

Structure

The most prominent structural feature in the mapped area is a large fault that strikes northeast through the center of the mapped area, separating the gray intrusive rhyolite from the Monte Cristo Limestone (Plate 1; Figure 3-3). The fault dips 48° to 66° northwest. Steps in slickenlines in the footwall of the fault at the entrance to the westernmost adit indicate the most recent movement was hanging wall down. The northeast end of the fault is covered by alluvium about 150 m southwest of the eastern adit and is not visible farther north. The southwest end of the fault disappears into the

covered area west of the western adits and is not visible farther south. The fault trace or surface is visible along approximately 70% of its mapped length.

A north-south oriented fault may project through a large wash near the center of the mapped area. Evidence for the existence of this fault includes the apparent offset of the normal fault 25 m to the north on the west side of this wash, and the slight steepening in the dip of the prominent fault to the west of this wash.

A small fault separates altered Monte Cristo Limestone from unaltered Monte Cristo Limestone in the east central map area. The fault, which coincides with a minor wash, trends N25°W, and is indicated by a zone of tectonically brecciated limestone that is 1 - 3 cm thick.

Alteration

The Monte Cristo Limestone is altered in two major areas (Plate 1). The easternmost area is approximately 0.015 km² and generally follows bedding. The westernmost area is approximately 0.044 km² and is more irregular in shape. In each altered area, the most intensely altered limestone is bleached white, intensely fractured, and crosscut by numerous veins. The fracture and vein densities decrease with increasing distance from the highly altered zones. In the highly altered zones, the fracture and vein density reaches a maximum of 15 fractures and veins per square meter. Within several tens of meters away from the highly altered zones, the fractures and veins essentially disappear, although the intense bleaching continues throughout the areas mapped as altered Monte Cristo Limestone (Mma). The limestone in the most intensely bleached, fractured, and veined areas has been dolomitized. The three adits described previously are

located in the highly altered, dolomitized limestone. The western adits have been driven into an intensely faulted and sheared zone, approximately 15 m wide, that parallels the normal fault at the gray rhyolite-altered Monte Cristo Limestone contact. Most of the walls in the western adits are fault surfaces. No comparable well-defined structural zone is visible in the altered limestones near the eastern adit, although in this area the gray rhyolite-altered Monte Cristo Limestone contact lies within the large wash. Similar sheared and faulted rock is likely present here also but is either at depth or is covered by alluvium and mine dumps.

A 10 m-wide zone of dynamically recrystallized partly altered limestone (Mmp) that is slightly bleached to a light blue color parallels the normal fault in the center of the mapped area. This limestone does not contain any veins. Several large areas of recrystallized limestone that is slightly bleached to a mottled gray color and contains few or no veins (Mmp) lie within and around the western zone of altered limestone (Mma).

Description of the Veins

Veins occur exclusively in altered and partly altered Monte Cristo Limestone (Mma and Mmp). X-ray diffraction analysis of vein samples shows the veins contain various combinations of calcite, brucite, quartz (chalcedony), hydromagnesite, and serpentine, with minor dolomite and clinochlore (Table 3-1). A hydrothermally altered rhyolite breccia (probably an explosion breccia) is also present in some of the veins. The most common vein assemblages include calcite, brucite, and hydromagnesite. Serpentine occurs most commonly with the rhyolite breccia.

The rhyolite breccia contains angular rhyolite fragments and rounded limestone fragments, ≤ 1 cm in size, in a green or red, fine-grained silica matrix. The breccia is found only in the easternmost adit and usually occurs in composite rhyolite breccia-mineral veins. In these composite veins, the breccia occupies the center of the vein while any minerals present mantle the vein margins.

Veins containing rhyolite breccia tend to be wider (2 - 10 cm wide) than those lacking it (1 - 7 cm wide). Some veins lacking rhyolite breccia contain vugs, and some contain layers of minerals that give the veins a banded appearance. Vugs can be up to 4 cm in diameter and commonly contain some combination of brucite plates, spheres of radiating hydromagnesite crystals, and botryoidal calcite.

All veins containing rhyolite breccia strike N 20-55° E and dip 55-77° NW, roughly parallel to the large fault. These breccia veins both crosscut and are crosscut by veins striking N 34-71° W and dipping 83-88° SW or 73-85° NE, and by veins striking N 20-75° E and dipping 64-77° SE.

In vein hand samples, brucite forms translucent clear-white, inelastic, mica-like plates with a pearly luster. Hydromagnesite forms spheres, ≤ 3 mm in diameter, composed of clear-white, radiating, needle-like crystals. The serpentine polymorphs are massive and translucent-light-green to pistachio green. Chalcedony is translucent to white and banded or botryoidal. Calcite is white or clear, banded or botryoidal when mantling vein walls, and forms crystals up to 1 cm long in the center of veins and in vugs.

Origin of the Veins

Field evidence indicates that the veins in the Monte Cristo Limestone were formed by a hydrothermal system related to the Devil Peak rhyolite and/or the associated gray rhyolite dike. Bleached limestone, hydrothermally altered rhyolite, and the deposition of minerals in veins in the bleached Monte Cristo Limestone all denote that hydrothermal activity occurred in the area. Several lines of evidence indicate that the hydrothermal activity is associated with the Devil Peak rhyolite and/or the gray rhyolite dike. The only hydrothermally altered rocks in the area occur within 600 m or less of the Devil Peak rhyolite and the gray rhyolite dike, and the altered rocks are commonly in contact with the gray rhyolite dike. Also, the general trend of the altered areas parallels the southeast margin of the Devil Peak plug and the strike of the gray rhyolite dike. Furthermore, as mentioned previously, the rhyolite dike intruded the altered limestones near the eastern adit, and the rhyolite itself is hydrothermally altered in some places where it intruded the altered limestones. Finally, no other intrusive rocks are present in the map area.

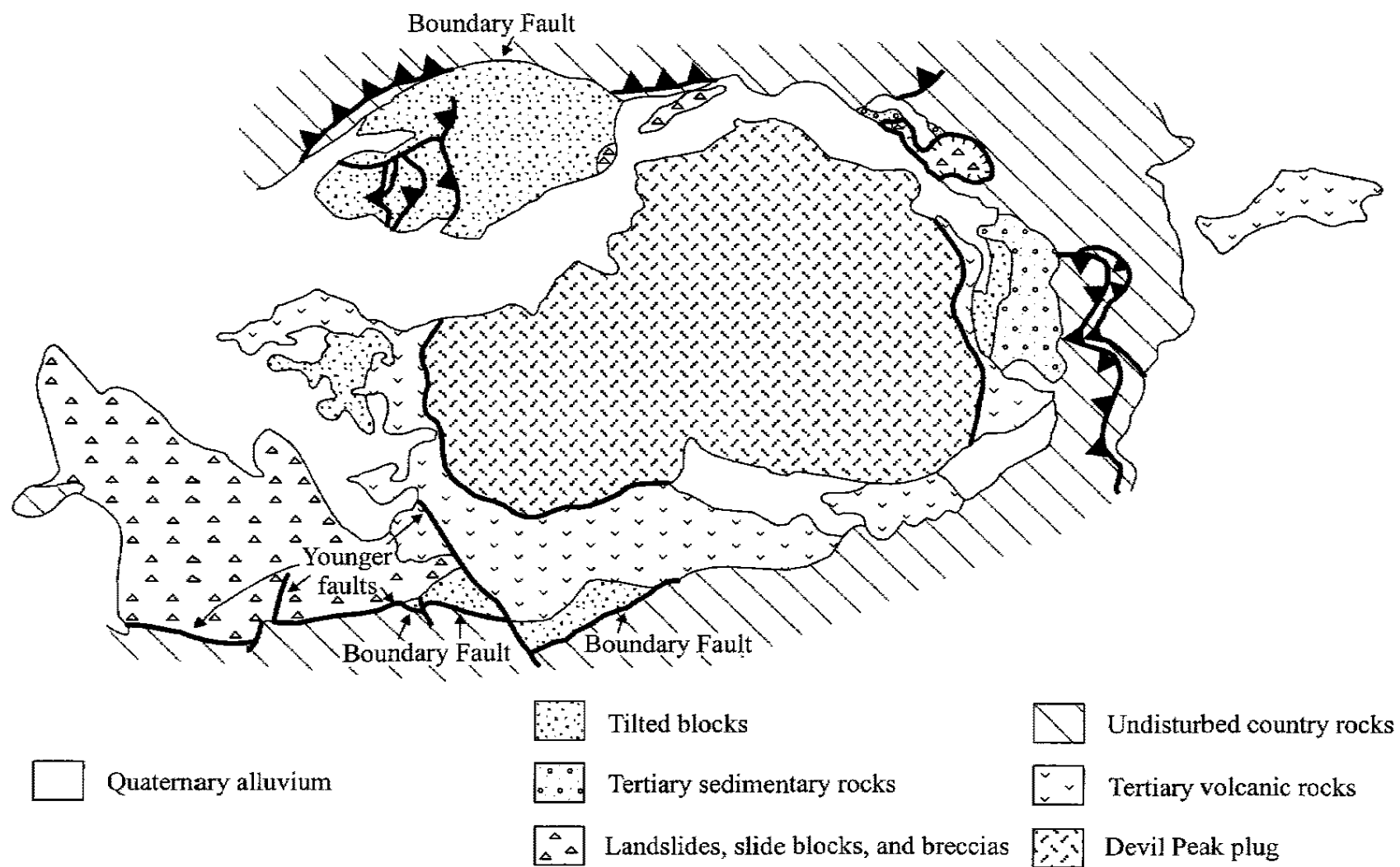


Figure 3-1. Boundary faults related to the intrusion of the Devil Peak plug. Modified from Walker et al. (1980).



Figure 3-2. Thin dikes of gray rhyolite (Tvg) that intruded dolomitized limestone near the eastern adit. Pocket knife in center of picture for scale.



Figure 3-3. Large fault separates the gray rhyolite dike (Tvg) from the altered Monte Cristo Limestone (Mma). Mmp = partly altered Monte Cristo Limestone. Adit opening is approximately 5 m high. Fault surface is visible to the left of adit opening.

Table 3-1. Results of X-ray diffraction analysis of Devil Peak samples. Abbreviations: ant = antigorite, bru = brucite, cal = calcite, chrys = chrysotile, clinochrys = clinochrysotile, dol = dolomite, bx = rhyolite breccia, hmag = hydromagnesite, liz = lizardite. The detection limit is 1% at the University of Windsor and 10% at UNLV.

Sample	Type	Minerals Present	Analyzed at
DPL1	vein	cal, dol, hmag, bru	U. of Windsor
DPL4	vein (w/bx)	clinochrys, ant, clinochlor, rectorite, cal	U. of Windsor
DPL9	vein	clinochrys, cal, liz	U. of Windsor
DPL14	vein	bru, cal, hmag	U. of Windsor
DPL21	vein	cal, bru	U. of Windsor
DPUA9	vein	cal, clinochrys, ant	U. of Windsor
DPUA20	vein	cal	U. of Windsor
DPUB15	vein	cal	U. of Windsor
DPUB22	vein	cal, ant	U. of Windsor
DPL14	vein	bru	UNLV
DPL14-fib	vein	hmag, quartz	UNLV
DPL14-gr	vein	ant, cal	UNLV
DPL14-wh	vein	bru, cal	UNLV
DPL25	vein	cal	UNLV
DPL30	vein	cal, quartz, dol?, liz?, bru?, hmag?	UNLV
DPUA22	vein	cal, liz, quartz, ant?, hmag?	UNLV
DPUA23a	vein	liz, cal	UNLV
DPV1	vein	liz, chrys	UNLV
DPV2	vein	cal, ant	UNLV
DPL34	unaltered ls	cal	UNLV
DPU2	unaltered ls	cal	UNLV

CHAPTER 4

PETROGRAPHY AND PARAGENESIS

Vein minerals identified in thin sections of highly altered veined limestone include calcite, serpentine polymorphs, chalcedony, brucite, hydromagnesite, dolomite, and clinochlore. Crinoid fossils and carbonate pellets were found in thin sections of the unaltered limestone. The thin sections of rhyolite, partly altered limestone, and highly altered limestone were too fine-grained to positively identify any minerals.

Description of Vein Minerals

At Devil Peak, brucite occurs in mica-like laths (Figure 4-1). The laths are length fast, produce uniaxial positive interference figures, and show parallel, mottled extinction. Chalcedony forms bands of low-birefringence, microcrystalline quartz that mantle the vein walls. The bands consist of parallel fibers that are oriented perpendicular to the vein wall (Figure 4-2). The serpentine polymorphs are so similar that electron microscopy is required to unequivocally distinguish among them, hence no attempt is made in this study to do so. The serpentine minerals occur as nets or webs composed of white, needle-like crystals (Figure 4-3). Hydromagnesite forms radiating, needle-like crystals of high birefringence (Figure 4-4). Vein calcite is banded or forms mostly euhedral and some anhedral crystals. Dolomite is rare in veins. Where present, dolomite forms euhedral crystals that contain cores of calcite. Clinochlore is also rare (it occurs in only a few

microveins) and forms small, mica-like laths that can be distinguished from brucite by their optic sign, which is biaxial positive.

Relative Abundances of Minerals

Calcite is the most abundant vein mineral at Devil Peak, occupying every vein examined in thin section and in hand sample. The next most abundant vein mineral is serpentine, followed by chalcedony, brucite, hydromagnesite, dolomite, and clinochlore (Table 4-1).

Conspicuously absent from the vein thin sections is periclase, which commonly occurs in association with brucite in hydrothermal systems (e.g., Crestmore, California (Brown et al., 1985) and Stephen Cross Quarry, Quebec, Canada (Cartwright and Weaver, 1993)). Periclase was neither detected by X-ray diffraction nor observed in thin section. Furthermore, when periclase is present it usually alters to brucite as the system cools, forming a diagnostic onion-skin texture. This texture, discussed in more detail later in this chapter, has not been found in thin section.

Also notable is the scarcity of open-space dolomite in the veins; more dolomite might be expected considering that the host rocks are carbonates and that most of the vein minerals contain Mg. Vein dolomite was found in only one thin section, and detected in only one of the samples analyzed by X-ray diffraction.

Open-Space and Replacement

Minerals at Devil Peak

Petrographic evidence indicates that chalcedony and most of the calcite were precipitated in open space. Chalcedony occurs in symmetrical, concentric bands that

mantle the vein walls; a classic open space-filling texture. Three other diagnostic open space-filling textures indicate that most of the calcite was deposited in open space. Many euhedral calcite crystals exhibit growth zoning, which is delineated by impurities that collected on the surface of the crystal as it grew in open space. Many calcite-bearing veins contain small, euhedral calcite crystals along the vein margins and coarser, euhedral crystals toward the center of the vein. Many veins also have vuggy centers rimmed by euhedral calcite crystals.

Published information on brucite formation is sparse, vague, and often contradictory. Some optical mineralogy textbooks state that brucite is always a replacement mineral (e.g., Phillips and Griffen, 1981, p. 41; Gribble and Hall, 1985, p. 169), but the majority of mineralogy and optical mineralogy textbooks do not address the subject in their descriptions of brucite (e.g., Klein and Hurlbut, 1985, p. 315; Nesse, 1991, p. 134). Most references state that when brucite exhibits a whorly, fibrous habit it has replaced another mineral (e.g., Carpenter, 1967), and that whorly brucite with an onion-skin texture has replaced periclase (Turner and Weiss, 1965; Carpenter, 1967). Carpenter (1967) distinguishes onion-skin brucite from brucite that forms by in-situ replacement of dolomite (Figure 4-5). Brown et al. (1985) found “primary laths” of open-space brucite, which they distinguished from replacement brucite with onion-skin texture, in a calc-silicate scarn at the Pine Creek mine, California.

Euhedral, mica-like laths of brucite at Devil Peak (Figure 4-1) suggest open-space growth. This is supported by textural evidence in sample DPUA12 (Figure 4-6), which shows brucite laths that grew into open space in a vug. The lack of replacement brucite textures, such as whorly or onion-skin brucite, is further evidence for open-space brucite.

Serpentine could have replaced another mineral or precipitated in open space.

When present in hydrothermally altered carbonate rocks, serpentine commonly replaces forsterite (e.g. Cartwright and Weaver, 1993). This may not be the case at Devil Peak, because no remnant forsterite was detected in thin section or by X-ray diffraction, and because evidence presented in the next chapter indicates that it is unlikely that forsterite could have formed under the conditions of alteration at Devil Peak. Evidence presented in the next chapter also indicates that the serpentine could have precipitated directly from solution.

Paragenetic Sequence

Textural evidence indicates that chalcedony was the earliest (non-carbonate) mineral to form. The precipitation of chalcedony in open space was followed by the formation of the serpentine polymorphs, and then by the precipitation of brucite in open space. Hydromagnesite formed last, possibly replacing brucite. Calcite precipitated throughout the entire sequence. Most of this sequence can be seen in slide DPUA12, which shows a single vein that contains alternating bands of chalcedony and calcite mantling the walls of a vug, with brucite and hydromagnesite filling in the center (Figure 4-7).



Figure 4-1. Brucite laths. (Slide DPL14-M2, crossed nicols).

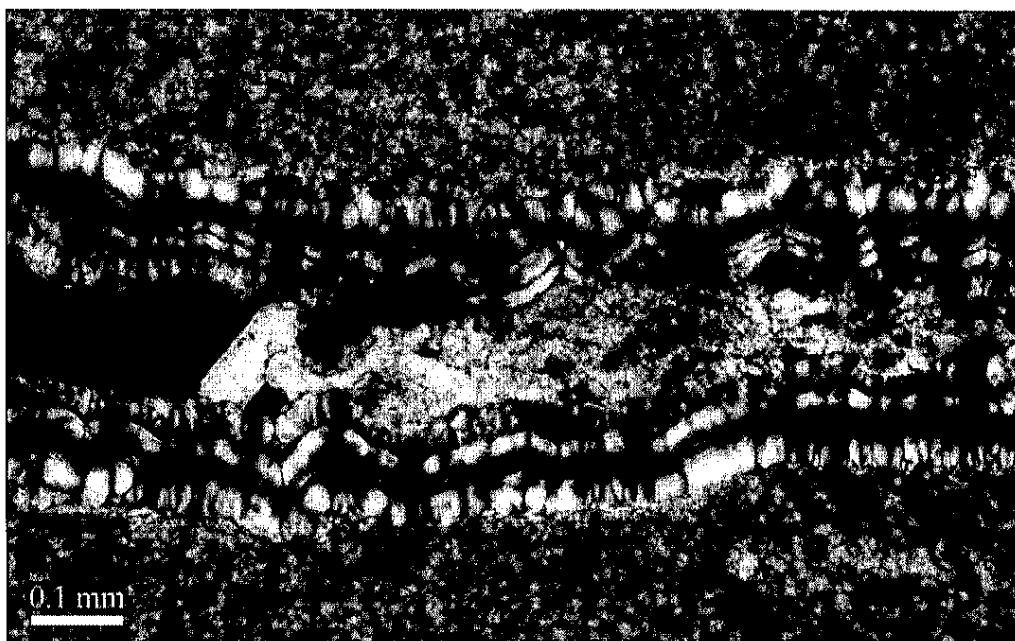


Figure 4-2. Vein containing banded chalcedony. Calcite fills the center of the vein. (Slide RK-4, crossed nicols).

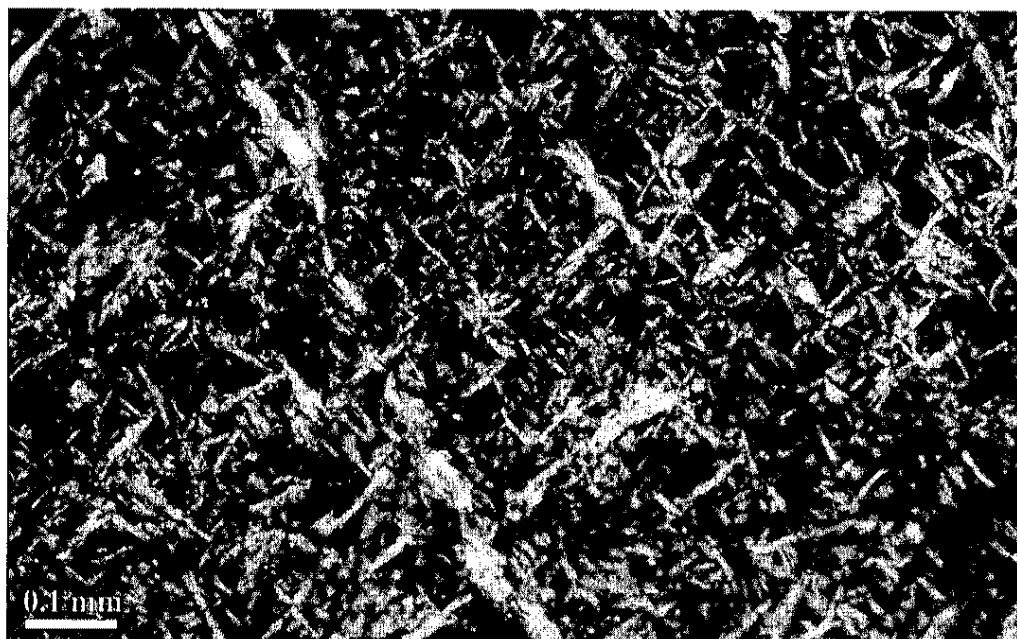


Figure 4-3. Netlike texture in serpentine. (Slide DPL13, crossed nicols).

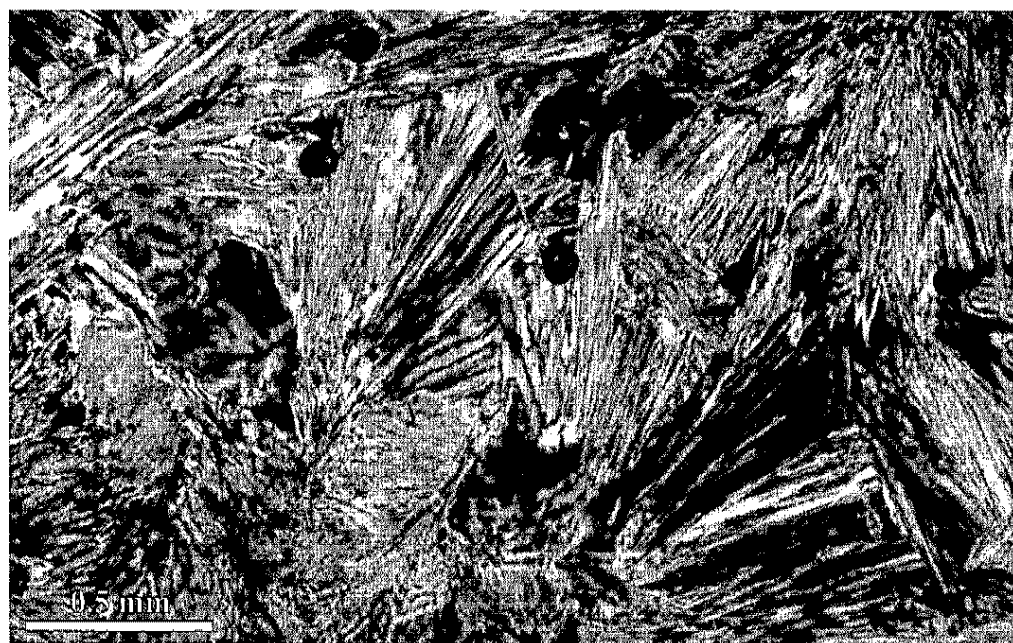


Figure 4-4. Hydromagnesite needles. (Slide DPL14-1, crossed nicols).

Table 4-1. Mineral assemblages in vein thin sections that contain other minerals in addition to calcite. % of Vein = the visually estimated percent of the vein each mineral comprises. Abbreviations: bru = brucite, cal = calcite, chal = chalcedony, dol = dolomite, hmag = hydromagnesite, serp = serpentine.

Thin Section	Vein Minerals (% of Vein)
DPL14-1	serp (40%) + cal (30%) + hmag (15%) + chal (12%) + bru (3%)
DPL14-2	cal (50%) + serp (30%) + chal (10%) + hmag (9%) + bru (1%)
DPUA12	cal (78%) + chal (15%) + bru (5%) + hmag (2%)
DPL14-M1	serp (63%) + chal (25%) + dol (8%)
DPL14-M2	bru (60%) + hmag (35%) + cal (5%)
DPL26	serp (90%) + cal (7%) + chal (3%)
DPUA2	cal (83%) + serp (15%) + chal (2%)
RK-3	cal (62%) + serp (35%) + chal (3%)
RK-4	cal (80%) + serp (15%) + chal (5%)
DPL13	cal (90%) + serp (10%)
DPUA17	serp (90%) + cal (10%)
RK12	cal (60%) + serp (40%)

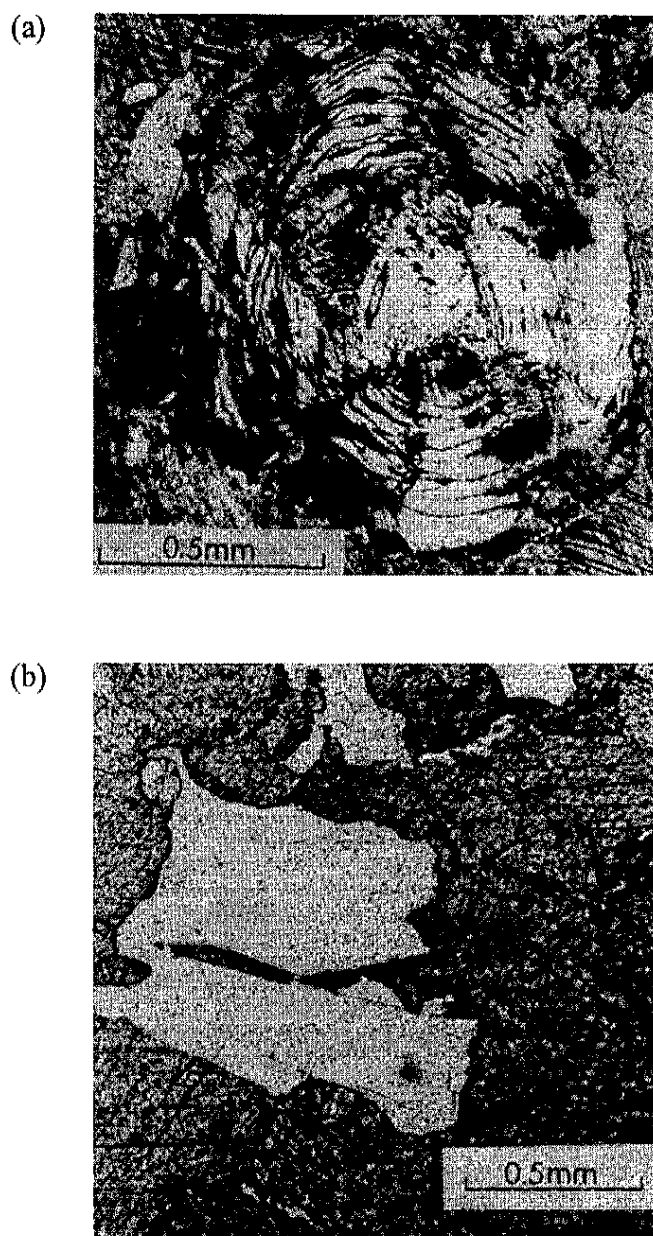


Figure 4-5. Photomicrographs of brucite replacement textures from Carpenter (1967).
(a) Pseudomorph of "onion-skin" brucite after periclase (crossed nicols).
(b) Pseudomorph of platy brucite after dolomite (plane polarized light).

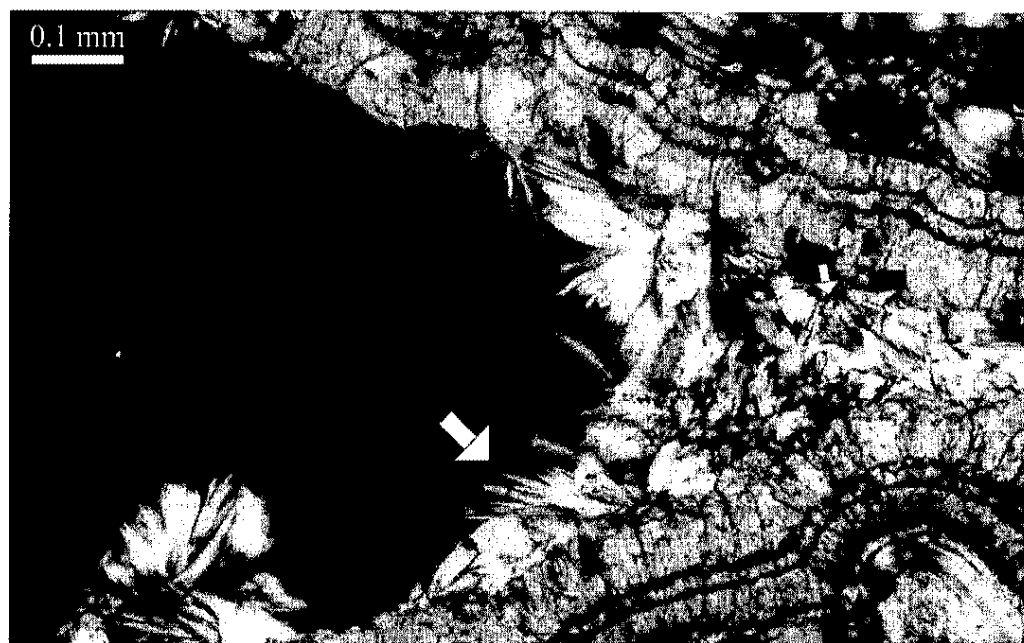


Figure 4-6. Brucite laths (small white arrow) and hydromagnesite needles (large white arrow) that grew in open space in a vug. (Slide DPUA12, crossed nicols).

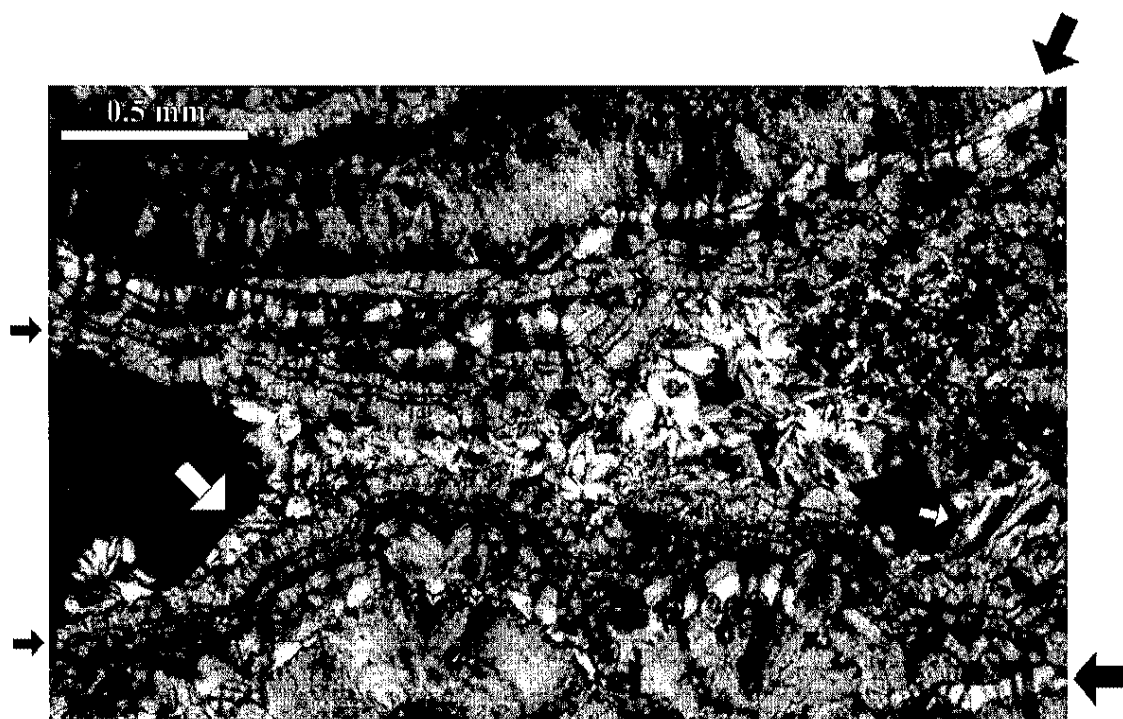


Figure 4-7. Vug containing symmetrical bands of calcite (small black arrows) and chalcedony (large black arrows), with brucite (small white arrow) and hydromagnesite (large white arrow) filling in the center. (Slide DPUA12, crossed nicols).

CHAPTER 5

FLUID INCLUSION ANALYSIS

An exploratory fluid inclusion study was done to gather ice melting temperatures and homogenization temperatures that may help restrict the composition and temperature of the hydrothermal fluid that deposited the minerals in the veins at Devil Peak. The fluid inclusions are from sample DPL26, a portion of a 7-cm thick calcite vein from the eastern adit. Data were collected on 47 fluid inclusions from 5 growth-zoned calcite crystals. Although the fluid inclusion temperatures were collected from a single sample and hence describe only one area of the system, the data do provide constraints on the temperature and composition of the hydrothermal fluid.

CO₂ and Salt Content of the Fluid

Visual inspection of the fluid inclusions during freezing studies did not indicate the presence of CO₂. No phase changes that denote the presence of CO₂, such as the formation of clathrate or the melting of CO₂ ice, were observed. Also, liquid CO₂ should be visible at 10°C if $X_{\text{CO}_2} > 0.04$ (Hedenquist and Henley, 1985). No liquid CO₂ was observed in any of the inclusions; thus $X_{\text{CO}_2} < 0.04$ for the fluid that deposited the calcite crystals.

Final ice melting temperatures, measured from 31 fluid inclusions, range from -0.6°C to 0.0°C (Table 5-1), with a mean of -0.3°C , a mode of -0.3°C (Figure 5-1), and a standard deviation of 0.2°C . The majority of final ice melting temperatures measured were below that of pure ice. The depressions in the final ice melting temperatures could be caused by the presence of NaCl and/or CO_2 . The concentrations of NaCl and CO_2 and depression of the final ice melting temperature are related by the following equation (Hedenquist and Henley, 1985):

$$T_m = - \sum K_i m_i$$

where T_m = the final ice melting temperature, K_i = the molal freezing point depression constant for species i , and m_i = the molality of species i . For Na^+ and Cl^- , $K = 1.72$, and for CO_2 , $K = 1.86$ (Hedenquist and Henley, 1985). To calculate the precise concentration of one of the species from the measured final ice melting temperature, the concentration of the other must be known, but the maximum possible concentration for each species can be calculated by assuming that the concentration of the other species equals zero. Assuming no NaCl is present in the fluid inclusions yields a maximum possible $X_{\text{CO}_2} = 0.0058$, and assuming no CO_2 is present gives a maximum $X_{\text{NaCl}} = 0.0031$, or 0.99 wt. % NaCl (Table 5-1).

Homogenization Temperatures and P-T

Behavior of the Hydrothermal Fluid

The temperature at which fluid inclusions homogenize is the minimum temperature at which the inclusions could have formed. Homogenization temperatures measured from 29 fluid inclusions range from 119°C to 188°C , with a mean of 151°C , a mode of 154°C ,

and a standard deviation of 17°C. The largest number of measurements fall within the range of 150-160°C (Figure 5-2). The large range in homogenization temperatures suggests that some of the inclusions may be stretched or necked down, which is common in low temperature systems.

Inclusions in two of the calcite crystals provide additional insight into the temperature behavior of the hydrothermal fluid. A crystal in chip A3 contains three fluid inclusions that reside in three adjacent growth zones (Figure 5-3). The fluid inclusions have homogenization temperatures ranging from 154 - 165°C. These homogenization temperatures are considered consistent because they are all within about 10°C (De Vivo and Frezzotti, 1994); such consistency in homogenization temperatures indicates that the temperature of the hydrothermal fluid remained fairly constant throughout the growth of these zones.

In a crystal in chip B4, data were measured from fluid inclusions in growth zones at increasing distances from the core of the crystal (Figure 5-4). The inclusions closer to the core (group A) have homogenization temperatures of approximately 155 - 170°C. A little farther from the core, the fluid inclusions in group C have homogenization temperatures of around 120 - 135°C. Still farther from the core, group D homogenization temperatures range from around 140 - 155°C. The homogenization temperatures in group B are highly variable and may be necked down or stretched. While the homogenization temperatures in B4 are fairly consistent within the groups of fluid inclusions, they vary across the growth zones. This variation in homogenization temperatures across the growth zones indicates that the temperature of the hydrothermal fluid was high when the crystal began to form, but decreased as the center portion of the

crystal precipitated, and then increased during precipitation of the outer portion of the crystal.

Summary and Conclusions

A total of 31 final ice melting temperatures and 29 homogenization temperatures were measured from 47 primary fluid inclusions in 5 growth-zoned calcite crystals from a vein. Final ice melting temperatures range from 0.0°C to -0.6°C . The presence of CO_2 or salt in the fluid inclusions could have caused the depression of the ice melting temperatures. The maximum possible concentration of CO_2 in the fluid was calculated to be $X_{\text{CO}_2} = 0.0058$, and the maximum possible concentration of salt in the fluid was calculated to be 0.99 wt. % NaCl. Homogenization temperatures, which represent the minimum temperature of the hydrothermal fluid at the time the fluid inclusions were trapped, range from 119°C to 188°C , with a mode of 154°C . Two calcite crystals give additional insight into the temperature of the hydrothermal fluid. Consistent homogenization temperatures of around $155 - 165^{\circ}\text{C}$ across three growth zones in one of the crystals show that the temperature of the hydrothermal fluid remained relatively constant during formation of those growth zones. The other crystal contains groups of fluid inclusions with homogenization temperatures that vary across growth zones, indicating that the temperature of the hydrothermal fluid fluctuated as the crystal grew.

Table 5-1. Results of fluid inclusion analysis of sample DPL26. Tm = final ice melting temperature, Th = homogenization temperature.

Chip #	Fluid Inc. #	Tm (°C)	Th (°C)	Max X _{CO2}	Max X _{NaCl}
A1	3	0.0		0.0	0.0
	6	-0.1		0.00097	0.00052
	7	0.0	154	0.0	0.0
	8	-0.1		0.00097	0.00052
A2	1	-0.6		0.0058	0.0031
	2	-0.6		0.0058	0.0031
	4	-0.2		0.0019	0.0010
	4.5	-0.6	188	0.0058	0.0031
	8	-0.3		0.0029	0.0016
	12	-0.3		0.0029	0.0016
A3	2	0.0	154	0.0	0.0
	3	0.0	159	0.0	0.0
	4		165		
	5	0.0		0.0	0.0
B1	45	-0.3		0.0029	0.0016
	46	-0.3		0.0029	0.0016
	47.1		131		
	47.2		159		
	47.3		161		
	47.4		160		
	50	-0.3		0.0029	0.0016
	52	-0.5		0.0048	0.0026
	52.1		150		
	52.2		182		

Table 3, continued.

Chip #	Fluid Inc. #	Tm (°C)	Th (°C)	Max X _{CO2}	Max X _{NaCl}
B1	54.1	-0.3		0.0029	0.0016
	54.2	-0.3	174	0.0029	0.0016
	54.3	-0.3		0.0029	0.0016
	54.8		154		
	54.9	-0.3	138	0.0029	0.0016
	55	-0.2		0.0019	0.0010
	55.5	-0.2		0.0019	0.0010
	67	-0.3		0.0029	0.0016
B4	4		143		
	4.5	-0.3	128	0.0029	0.0016
	5	-0.3	119	0.0029	0.0016
	5.5		136		
	6.5		129		
	7		132		
	7.5		122		
	17	-0.3	168	0.0029	0.0016
	18		154		
	19	-0.3	155	0.0029	0.0016
	20	-0.3	139	0.0029	0.0016
	21		146		
	22		150		
	23	-0.3	151	0.0029	0.0016
	24	-0.2	169	0.0019	0.0010

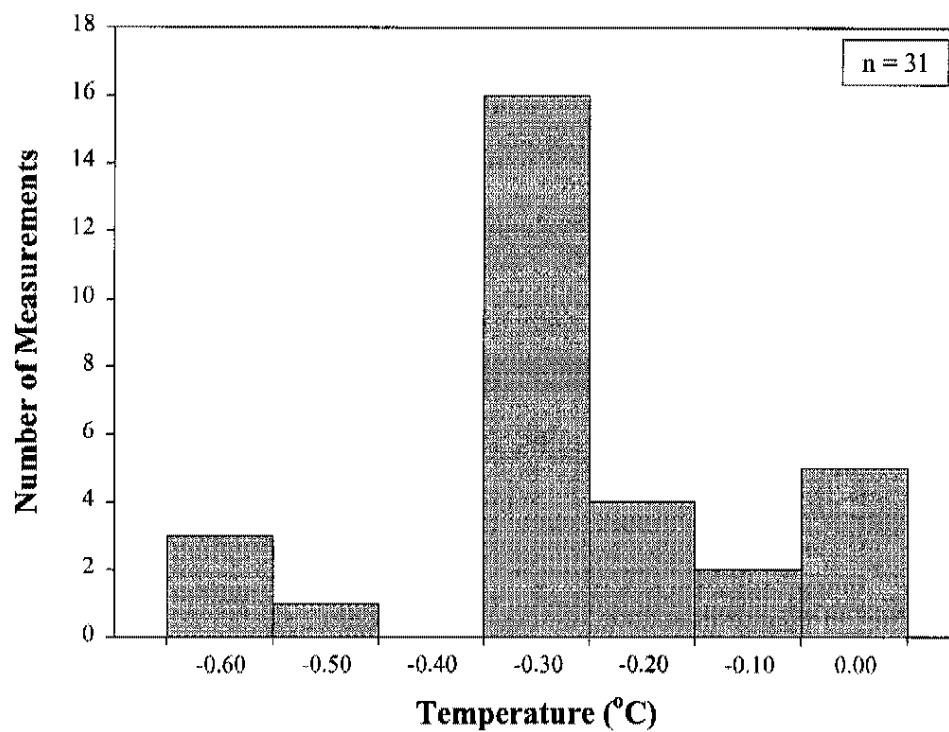


Figure 5-1. Final ice melting temperatures in fluid inclusions.

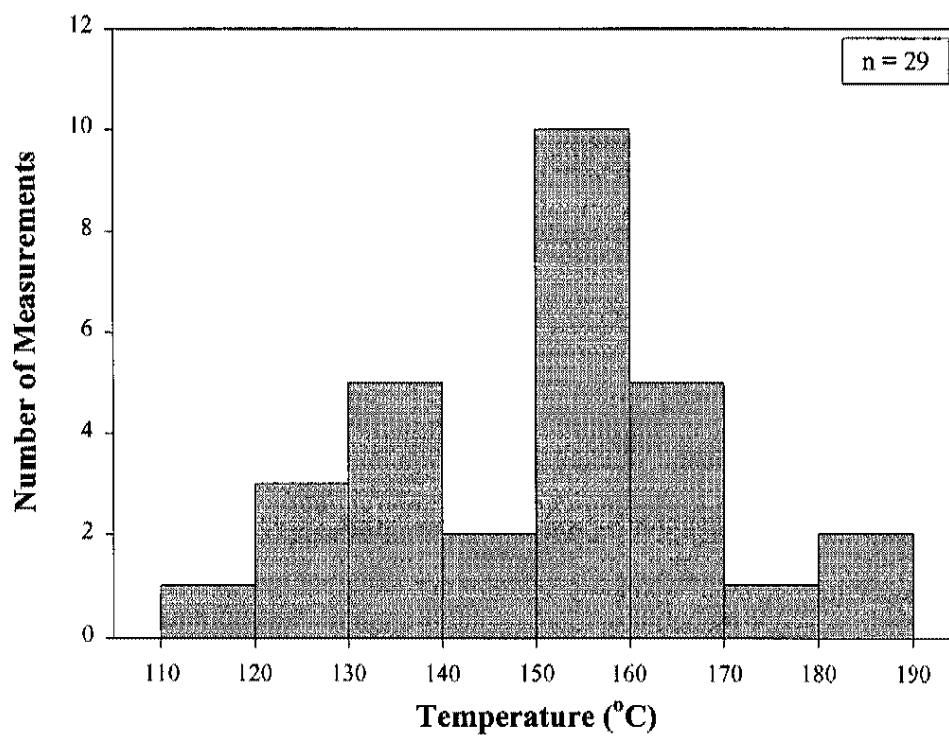


Figure 5-2. Fluid inclusion homogenization temperatures.

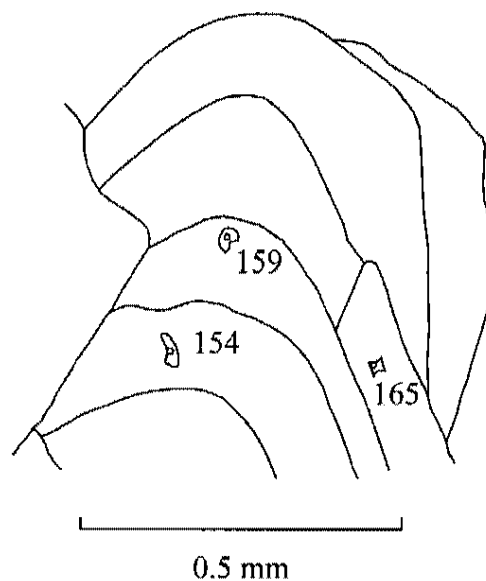


Figure 5-3. Sketch of growth-zoned crystal from chip A3, showing homogenization temperatures (in °C) from fluid inclusions in different growth zones.

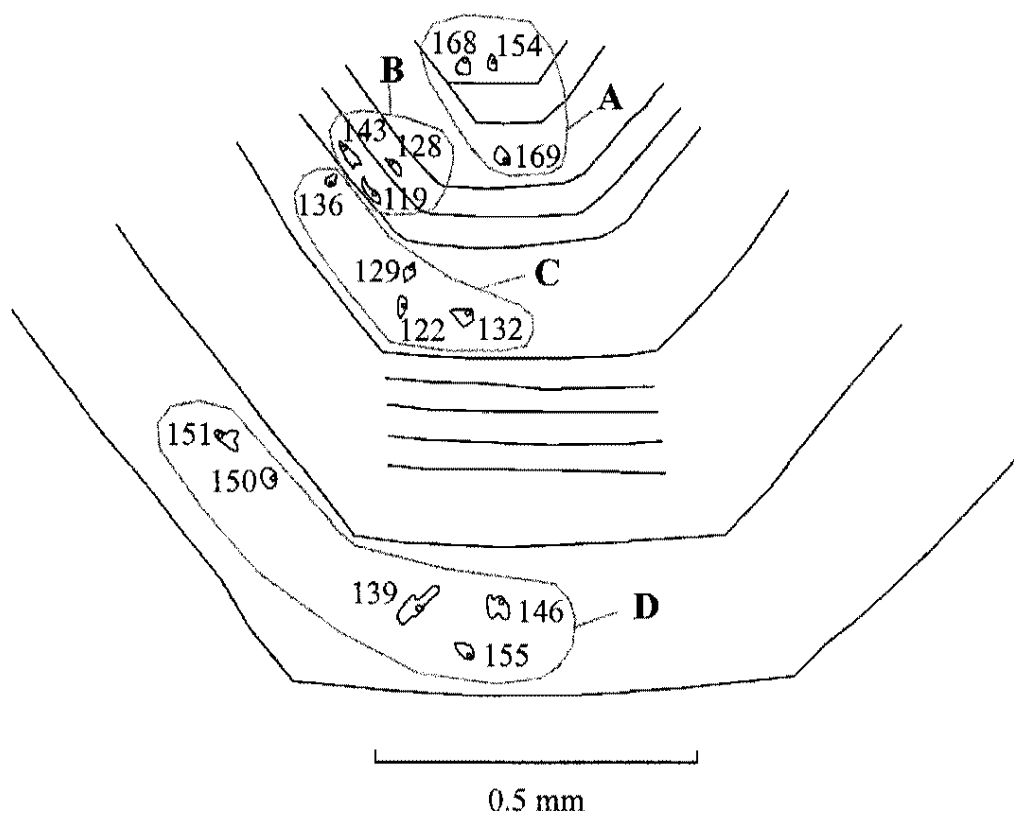


Figure 5-4. Sketch of growth-zoned crystal from chip B-4, showing homogenization temperatures (in °C) in groups of fluid inclusions from different growth zones.

CHAPTER 6

THERMODYNAMIC MODELING

Estimation of Pressure, Temperature, and X_{CO_2}

Significance of Chalcedony

The presence of chalcedony in veins at Devil Peak has very important implications for the temperature of alteration and the interpretation of thermodynamic diagrams.

Fournier (1985) describes the behavior of silica in hydrothermal fluids. Chalcedony precipitates from hydrothermal fluids only at temperatures below 180°C. If chalcedony precipitates and the temperature of the fluid subsequently increases above 180°C, the chalcedony will convert to crystalline quartz. If quartz is deposited at temperatures above 180°C and the temperature drops below 180°C, the quartz will convert to chalcedony.

The texture of the chalcedony in the veins at Devil Peak indicates it precipitated directly from solution, as discussed in Chapter 4. Because the chalcedony formed early in the paragenetic sequence and did not recrystallize to crystalline quartz, the temperature of the hydrothermal fluid during and after mineral deposition must have been less than 180°C.

Pressure and X_{CO_2}

While the presence of chalcedony in veins gives a known maximum temperature of 180°C, no similar, precise estimate for either the pressure or the X_{CO_2} exists. Fluid inclusion analysis suggests that the X_{CO_2} of the hydrothermal fluid is very low, but this may not be true throughout the entire sequence of mineral deposition. If the rhyolites and rhyolite breccia in the map area are surface flows, the pressure of the system is probably less than 100 bars (pers. comm., E. I. Smith, 1998). Thus some of the diagrams are calculated at $X_{\text{CO}_2} = 0.01$, the lowest possible X_{CO_2} the CORK (Compensated Redlich-Kwong) equation of Holland and Powell (1991) will allow, and at $P = 100$ bars, the best estimate for maximum pressure available.

Temperature- X_{CO_2} Diagrams

Calculated at fixed pressure, temperature- X_{CO_2} diagrams show the reactions that may occur among stable phases and phase assemblages at specific pressure, temperature, and X_{CO_2} conditions. As the conditions change, existing phase assemblages can react to form new phase assemblages. These diagrams are useful for placing constraints on the P-T- X_{CO_2} conditions of the system based on which phases are present.

Temperature- X_{CO_2} diagrams were constructed at 1 bar and 100 bars pressure (Figures 6-1 and 6-2, respectively). At first glance, several features of the diagrams appear to restrict the pressure and X_{CO_2} of the hydrothermal fluid. Closer inspection of the diagrams reveals that these variables cannot be adequately limited.

According to Figures 6-1 and 6-2, serpentine is stable only within the field formed by reactions 4 and 6. The intersection of these reactions denotes the maximum X_{CO_2} at

which serpentine is stable, and thus suggests a maximum X_{CO_2} for the hydrothermal fluid. The X_{CO_2} at which the intersection occurs, however, is proportional to the pressure. At 1 bar, the intersection occurs at $X_{\text{CO}_2} = 0.25$, while at 100 bars, the intersection occurs at $X_{\text{CO}_2} = 0.4$. Thus, to place a reasonable limit on the X_{CO_2} , the actual pressure of alteration must be known.

The presence of both hydromagnesite and brucite in veins suggests that the equilibrium P-T- X_{CO_2} conditions for reaction 7 may have been reached. Because a maximum temperature is known, reaction 7 can be used to determine the X_{CO_2} if the pressure can be estimated. Figures 6-1 and 6-2 show that for this reaction, when $T = 180^\circ\text{C}$, pressure and X_{CO_2} are inversely proportional. Thus the lowest possible pressure of 1 bar indicates a maximum X_{CO_2} of 0.16 for the hydrothermal fluid, assuming that reaction 7 occurred. Evidence presented later in this chapter, however, indicates the hydromagnesite can also precipitate from solution. The presence of hydromagnesite, then, does not necessarily indicate that reaction 7 occurred.

The T- X_{CO_2} diagrams do show that reactions forming replacement periclase, forsterite, and brucite could not have occurred at Devil Peak because the reactions proceed at temperatures higher than 180°C (at reasonable X_{CO_2} values). Periclase will form from dolomite by reaction 1 at temperatures above 300°C , and from brucite by reaction 2 at temperatures as low as 165°C (but at unreasonably high X_{CO_2} for this system)(Figure 6-1). The lowest temperatures at which forsterite can form are 210°C by reaction 5, and 135°C by reaction 4 (at unreasonably high X_{CO_2}) (Figure 6-1). The X_{CO_2} generally remains below 0.2 in hydrothermal fluids (Holland and Malinin, 1979); at lower X_{CO_2} values, reactions 2 and 4 occur at temperatures well above 180°C . Brucite will form

from dolomite and water by reaction 8, but only at temperatures significantly above 180°C (Figures 6-1 and 6-2). Reaction 8 is not stable at 1 bar pressure (Figure 6-1) because reaction 1 would consume all dolomite present, leaving none to react with water to form brucite. Nevertheless, even if reaction 8 could occur at 1 bar, brucite would form only at temperatures of 360°C or higher.

Mineral Stability Diagrams

Constructed at constant pressure and temperature, mineral stability diagrams show how the solubility of minerals varies with X_{CO_2} and the activities of major ions. They are useful for determining the conditions under which minerals will precipitate from solution or dissolve. Several diagrams at the same pressure and X_{CO_2} can be combined to form a single diagram that shows how the mineral stability fields change with changing temperature. For the diagrams used in this study, the variables $\log a\text{Mg}^{2+}/(a\text{H}^+)^2$ and $\log a\text{H}_4\text{SiO}_4$ were chosen as axes.

Conditions of Mineral Precipitation

Figure 6-3, calculated at 1 bar pressure and $X_{\text{CO}_2} = 0.01$, shows that brucite will precipitate at temperatures as low as 135°C. Increasing either the pressure or the X_{CO_2} will increase the lowest temperature at which brucite will precipitate (Figures 6-4 and 6-5). Forsterite and periclase will precipitate at temperatures as low as 180°C and 260°C, respectively, (Figure 6-3), and at higher temperatures at increased pressure and X_{CO_2} (Figures 6-4 and 6-5).

It is unlikely that forsterite ever precipitated at Devil Peak because the conditions for its formation are highly restricted. The lowest temperature at which forsterite will

form (180°C) is the highest possible temperature that the hydrothermal fluid could have reached. Furthermore, because the temperature at which forsterite will precipitate increases with any increase in pressure or X_{CO_2} , for forsterite to have precipitated at Devil Peak the pressure must have been no more than 1 bar and the X_{CO_2} must have been 0.01 or less. Periclase forms at temperatures well above 180°C, and therefore could not have precipitated at Devil Peak.

In Figure 6-3, the hydromagnesite field is overlapped by portions of the brucite and serpentine fields. In the overlapped area the hydromagnesite and brucite/serpentine fields share the same ionic activities; thus in this area temperature is the only factor governing whether hydromagnesite or brucite/serpentine will precipitate. When the ionic conditions plot within the overlapped area, at temperatures below 135°C hydromagnesite will precipitate, and at temperatures above 135°C brucite or serpentine will precipitate. For periclase, forsterite, talc, and quartz (chalcedony), and for hydromagnesite, brucite, and serpentine at higher pressure, the minerals that will precipitate are determined by the activities of the major ions in addition to the temperature.

Hydrothermal Fluid Composition and Evolution

The mineral stability diagrams also show the possible changes in the composition of the hydrothermal fluid indicated by the paragenetic sequence. Chalcedony formed early in the sequence, followed by serpentine, brucite, and hydromagnesite, as discussed in Chapter 4. This sequence suggests that during mineral deposition the hydrothermal fluid may have contained more silica early and more Mg^{2+} later. The mineral stability diagrams allow a more detailed exploration of the chemical evolution of the hydrothermal fluid.

A change in precipitation from chalcedony to serpentine could have been caused by an increase in the activity of Mg^{2+} and/or a decrease in pH (Figures 6-3, 6-4, and 6-5), by a decrease in the activity of silica if precipitation occurred at relatively high X_{CO_2} and/or pressure (Figures 6-4 and 6-5), or simply by a decrease in pressure (Figures 6-3 and 6-4). The shift from precipitation of serpentine to brucite probably resulted from a decrease in the activity of silica (Figures 6-3, 6-4, and 6-5), but could also have resulted from an increase in $a\text{Mg}^{2+}$ and/or a decrease in pH at low X_{CO_2} and pressure (Figure 6-3). A shift in precipitation from brucite to hydromagnesite could have been caused by a decrease in temperature in addition to an increase in $a\text{Mg}^{2+}$ and/or a decrease in pH (Figures 6-4 and 6-5), by an increase in X_{CO_2} (Figures 6-4 and 6-5), or as discussed previously, simply by a decrease in temperature at low X_{CO_2} and pressure (Figure 6-3).

As discussed above, fluctuations in the activity of silica in the hydrothermal fluid can cause shifts between the precipitation of brucite and serpentine. The fact that serpentine is most commonly associated with rhyolite breccia suggests that the rhyolite may have introduced enough silica into the hydrothermal fluid to allow serpentine (rather than brucite) to precipitate.

Implications of Thermodynamic Modeling Results

The low alteration temperature at Devil Peak is very unusual for hydrothermal systems containing brucite, and may be a factor in this rare occurrence of open-space brucite. The alteration temperatures for most brucite occurrences are estimated to have been at least 500 - 600°C (e.g., Adamello, Italy (Bucher-Nurminen, 1982); Pine Creek, California (Brown et al., 1985); and Notch Peak, Utah (Nabelek et al., 1984)), and

commonly reached 700 - 800°C (e.g. Crestmore, California (Carpenter, 1967), and Stephen Cross Quarry, Quebec, Canada (Cartwright and Weaver, 1993)). All of these localities contain brucite after periclase, and Crestmore also contains brucite after dolomite. But, as discussed above, periclase could not have formed at Devil Peak, and brucite replaces dolomite only at temperatures above 360°C. At temperatures below 180°C, brucite can form only by direct precipitation from solution.

Summary and Conclusions

The presence of open-space chalcedony in the veins indicates that the temperature of the hydrothermal fluid during and after mineral deposition was less than 180°C. The thermodynamic diagrams reveal no definite pressure or X_{CO_2} limits, but the possible conversion of brucite to hydromagnesite by reaction 7 may limit the X_{CO_2} to ≤ 0.16 .

The thermodynamic diagrams indicate that periclase could not have been present at Devil Peak, because the reactions that form it from other phases occur at temperatures higher than 180°C or at unreasonably high X_{CO_2} for this system, and because it precipitates only at temperatures above 180°C. It is also very unlikely that forsterite was present at Devil Peak because the reactions that form it from other phases occur at temperatures higher than 180°C or at unrealistically high X_{CO_2} for this system. Furthermore, forsterite precipitates only if $T \geq 180^\circ\text{C}$, $P = 1$ bar, and $X_{\text{CO}_2} \leq 0.01$. These highly restricted conditions are implausible at Devil Peak.

The thermodynamic diagrams provide further evidence that the brucite at Devil Peak precipitated from solution into open space. The temperature- X_{CO_2} diagrams show that brucite forms from other phases only at temperatures above 180°C or at unreasonably

high X_{CO_2} for this system. Furthermore, the T - X_{CO_2} and mineral stability diagrams indicate that periclase, the mineral that brucite most commonly replaces, could not have been present at Devil Peak.

Chalcedony precipitated early in the paragenetic sequence, followed by serpentine, brucite, and hydromagnesite, suggesting that during mineral deposition the hydrothermal fluid contained more silica early and more Mg^{2+} later. The mineral stability diagrams show that fluctuations the temperature, pressure, X_{CO_2} , and pH of the hydrothermal fluid also could have influenced the paragenetic sequence.

In most other localities, brucite formed as a replacement mineral in systems with alteration temperatures above 500°C . At Devil Peak, however, the alteration temperatures were so low that brucite could form only by precipitation from solution. Thus the low alteration temperature may partially explain the rare occurrence of open-space brucite at Devil Peak.

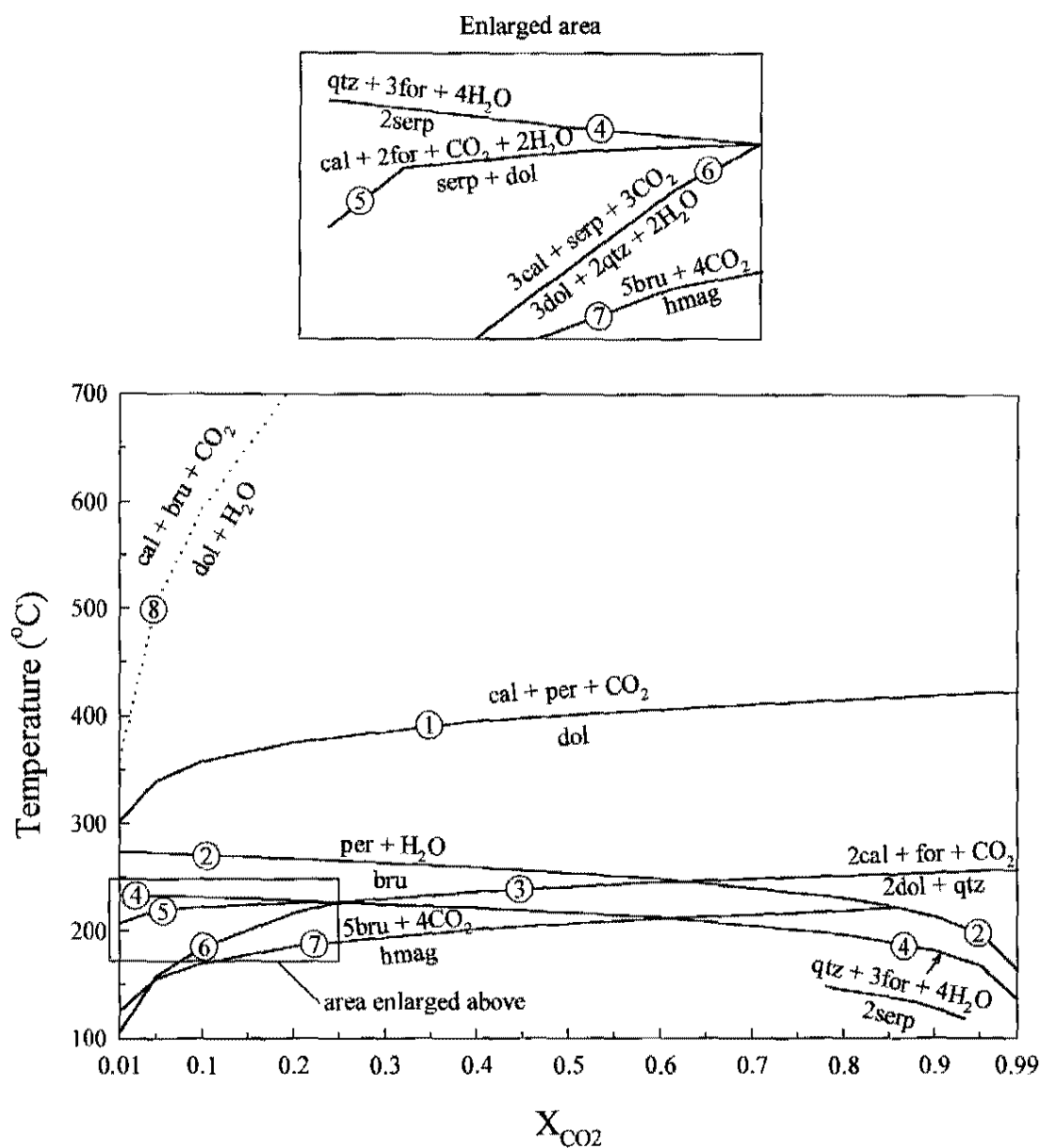


Figure 6-1. T - X_{CO_2} diagram at $P = 1$ bar. Abbreviations: bru = brucite, cal = calcite, dol = dolomite, for = forsterite, hmag = hydromagnesite, per = periclase, serp = serpentine, qtz = quartz. Reaction 8 is dotted because it is unstable. Enlarged area is vertically exaggerated.

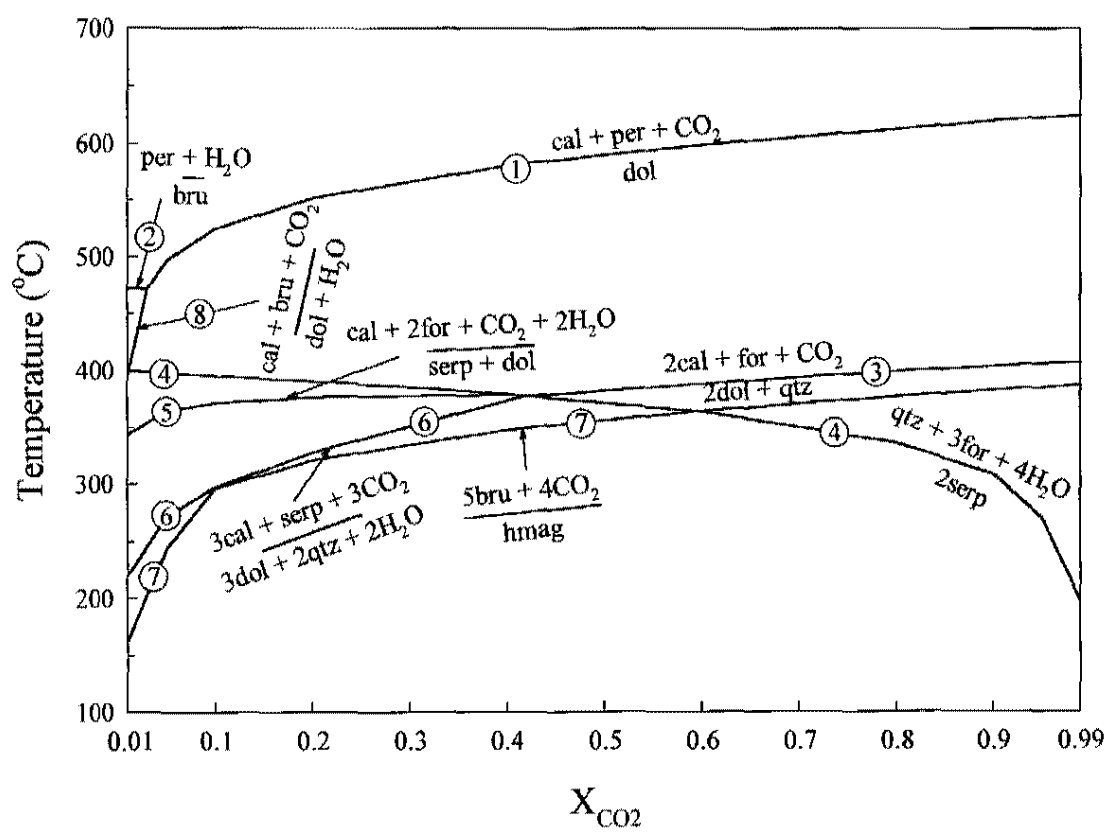


Figure 6-2. T-X_{CO2} diagram at 100 bars.

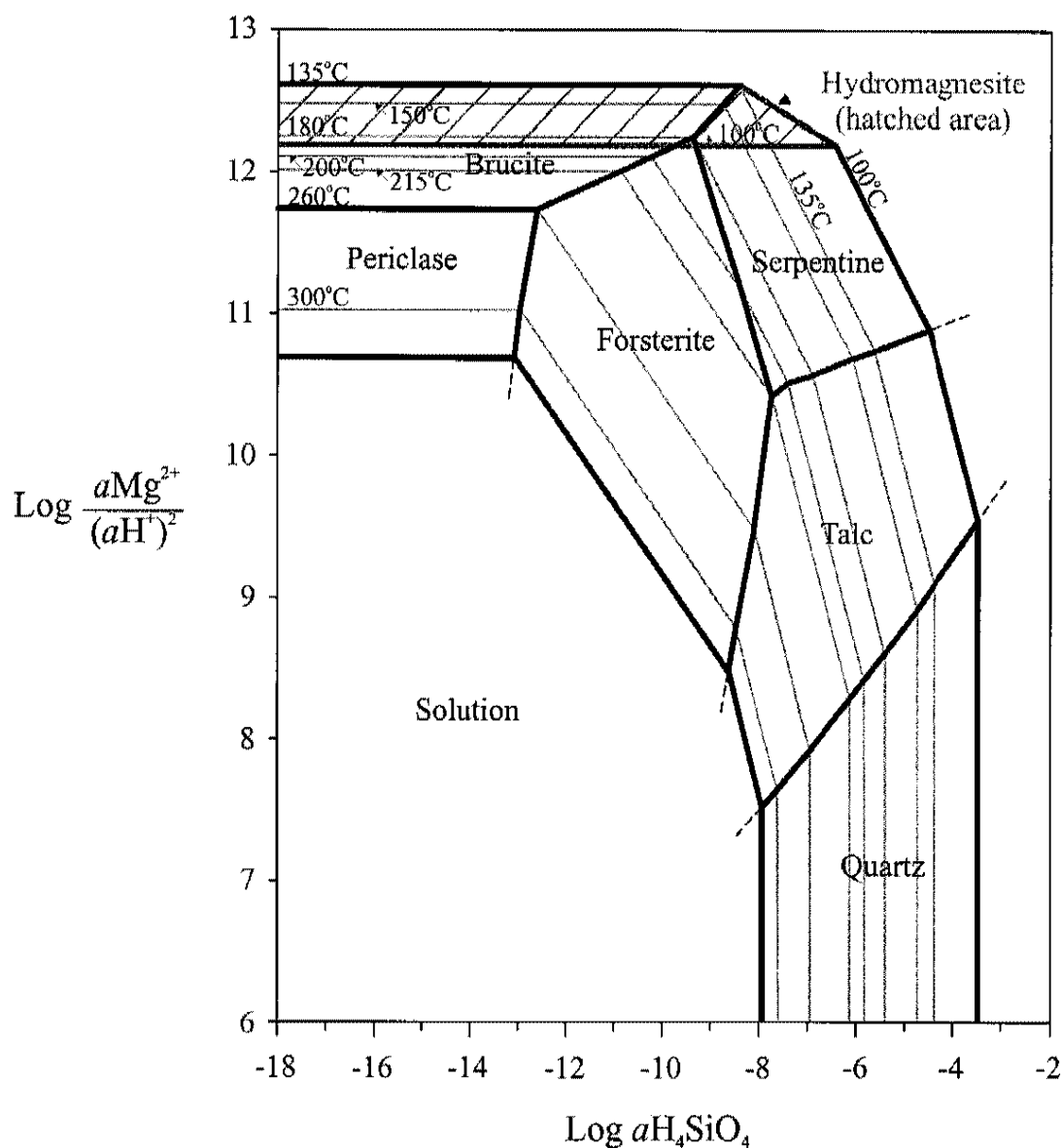


Figure 6-3. Mineral stability diagram at 1 bar, $X_{\text{CO}_2} = 0.01$, and various temperatures. The hydromagnesite field (hatched, in gray) is overlapped by portions of the brucite and serpentine fields (outlined in black). In the overlapped area, at temperatures below 135°C hydromagnesite will precipitate, and at temperatures above 135°C brucite or serpentine will precipitate.

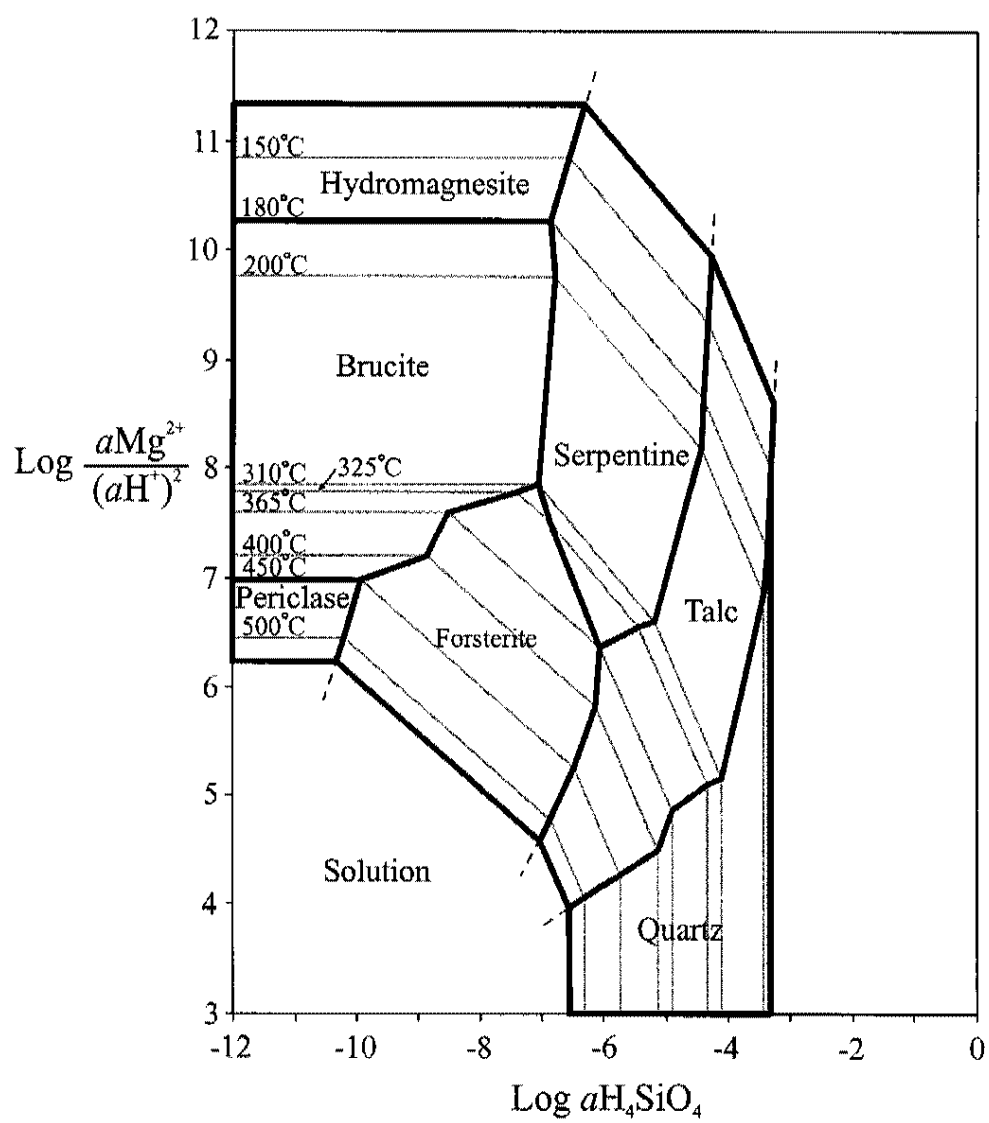


Figure 6-4. Mineral stability diagram at 100 bars, $X_{\text{CO}_2} = 0.01$, and various temperatures.

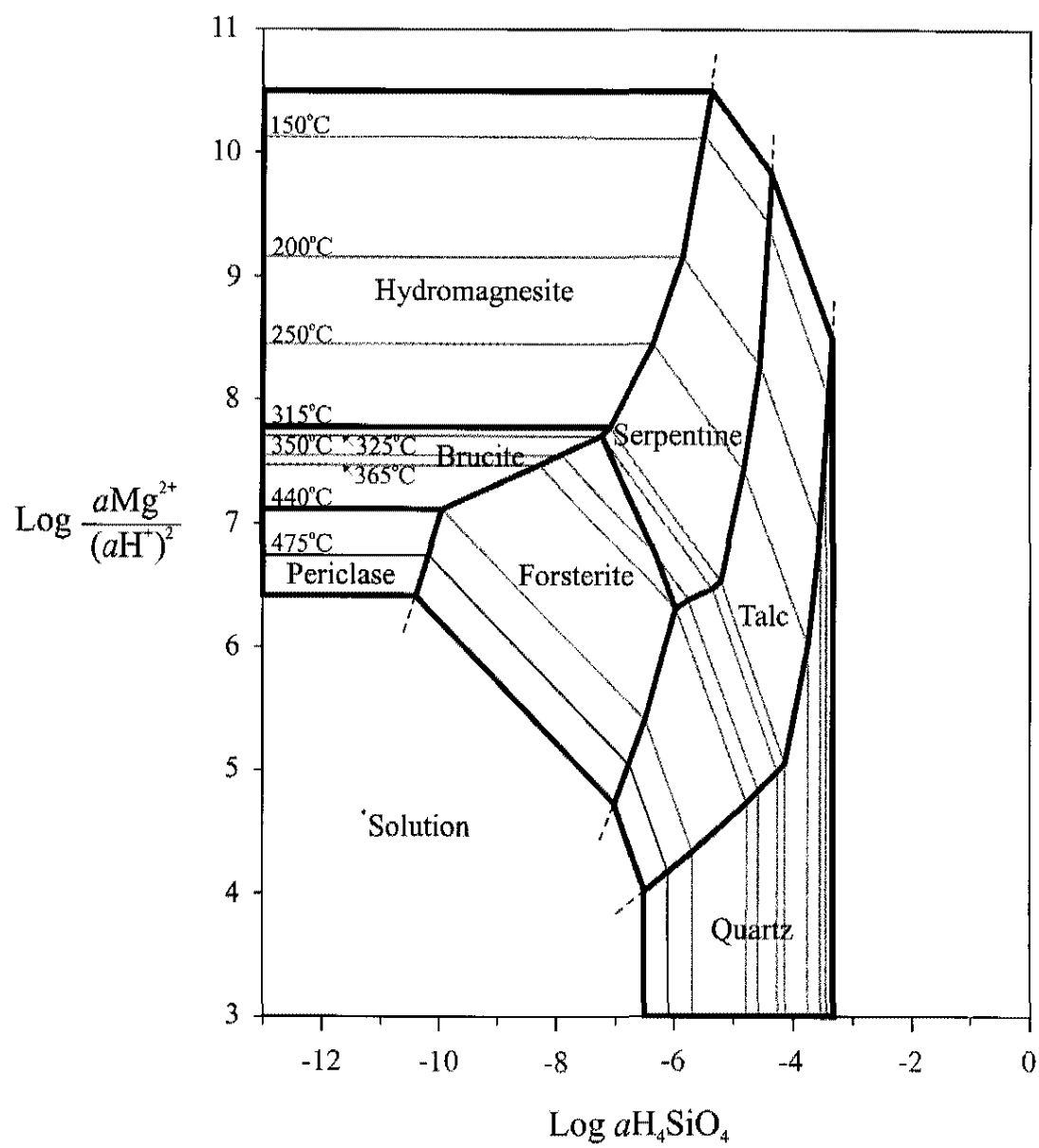


Figure 6-5. Mineral stability diagram at 100 bars, $X_{\text{CO}_2} = 0.1$, and various temperatures.

CHAPTER 7

STABLE ISOTOPE ANALYSIS

Preliminary Interpretation of Results

Sample Groups

The results of C and O stable isotope analyses of five unaltered limestones, two partly altered limestones, three highly altered limestones, one highly altered vein-margin limestone, and three calcite separates from veins are listed in Table 7-1. The samples comprise four groups that are characterized by similar stable isotope signatures and similar degrees of alteration (Figure 7-1). Group 1 contains samples of unaltered Monte Cristo Limestone with $\delta^{18}\text{O}$ and $\delta^{13}\text{C}$ averaging 23.6‰ and 2.2‰, respectively. Group 2 samples are partly altered limestones that have stable isotope signatures of $\delta^{18}\text{O} = 17.2$ to 17.7‰ and $\delta^{13}\text{C} = 0.1$ to 0.8‰. Group 3 is comprised of highly altered limestones collected from inside the adits, and also contains one sample (DPL30a) collected from within 5 mm of a vein. Group 3 samples have stable isotope signatures ranging from 8.0 to 12.3‰ for $\delta^{18}\text{O}$ and -2.1 to -3.3‰ for $\delta^{13}\text{C}$. Group 4 contains calcite crystals separated from vein samples that were collected from within the adits. Stable isotope signatures for group 4 samples are about 18.0‰ for $\delta^{18}\text{O}$ and -3.6 to -6.5‰ for $\delta^{13}\text{C}$.

Relationships Among Sample Groups

Figure 7-1 reveals two important relationships among the sample groups. The first is a trend of decreasing $\delta^{13}\text{C}$ and $\delta^{18}\text{O}$ in the limestone samples (groups 1, 2, and 3) that correlates with increasing degree of alteration (Figure 7-2). The second is the high $\delta^{18}\text{O}$ signatures of the vein calcites (group 4) relative to the highly altered limestones (group 3) (Figure 7-1). The causes and implications of these relationships are discussed in detail in this chapter.

Mg-Metasomatism

Ten of the fourteen samples that were sent for stable isotope analysis were also analyzed by X-ray fluorescence spectrometry. The results show that groups 1 and 2 are essentially pure limestones, but group 3 samples are dolostones (Table 7-2). Because group 1 samples are unaltered limestones that represent the parent rock for both group 2 and group 3 samples, the dolomitization of group 3 samples must be secondary; i.e., a result of Mg-metasomatism. Mg-metasomatism is also manifested by the deposition of Mg-bearing minerals in veins that crosscut the highly altered wall rocks.

Possible Explanations for the Stable

Isotope Signatures

Possible Explanations for the Depletion Trend

In the depletion trend in Figure 7-2, $\delta^{18}\text{O}$ decreases by approximately 13‰ and $\delta^{13}\text{C}$ decreases by about 6‰. Such large depletions in the stable isotope signatures are

common in contact metamorphosed carbonate rocks, and can usually be explained by Rayleigh decarbonation or infiltration by hydrothermal fluids, or both (Valley, 1986).

Rayleigh Decarbonation

Contact metamorphism of carbonate rocks produces volatiles that increase the pressure of the system, resulting in fracturing and subsequent release of the volatiles. Rayleigh decarbonation occurs if the devolatilization reactions produce CO₂ that is immediately released from the system, either by escape through fractures or flushing with water. Because ¹³C and ¹⁸O preferentially enter the CO₂ phase (relative to ¹²C and ¹⁶O, respectively), the stable isotope signatures of the remaining wall rocks become depleted in ¹³C and ¹⁸O. The effects of Rayleigh decarbonation on wall rock isotopic signatures can be modeled using the equation:

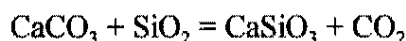
$$\delta_r^f = (\delta_r^i + 1000)(F^{\alpha-1}) - 1000$$

where δ_r^f = the final isotopic signature of the wall rock, δ_r^i = the initial isotopic signature of the wall rock, α = the fractionation factor between the wall rock and CO₂, and F = the fraction of carbon remaining in the wall rock.

Use of this equation to model Rayleigh decarbonation requires the adoption of two assumptions: (1) that the temperature remained constant during decarbonation (i.e., α remained constant), and (2) that the CO₂ released during decarbonation escaped immediately. The probability of the temperature of any hydrothermal system remaining constant during decarbonation is low, but this assumption can be circumvented by calculating the isotopic depletion caused by Rayleigh decarbonation at a variety of

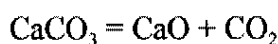
temperatures and comparing the results. In highly fractured, shallow level rocks such as those at Devil Peak, immediate escape of the CO₂ is a valid assumption.

Rayleigh decarbonation is usually modeled in calc-silicate rocks. In these types of rocks, Rayleigh decarbonation can explain large depletions in $\delta^{13}\text{C}$ but not in $\delta^{18}\text{O}$ because of the “calc-silicate limit” described by Valley (1986). The formation of wollastonite and CO₂ from calcite and quartz demonstrates the maximum possible extent of decarbonation in calc-silicate rocks:



As decarbonation occurs, all of the carbon escapes as CO₂, while only 40% of the oxygen enters the CO₂ phase. Wollastonite retains 60% of the oxygen atoms, thus limiting decarbonation to $F_{\text{oxygen}} = 0.6$, and limiting changes in $\delta^{18}\text{O}$ to only a few per mil.

Rayleigh decarbonation can cause larger $\delta^{18}\text{O}$ shifts only in rare cases when decarbonation occurs in the absence of silica by the reaction



(Valley, 1986). In this case, only 33% of the oxygen atoms remain in the wall rock, allowing decarbonation to proceed until $F_{\text{oxygen}} = 0.33$, and resulting in larger $\delta^{18}\text{O}$ depletions.

Chemical analysis by XRF (Table 7-2) shows very little silica in the Devil Peak limestone samples, indicating that silicate-absent decarbonation likely occurred here. Figure 7-3 shows curves illustrating how silicate-absent decarbonation at 200°C, 300°C, and 500°C would affect the $\delta^{13}\text{C}$ and $\delta^{18}\text{O}$ signatures in wall rocks with the starting composition of the group 1 (unaltered limestone) samples. The tie lines show F_{carbon}

remaining in the wall rock. For silicate-absent decarbonation, F_{carbon} is related to F_{oxygen} by the equation

$$F_{\text{carbon}} = 1.5 * F_{\text{oxygen}} - 0.5$$

as discussed in Appendix III.

Figure 7-3 shows that even silicate-absent Rayleigh decarbonation cannot be solely responsible for the large $\delta^{18}\text{O}$ and $\delta^{13}\text{C}$ shifts at Devil Peak. The curves show that Rayleigh decarbonation at around 200 - 300°C might explain the low $\delta^{13}\text{C}$ and $\delta^{18}\text{O}$ signatures in the wall rocks after extensive decarbonation, but the wall rocks have not lost that much CO_2 . The fraction of carbon remaining in the wall rock samples can be calculated from the XRF data:

$$F_{\text{carbon}} = 1 - [(\text{CaO} + \text{MgO} - \text{LOI})/(\text{CaO} + \text{MgO})],$$

where LOI is assumed to be CO_2 . The results are shown in Table 7-3. The most decarbonation exhibited by any of the samples is 38% ($F_{\text{carbon}} = 0.62$ in sample DPL33); not enough to cause a significant decrease in the stable isotope signatures.

Infiltration

Infiltration of wall rocks by a hydrothermal fluid with a different isotopic composition will cause the isotopic signature of the wall rocks to change as exchange occurs between the fluid and rock (Valley, 1986). If the $\delta^{13}\text{C}$ and $\delta^{18}\text{O}$ signatures of the infiltrating fluid are lower than the those of the wall rock, the wall rock signatures will decrease with increasing fluid-rock interaction. Infiltrating fluids with higher $\delta^{13}\text{C}$ and $\delta^{18}\text{O}$ will increase the isotopic signatures of the wall rock.

The Mass-Balance (Box) Model for Isotope

Exchange During Infiltration

Taylor (1974, 1977) proposed a zero-dimensional model (box model) for calculating the effects of infiltrating fluids on wall rock stable isotope signatures in closed systems, using a mass-balance equation:

$$F\delta_{fl}^i + R\delta_r^i = F\delta_{fl}^f + R\delta_r^f$$

where F = the atom percent of fluid oxygen or carbon in the total system, R = the atom percent of exchangeable rock oxygen or carbon in the bulk system, δ_{fl}^i and δ_r^i = initial δ value in the fluid and rock, respectively, and δ_{fl}^f and δ_r^f = final δ value in the fluid and rock, respectively, after exchange. This equation can be rearranged into a more useful form (Appendix III):

$$F/R_{closed} = (\delta_r^f - \delta_r^i) / (\delta_{fl}^i - \delta_r^f + \Delta_{r-fl}),$$

where $\Delta = \delta_r^f - \delta_{fl}^f = 1000 \ln \alpha$ (α = the fractionation factor between the mineral and fluid) and F/R is the “fluid to rock ratio,” or the ratio of the atom percent of fluid oxygen in the total system to the atom percent of exchangeable rock oxygen in the bulk system. To characterize an open system, Taylor (1977) proposed integrating the equation for closed systems to give:

$$F/R_{open} = \ln(F/R_{closed} + 1),$$

which considers repeated infiltration by infinitely small portions of fluid (Appendix III).

In Taylor’s closed systems, a single constant volume of fluid and a single constant volume of rock simultaneously equilibrate (Nabelek, 1991). In Taylor’s open systems,

infinitely small volumes of fluid equilibrate with a given volume of rock and then leave the system (Valley, 1986).

These equations allow calculation of fluid to rock ratios for a particular rock sample given a starting and ending isotopic signature for the rock sample and an ending isotopic signature for the fluid. The isotopic effects on wall rock signatures resulting from infiltration by a fluid with a given isotopic signature can also be modeled using Taylor's equations.

Use of the mass-balance method requires four assumptions: (1) that isotopic equilibrium occurred between the fluid and rocks; (2) that the fractionation factor, and therefore the temperature and modal composition of the system, remained constant; (3) that the isotopic signature of the infiltrating fluid remained constant (for open systems) or that the volume of fluid remained constant (for closed systems); and (4) that the volume of infiltrated rock was homogenous.

Baumgartner and Rumble (1988) and Ferry (1989) have questioned the usefulness and validity of these equations because: (1) the equations contain no space or time coordinates to provide information regarding the spatial or temporal evolution of the system, (2) a fluid to rock ratio does not give much insight into actual fluid volumes (i.e., the equations give no absolute fluid fluxes), and (3) the equations take into account only fluid flow that had a perceptible effect on the system.

The main concern of critics of the mass-balance method is that fluid to rock ratios are commonly presented as actual fluid volumes. In reality, the fluid to rock ratios might best be considered a measure of the extent of isotope exchange, because the assumption of rock homogeneity is unrealistic, and because fluids that do not cause changes in wall rock

signatures are not taken into account. Critics also question the usefulness of models that do not consider the direction or absolute volume of fluid flow.

Not all researchers are harshly critical of Taylor's equations. Blattner and Lassey (1990) defend the mass-balance method, retorting that the model should not be dismissed simply because it does not deal with fluid fluxes and flow direction. Blattner and Lassey (1990) note that many geochemical models, including phase-rule applications, do not encompass directional flow because the models implicitly assume zero-dimensional, fixed volumes of rock where the contents of the unit volume are considered thoroughly mixed. They contend that the mass-balance approach is still useful if the limitations are kept in mind. Nabelek (1991) agrees, pointing out that Taylor's equations are actually a general form of a mixing equation and are therefore still useful for estimating fluid sources. Baumgartner and Rumble (1988) do concede that the equations are effective in estimating the X_{CO_2} of fluids in simple systems (i.e., systems involving exchange between calcite and an $\text{H}_2\text{O}-\text{CO}_2$ fluid).

Because of the concerns discussed above, no attempts have been made in this study to quantify the volume of water that flowed through the rocks at Devil Peak. Instead, the mass-balance model was used to estimate X_{CO_2} values of the infiltrating fluid and to identify possible fluid sources.

Whether to model an open or closed system is an additional question. Nabelek (1991) points out that the open system model requires the isotopic composition of the infiltrating fluid to remain constant, which is unlikely. On the other hand, the closed system model does not allow the addition or escape of any fluids, which is also unrealistic.

The true behavior of a hydrothermal system is probably somewhere in between, therefore both open and closed systems were modeled in this study.

The Mass-Balance Model Applied to Devil Peak: Special Considerations

During contact metamorphism, interactions between wall rock and infiltrating fluid usually result in decreasing $\delta^{13}\text{C}$ and $\delta^{18}\text{O}$ in the wall rock. Figure 7-4 shows measured $\delta^{18}\text{O}$ and $\delta^{13}\text{C}$ depletion trends from 16 different stable isotope studies compiled by Valley (1986), as well as the depletion trend at Devil Peak. Generally, as alteration increases, the $\delta^{18}\text{O}$ and $\delta^{13}\text{C}$ signatures in the wall rocks decrease from normal marine limestone values toward the “carbonatite box,” or “igneous calcite,” the isotopic signature of calcite deposited in equilibrium with magmatic fluids. Calcites separated from veins within the altered wall rocks also commonly plot in or near the carbonatite box, at the end of the wall rock depletion trend (e.g., Deines and Gold, 1969; Sverjensky, 1981; Brown et al., 1985; Taylor and Bucher-Nurminen, 1986).

A comparison of the Devil Peak depletion trend with the 16 other depletion trends in Figure 7-4 suggests that the Devil Peak depletion trend results from infiltration of the wall rocks by a hydrothermal fluid with a low $\delta^{13}\text{C}$ and $\delta^{18}\text{O}$ signature. Unlike the majority of the studies Valley compiled, however, the vein calcites (group 4) at Devil Peak do not plot in or near the carbonatite box. Rather, they plot away from the carbonatite box at much higher $\delta^{18}\text{O}$ values (Figure 7-2). Thus a model describing the isotopic effects of infiltration at Devil Peak must consider high $\delta^{18}\text{O}$ values in the vein calcites as well as decreased $\delta^{18}\text{O}$ values in the altered wall rocks.

There are two possible explanations for the elevated $\delta^{18}\text{O}$ signatures in the vein calcites. One is that the calcites were deposited at lower temperatures by the same fluid that depleted the wall rocks. This is unlikely, however, because low temperature deposition would have increased the $\delta^{13}\text{C}$ signatures as well as the $\delta^{18}\text{O}$ signatures of the vein calcites. The other possible explanation is that the vein calcites were deposited by a fluid with a higher $\delta^{18}\text{O}$ signature than the fluid that depleted the wall rocks. This explanation engenders the additional question of the origin of the higher $\delta^{18}\text{O}$ fluid. One possibility is that isotopic exchange between the early infiltrating fluid and the carbonate wall rock increased the $\delta^{18}\text{O}$ signature of the fluid. This is probably not the case, because exchange between the early infiltrating fluid and the carbonate wall rock should also have increased the $\delta^{13}\text{C}$ signatures of the fluid and hence the vein calcites, but the vein calcites have the lowest $\delta^{13}\text{C}$ signatures of all the samples. Most likely the higher $\delta^{18}\text{O}$ fluid resulted from a mixture of the initial infiltrating fluid with a high $\delta^{18}\text{O}$ fluid after initial depletion of the wall rocks. This explanation may be supported by the $\delta^{18}\text{O}$ signature of DPL30a, a sample of limestone collected along a vein margin (within 5 mm of the vein). The $\delta^{18}\text{O}$ value of DPL30a is at least 2‰ higher than the $\delta^{18}\text{O}$ values of the other highly altered limestones (Table 7-1, Figure 7-2). An evolved, higher $\delta^{18}\text{O}$ fluid that resulted from a mixture of the existing low $\delta^{13}\text{C}$ and $\delta^{18}\text{O}$ fluid and an invading high $\delta^{18}\text{O}$ fluid could have deposited calcite with relatively high $\delta^{18}\text{O}$ values in veins, while increasing the previously depleted $\delta^{18}\text{O}$ signature of the vein margin limestone.

Use of the mass-balance model for infiltration at Devil Peak is complicated by the addition of a high $\delta^{18}\text{O}$ fluid and by Mg-metasomatism. The addition of a high $\delta^{18}\text{O}$ fluid

violates the assumption of constant fluid composition (for open systems) and constant fluid volume (for closed systems), and dolomitization of the highly altered wall rocks violates the implicit assumption of constant modal composition. Nonetheless, the infiltration causing the depletion trend can be modeled as long as the results are interpreted with the effects of these complications kept in mind.

Addition of a High $\delta^{18}\text{O}$ Fluid

If the added high $\delta^{18}\text{O}$ fluid increased the $\delta^{18}\text{O}$ signature of the vein margin limestone, the fluid may also have increased the previously depleted $\delta^{18}\text{O}$ values of the other highly altered limestone samples. Thus the $\delta^{18}\text{O}$ signatures of the highly altered samples (and hence of the modeled early, low $\delta^{13}\text{C}$ and $\delta^{18}\text{O}$ fluid) should be considered maximums.

Effects of Dolomitization

There are two possible scenarios that may describe the dolomitization of the highly altered limestone (group 3) samples. The first is that dolomitization began after the high $\delta^{18}\text{O}$ fluid mixed completely with the early, low $\delta^{13}\text{C}$ and $\delta^{18}\text{O}$ fluid. In this case, the signatures imparted by the early fluid on the group 3 samples would have been set in calcite that was later changed to dolomite. The second scenario is that dolomitization began before the high $\delta^{18}\text{O}$ fluid was added, or as it was just beginning to mix with the early fluid. In this case, the signatures imparted by the early fluid on the group 3 samples would have been set in rock that was partly or entirely dolomite. Fortunately, the means of compensating for both of these scenarios is the same. In the first scenario, subsequent

dolomitization of the group 3 samples after their signatures were set in calcite would increase their $\delta^{18}\text{O}$ signatures (because $\Delta_{\text{dol-H}_2\text{O}} > \Delta_{\text{cc-H}_2\text{O}}$ for ^{18}O) but decrease their $\delta^{13}\text{C}$ signatures (because $\Delta_{\text{dol-H}_2\text{O}} < \Delta_{\text{cc-H}_2\text{O}}$ for ^{13}C). To allow for this, the $\delta^{18}\text{O}$ signatures of the samples (and thus the modeled early fluid) should be considered maximums, and the $\delta^{13}\text{C}$ signatures of the samples (and the modeled early fluid) should be considered minimums. In the second scenario, the signatures would have been set in rock that is partly or entirely dolomite. Because $\Delta_{\text{dol-H}_2\text{O}} > \Delta_{\text{cc-H}_2\text{O}}$ for ^{18}O , but $\Delta_{\text{dol-H}_2\text{O}} < \Delta_{\text{cc-H}_2\text{O}}$ for ^{13}C , the same fluid will impart a higher $\delta^{18}\text{O}$ and a lower $\delta^{13}\text{C}$ signature in dolomites than in calcites. Here again, the $\delta^{18}\text{O}$ signatures of the samples (and the early modeled fluid) should be considered maximums, and the $\delta^{13}\text{C}$ signatures of the samples (and the early modeled fluid) should be considered minimums.

Mass-Balance Method Results

Infiltration by the early fluid was modeled at 100°C, 300°C, and 500°C for both open and closed systems. A starting isotopic composition and CO_2 content were chosen for the infiltrating fluid and used to solve the mass-balance equations. The results were graphed, producing a curve that represented the depletion in the stable isotope signatures of the wall rocks that would be caused by the modeled infiltrating fluid. The isotopic composition and CO_2 content of the infiltrating fluid were varied until a best fit curve duplicated the observed depletion trend in the altered wall rocks (e.g., Figure 7-5). The results of the mass-balance modeling are listed in Table 7-4. Depending on temperature, a fluid with a minimum $\delta^{13}\text{C} = -1.5$ to -7.4‰ , a maximum $\delta^{18}\text{O} = 8.0$ to -8.0‰ , and

$X_{\text{CO}_2} = 0.15 - 0.16$ would be required to cause the isotopic depletion in the Devil Peak wall rock samples. The differences in results between open and closed systems were relatively small for $\delta^{18}\text{O}$ and very small to non-existent for X_{CO_2} and $\delta^{13}\text{C}$.

With the mass-balance method, the modeled X_{CO_2} decreases with increased curvature of a trend (Figure 7-6). Combined dolomitization and infiltration by a late, high $\delta^{18}\text{O}$ fluid would result in increased $\delta^{18}\text{O}$ but decreased $\delta^{13}\text{C}$ in the wall rock as described above, which in turn would result in more curvature to the depletion trend. The X_{CO_2} indicated by modeling is therefore considered a minimum.

Implications of Modeling Results for Origin of Vein Calcites

The modeling results confirm that the high $\delta^{18}\text{O}$ values of the group 4 calcites are not simply a result of low temperature deposition by the same fluid that initially depleted the wall rock. The isotopic signatures that hypothetical vein calcites would have if deposited at low temperatures by the modeled early fluids were calculated using the equation:

$$\delta_{\text{cal}} = [(\delta_{\text{fl}} + 1000)/\alpha_{\text{fl-cal}}] - 1000$$

where $\alpha_{\text{fl-cal}}$ is the fractionation factor between the fluid and calcite for ^{13}C or ^{18}O , and δ_{fl} and δ_{cal} are the $\delta^{13}\text{C}$ values or $\delta^{18}\text{O}$ values of the fluid and calcite, respectively (Appendix III). The results of the calculations are listed in Table 7-5. At low temperatures, the modeled early infiltrating fluid could have deposited calcite with the same $\delta^{18}\text{O}$ signatures as the group 4 samples, but the $\delta^{13}\text{C}$ signatures would be too high (Figure 7-7). The vein

calcites must have been deposited by a fluid with an isotopic composition different from that of the early infiltrating fluid.

The isotopic signature of the fluid that would have deposited calcite with the $\delta^{13}\text{C}$ and $\delta^{18}\text{O}$ values of the group 4 vein calcites can be calculated using the same equation that was used for the hypothetical calcite calculations, but rearranged:

$$\delta_{\text{fl}} = (\alpha_{\text{fl-cc}})(\delta_{\text{cc}} + 1000) - 1000.$$

The isotopic signature of a fluid in equilibrium with group 4 calcites was calculated at 100°C and 200°C, resulting in a range of -9.9‰ to -3.2‰ for $\delta^{13}\text{C}$ and 0.5‰ to 8.7‰ for $\delta^{18}\text{O}$ (Table 7-6).

The modeled isotopic signatures of the fluid that depleted the wall rocks and the calculated isotopic signatures of the fluid that deposited the vein calcites are compared in Figure 7-8. The calculated $\delta^{18}\text{O}$ values of the fluid that deposited the vein calcites are systematically higher than the modeled $\delta^{18}\text{O}$ values of the fluid that depleted the wall rocks, supporting the conclusion that a high $\delta^{18}\text{O}$ fluid was added to the system after the wall rocks were depleted.

Hydrothermal Fluid Source and Evolution

The hydrothermal fluid at Devil Peak could have been composed of one or more of the following types of fluids: magmatic fluids released during crystallization, fluids produced by metamorphic decarbonation and dehydration reactions at depth or in adjacent country rocks, and meteoric water. Because their different derivations impart different stable isotope signatures to each of the fluids, possible fluid sources can be identified if the

stable isotope signature of a hydrothermal fluid is known or estimated. Ranges in stable isotope signatures for the different types of fluids are compiled in Table 7-7.

Figure 7-9 shows the modeled isotopic signature ranges of the early infiltrating fluid, the calculated isotopic signature ranges of the fluid that deposited the vein calcites, and the established isotopic signature ranges of the three possible sources for the hydrothermal fluid. The diagram indicates that the early infiltrating fluid may have been a mixture of metamorphic fluid and meteoric water. The diagram also shows that an influx of either magmatic fluid or metamorphic water (with no carbon) could have shifted the $\delta^{18}\text{O}$ values of the early infiltrating fluid enough to match those of the late, evolved fluid that deposited the calcite.

An influx of late metamorphic water or magmatic fluid may explain the difference in X_{CO_2} indicated by the fluid inclusion analysis and the mass-balance modeling. The early infiltrating fluid may have been relatively CO_2 -rich due to decarbonation of the host rocks. The stable isotope signature of the vein calcite analyzed for the fluid inclusion study indicates that it was deposited by the late, evolved fluid. The addition of magmatic fluid or metamorphic water to the early infiltrating fluid could have diluted the CO_2 concentration, resulting in a much lower CO_2 content in the fluid that deposited the calcite containing the fluid inclusions.

A metamorphic component in the early infiltrating fluid is not surprising considering that the host rocks are carbonates; the metamorphic C and O could have entered the hydrothermal fluid by Rayleigh decarbonation of the limestones. A late influx of magmatic or metamorphic fluid is unusual. One possible explanation for the late influx of high $\delta^{18}\text{O}$ fluid is that the gray rhyolite dike and the Devil Peak plug intruded at

different times. For example, the gray rhyolite dike may have intruded first and initiated hydrothermal alteration. The Devil Peak plug may have intruded later, releasing magmatic fluids into the hydrothermal system after the isotopic signatures of the wall rocks had already been depleted.

Another possibility is that the hydrothermal system was invaded by rising metamorphic water released during contact metamorphism of the country rock at depth by the Devil Peak intrusion or a related unexposed intrusion. Rocks that could yield metamorphic water from dehydration reactions occur in a number of units that underlie the Monte Cristo Limestone in the southern Spring Mountains. The Valentine Limestone Member of the Sultan Limestone, which directly underlies the Monte Cristo Limestone, contains silty and sandy beds (Carr and Pinkston, 1987). The Goodsprings Dolomite contains silty dolomite and brown shale (Carr, 1978; Carr and Pinkston, 1987). A wedge of Precambrian to Cambrian shales, quartzites, and sandstones that is up to 3 km thick underlies the Bonanza King Limestone (which correlates with units 1 and 2 in the Goodsprings Dolomite (Carr and Pinkston, 1987)) in the central Spring Mountains (Secor, 1962), and likely extends to the southern Spring Mountains.

Mg Source

The rocks underlying the Monte Cristo Limestone are the most likely source for the Mg^{2+} in the hydrothermal fluid. The Sultan Limestone and the Goodsprings Dolomite both contain abundant layers of dolomite (Carr, 1978; Carr and Pinkston, 1987). Fluids released from metamorphic dehydration and decarbonation reactions at depth or from the

ascending Devil Peak intrusion could remove Mg^{2+} from the dolomitic units and carry it upward to the Monte Cristo limestone.

Summary and Conclusions

Data from the stable isotope analysis falls into four groups representing unaltered limestones (group 1), partly altered limestones (group 2), highly altered limestones (group 3), and vein calcites (group 4). The highly altered limestone samples have been dolomitized. The data show two important characteristics. One is the trend of decreasing $\delta^{13}\text{C}$ and $\delta^{18}\text{O}$ values in the limestones that corresponds to increasing degree of alteration, and the other is the high $\delta^{18}\text{O}$ signatures of the vein calcites relative to the highly altered limestones.

Depletion trends like the one seen in the Devil Peak wall rocks are usually caused by Rayleigh decarbonation, infiltration by a hydrothermal fluid, or both. Rayleigh decarbonation could not have been responsible for the decrease in the isotopic signatures because the wall rocks have not lost enough CO_2 . Infiltration of the wall rocks by a hydrothermal fluid with a low $\delta^{13}\text{C}$ and $\delta^{18}\text{O}$ signature can explain the depletion trend.

The relatively high $\delta^{18}\text{O}$ signatures of the vein calcites are most likely the result of deposition of the calcites by a fluid with a higher $\delta^{18}\text{O}$ signature than the fluid that initially depleted the wall rocks. The fluid that deposited the calcites was probably formed by mixing of the initial infiltrating fluid with a high $\delta^{18}\text{O}$ fluid that invaded the hydrothermal cell.

The isotopic signatures and X_{CO_2} of the early, low $\delta^{18}\text{O}$ and $\delta^{13}\text{C}$ fluid responsible for the depletion trend can be modeled using the mass-balance method, but the modeling is

complicated by the dolomitization of the group 3 samples and by the influx of the late, high $\delta^{18}\text{O}$ fluid. To compensate, the calculated $\delta^{18}\text{O}$ values of the fluid are considered maximums, and the calculated $\delta^{13}\text{C}$ and X_{CO_2} values are considered minimums. Modeling results indicate that, depending on temperature, the infiltrating fluid responsible for the depletion trend had a maximum $\delta^{18}\text{O}$ signature of -8.0‰ to 8.0‰, a minimum $\delta^{13}\text{C}$ signature of -7.4‰ to -1.5‰, and a minimum X_{CO_2} of 0.15 to 0.16.

The $\delta^{13}\text{C}$ and $\delta^{18}\text{O}$ values of the fluid that deposited the vein calcites were also calculated. The $\delta^{13}\text{C}$ values ranged from -9.9‰ to -3.2‰, and the $\delta^{18}\text{O}$ values ranged from 0.5‰ to 8.7‰, depending on temperature. These $\delta^{18}\text{O}$ values are approximately 8‰ higher than those of the modeled early infiltrating fluid, thus suggesting that a high $\delta^{18}\text{O}$ fluid was added to the early infiltrating fluid.

A comparison of the modeled early infiltrating fluid signatures with the established isotopic signature ranges of possible fluid sources suggests that early infiltrating fluid was a mixture of meteoric water and metamorphic fluid. An influx of either magmatic fluid or metamorphic water (with no carbon) could have increased the $\delta^{18}\text{O}$ signature of the early infiltrating fluid enough to deposit vein calcites with the $\delta^{18}\text{O}$ signatures of the group 4 samples. Dilution of the CO_2 in the early infiltrating fluid by an influx of magmatic fluid or metamorphic water may explain the lower X_{CO_2} in the vein calcite determined by fluid inclusion analysis.

Possible sources of late magmatic fluid include the Devil Peak plug or the gray rhyolite stock. Late metamorphic water could have originated at depth from contact metamorphism of underlying shales and impure limestones and dolomites by the Devil

Peak plug or by a related, unexposed intrusion. Dolomitic layers in the rocks underlying the Monte Cristo Limestone are the most likely source for the Mg^{2+} in the hydrothermal fluid.

Table 7-1. Results of C and O stable isotope analysis of Devil Peak samples. St. Dev. = standard deviation, ls = limestone.

Sample #	$\delta^{13}\text{C}$ (‰)	St. Dev.	$\delta^{18}\text{O}$ (‰)	St. Dev.	Sample Type	Group
DPL34	2.035	0.063	24.509	0.100	unaltered ls	1
DPUC6	2.388	0.029	24.127	0.098	unaltered ls	1
DP24	1.954	0.034	23.678	0.048	unaltered ls	1
DPU2	2.598	0.030	23.379	0.036	unaltered ls	1
DPL35	1.805	0.055	22.362	0.055	unaltered ls	1
DPU3	0.050	0.047	17.680	0.044	partly altered ls	2
DPUA25	0.783	0.041	17.169	0.085	partly altered ls	2
DPL31	-2.746	0.072	10.456	0.089	highly altered ls	3
DPL33	-3.329	0.069	10.119	0.128	highly altered ls	3
DPUA24	-2.072	0.033	9.033	0.081	highly altered ls	3
DPL30a	-3.322	0.066	12.316	0.080	vein margin ls	3
DPL30	-4.444	0.039	18.396	0.164	vein calcite	4
DPL26	-3.600	0.150	18.300	0.073	vein calcite	4
DPUA22	-6.537	0.028	17.728	0.088	vein calcite	4

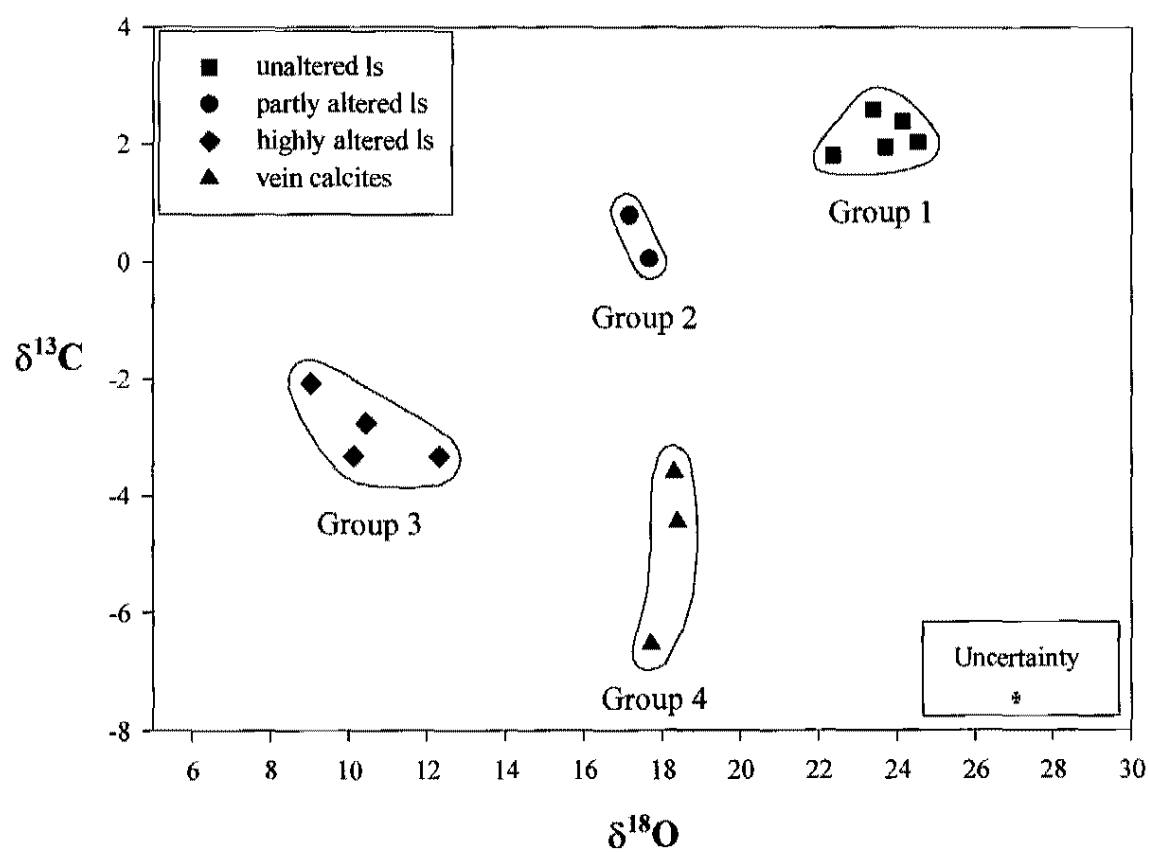


Figure 7-1. Results of stable isotope analysis of Devil Peak samples. ls = limestone.

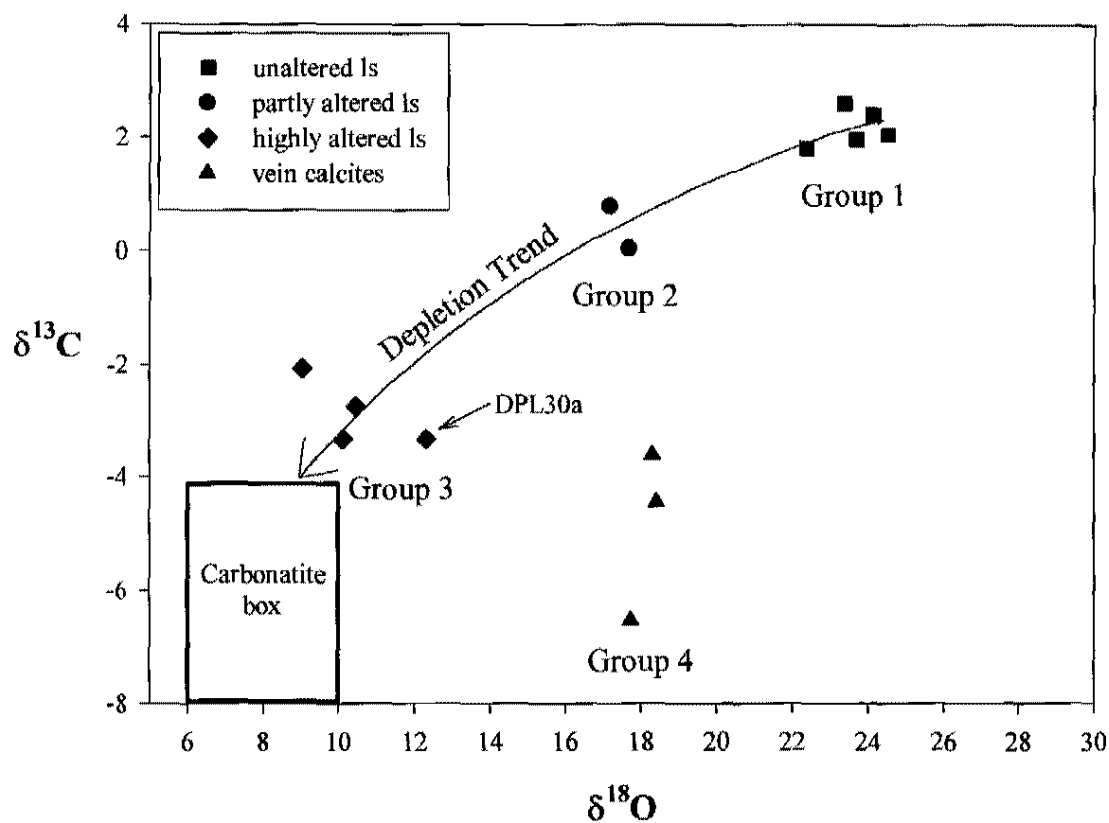


Figure 7-2. The important relationships among sample groups include a depletion trend in the limestone samples and high $\delta^{18}\text{O}$ values in the vein limestones (group 4) relative to the highly altered limestones (group 3). DPL30a is a vein margin limestone sample. The carbonatite box represents the $\delta^{13}\text{C}$ and $\delta^{18}\text{O}$ values of calcite formed from or in equilibrium with igneous fluid (Valley, 1986).

Table 7-2. Results of X-ray fluorescence analysis of Devil Peak limestone and altered limestone samples. The detection limit and precision for each element is 0.01% and 5%, respectively. LOI = loss on ignition.

Sample	Type	Group	Al ₂ O ₃ %	CaO %	Fe ₂ O ₃ %	MgO %	SiO ₂ %	LOI %	Total %
DP24	unaltered ls	1	0.22	53.70	<0.01	1.65	0.23	43.78	99.61
DPL34	unaltered ls	1	0.27	54.65	<0.01	0.44	0.81	43.37	99.58
DPL35	unaltered ls	1	0.27	54.75	<0.01	0.47	0.40	43.28	99.21
DPU2	unaltered ls	1	0.25	54.94	<0.01	0.33	1.06	43.20	99.80
DPUC6	unaltered ls	1	0.21	54.96	<0.01	0.35	0.74	43.25	99.53
DPU3	partly altered ls	2	0.91	55.12	0.83	0.99	3.67	38.27	99.99
DPUA25	partly altered ls	2	0.34	54.87	<0.01	0.75	0.97	42.65	99.62
DPL31	highly altered ls	3	0.20	36.64	<0.01	23.82	0.10	38.73	99.53
DPL33	highly altered ls	3	0.20	35.26	0.01	25.39	1.34	37.71	99.94
DPUA24	highly altered ls	3	0.24	36.71	0.27	22.72	0.28	39.61	99.85

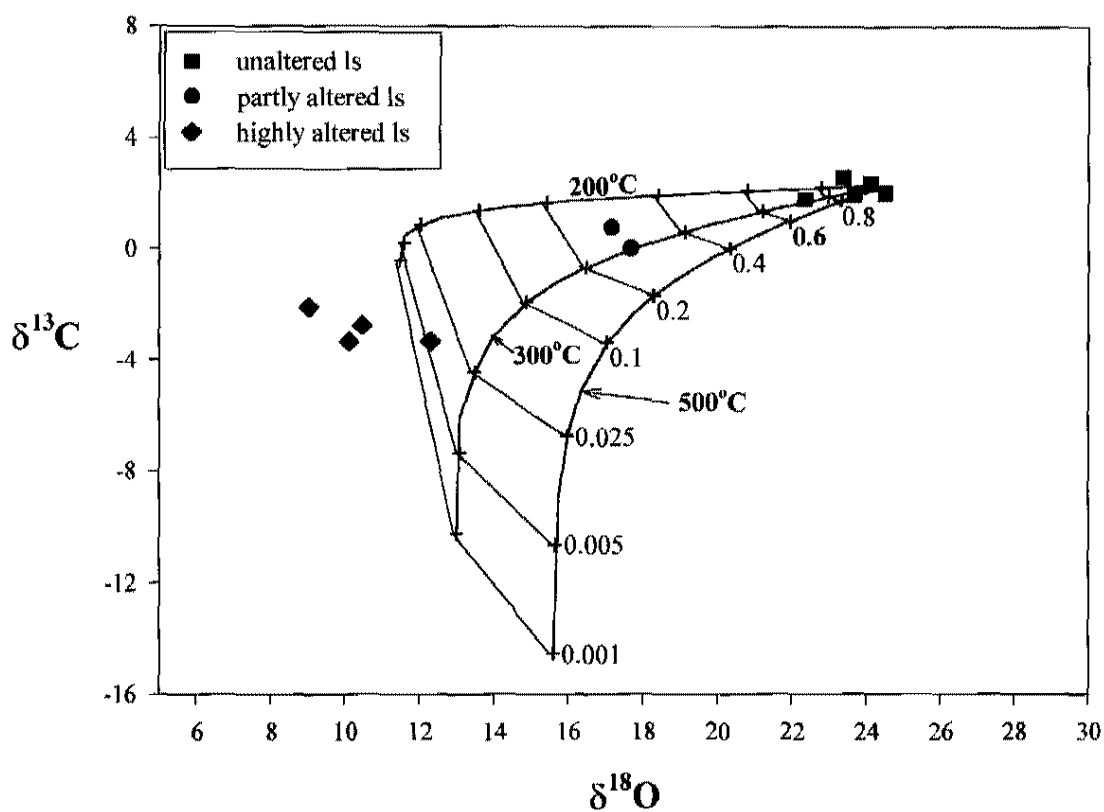


Figure 7-3. Silicate-absent Rayleigh decarbonation trend calculated at 200°C, 300°C, and 500°C. Tie lines show the fraction of carbon (F_{carbon}) remaining in the rock.

Table 7-3. F_{carbon} (fraction of carbon) remaining in wall rock samples.

Sample #	F_{carbon}	Sample Type	Group
DPL33	0.62	highly altered limestone	3
DPL31	0.64	highly altered limestone	3
DPUA24	0.67	highly altered limestone	3
DPU3	0.68	partly altered limestone	2
DPUA25	0.77	partly altered limestone	2
DPL35	0.78	unaltered limestone	1
DPU2	0.78	unaltered limestone	1
DPUC6	0.78	unaltered limestone	1
DP24	0.79	unaltered limestone	1
DPL34	0.79	unaltered limestone	1

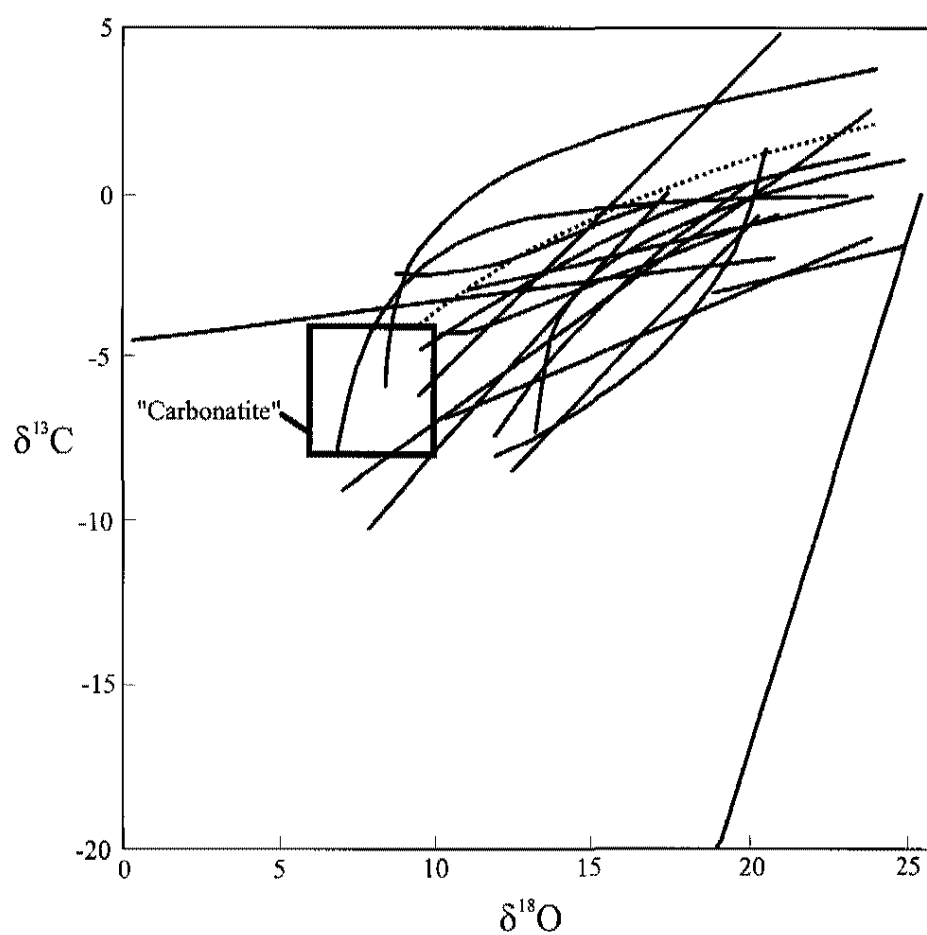


Figure 7-4. Measured $\delta^{13}\text{C}$ and $\delta^{18}\text{O}$ depletion trends from 17 stable isotope studies. Solid lines represent studies compiled by Valley (1986). Dotted line is depletion trend in Devil Peak wall rock samples. Most curves trend toward the carbonatite box. Modified from Valley (1986).

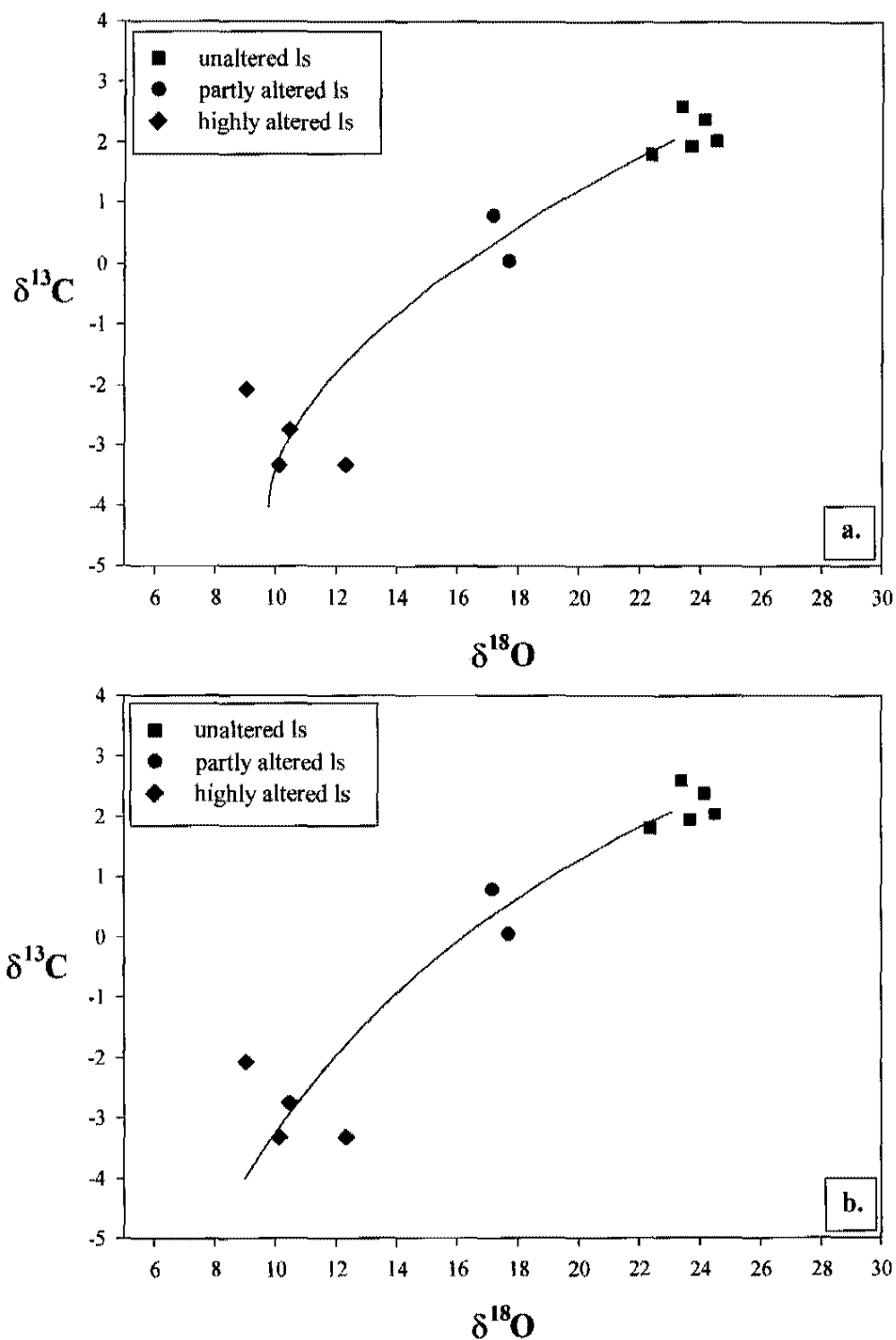


Figure 7-5. Curves representing modeled $\delta^{13}\text{C}$ and $\delta^{18}\text{O}$ depletions in wall rock signatures caused by infiltration at 300°C in (a) open and (b) closed systems. For open system, infiltrating fluid $\delta^{13}\text{C} = -2.2$, $\delta^{18}\text{O} = 4.2$, and $X_{\text{CO}_2} = 0.16$. For closed system, infiltrating fluid $\delta^{13}\text{C} = -2.2$, $\delta^{18}\text{O} = 3.4$, and $X_{\text{CO}_2} = 0.15$. Initial wall rock $\delta^{13}\text{C} = 2.4$ and $\delta^{18}\text{O} = 24.5$.

Table 7-4. Stable isotope signature and X_{CO_2} of early infiltrating fluid estimated by mass-balance modeling.

System	Temperature ($^{\circ}\text{C}$)	$\delta^{13}\text{C}$ (‰)	$\delta^{18}\text{O}$ (‰)	X_{CO_2}
open	100	-7.4	-7.3	0.16
closed	100	-7.3	-8.0	0.15
open	300	-2.2	4.2	0.16
closed	300	-2.2	3.4	0.15
open	500	-1.5	8.0	0.16
closed	500	-1.5	7.2	0.15

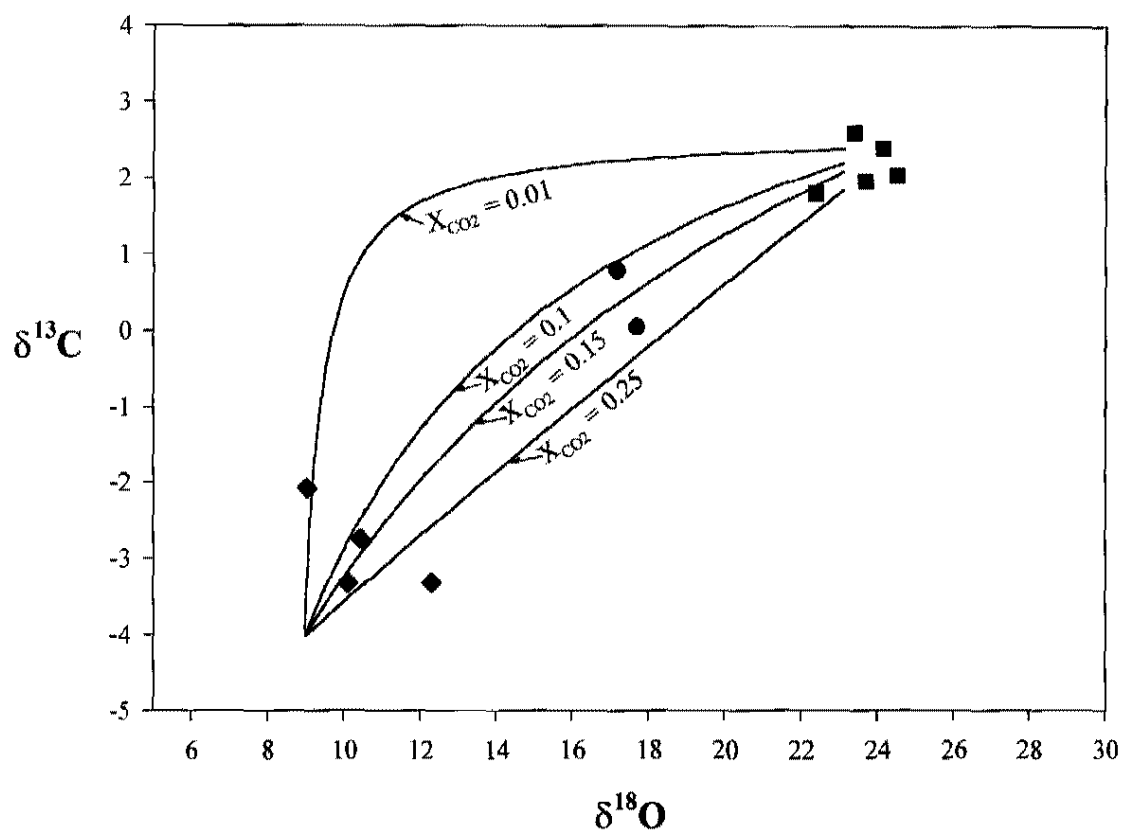


Figure 7-6. Decrease in curvature of modeled wall rock signatures with increase in X_{CO_2} of infiltrating fluid. Curves are for infiltration in a closed system at 300°C , with infiltrating fluid $\delta^{13}\text{C} = -2.2$ and $\delta^{18}\text{O} = 3.4$, and initial wall rock $\delta^{13}\text{C} = 2.4$ and $\delta^{18}\text{O} = 24.5$.

Table 7-5. Calculated $\delta^{13}\text{C}$ signatures of hypothetical vein calcites deposited by the modeled infiltrating fluids. T ($^{\circ}\text{C}$) required is the temperature required for the modeled fluid to deposit calcite with $\delta^{18}\text{O} = 18.0$, the approximate $\delta^{18}\text{O}$ signature of the group 4 vein calcites. $\delta^{13}\text{C}$ is the $\delta^{13}\text{C}$ value of hypothetical calcite deposited by the modeled fluid at the temperature listed in column 2. The calculated $\delta^{13}\text{C}$ values are at least 1.9‰ higher than the $\delta^{13}\text{C}$ values of the group 4 vein calcites, which range from -6.5 to -3.6 (Table 7-1, Figure 7-7).

Modeled infiltrating fluid	T ($^{\circ}\text{C}$) required	$\delta^{13}\text{C}$ (‰)
100 $^{\circ}\text{C}$ - open system	42	0.8
100 $^{\circ}\text{C}$ - closed system	38	1.4
300 $^{\circ}\text{C}$ - open system	137	-0.7
300 $^{\circ}\text{C}$ - closed system	127	-0.3
500 $^{\circ}\text{C}$ - open system	194	-1.7
500 $^{\circ}\text{C}$ - closed system	180	-1.4

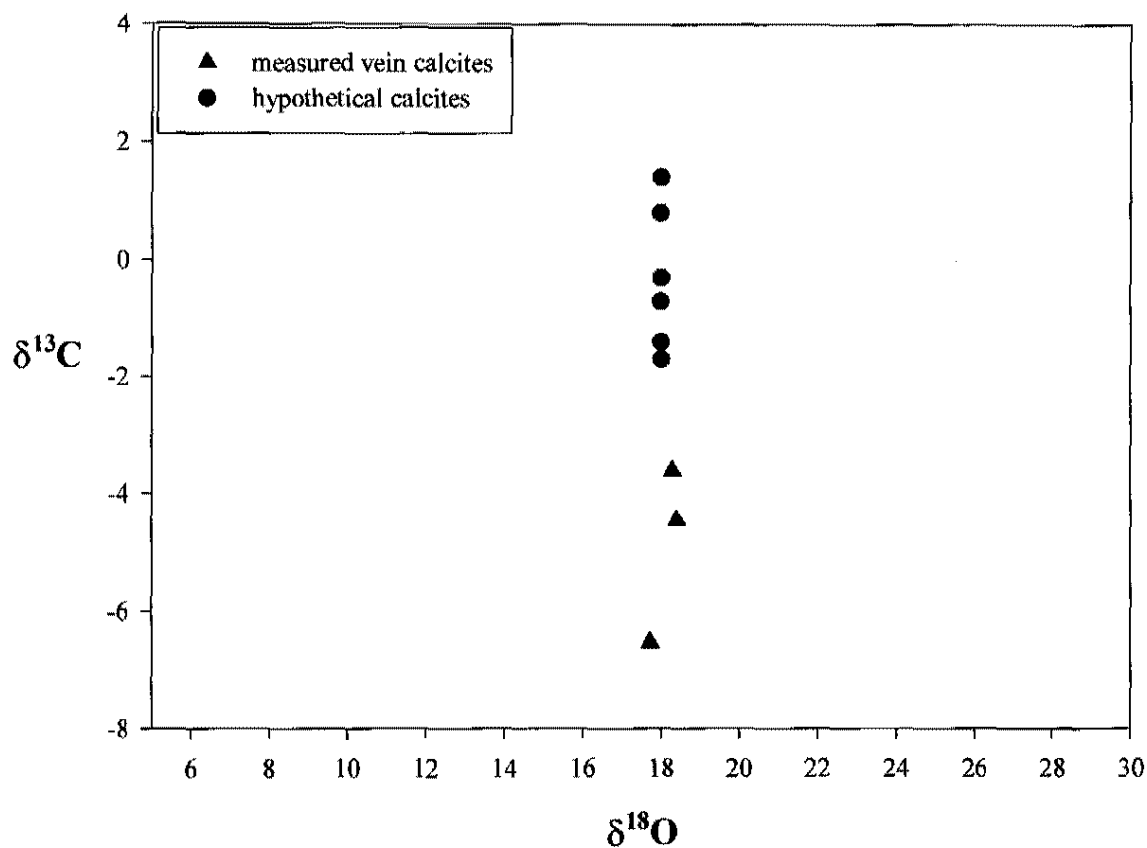


Figure 7-7. Comparison of isotopic signatures of vein calcite samples with the signatures hypothetical vein calcites would have if deposited by the modeled infiltrating fluid at low temperatures. The high $\delta^{13}\text{C}$ values of the hypothetical vein calcites show that the modeled fluid could not have deposited the vein calcites.

Table 7-6. Calculated isotopic signatures of fluid in equilibrium with vein calcite samples at 100°C and 200°C.

Sample	Temperature (°C)	$\delta^{13}\text{C}_\text{fl}$ (‰)	$\delta^{18}\text{O}_\text{fl}$ (‰)
DPUA22	100	-9.9	0.5
DPL30	100	-7.8	1.1
DPL26	100	-7.0	1.1
DPUA22	200	-6.1	8.1
DPL30	200	-4.1	8.7
DPL26	200	-3.2	8.6

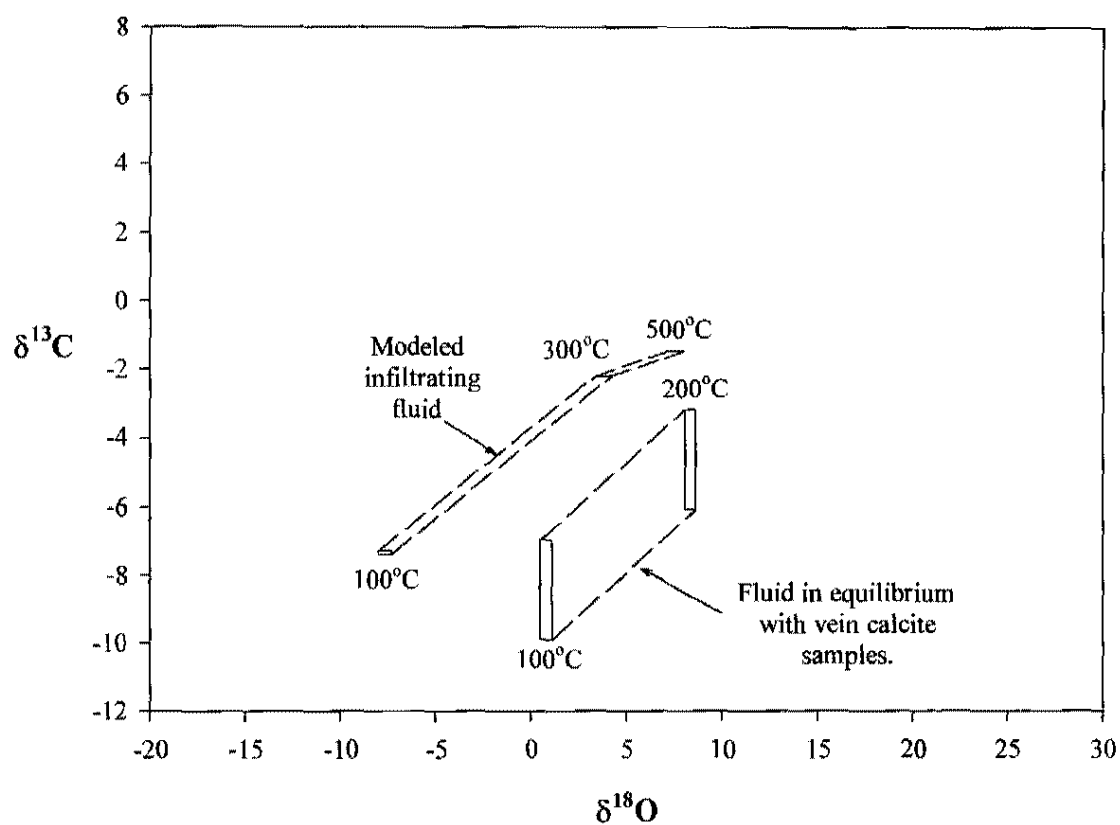


Figure 7-8. Modeled isotopic signature range of infiltrating fluid that depleted the wall rock, and calculated isotopic signature range of fluid that deposited the vein calcites.

Table 7-7. Established ranges of $\delta^{13}\text{C}$ and $\delta^{18}\text{O}$ values for the three possible sources of hydrothermal fluid at Devil Peak.

Fluid Type	Phase	$\delta^{18}\text{O}$ (‰)	$\delta^{13}\text{C}$ (‰)	Reference
magmatic	H ₂ O	5.5 to 10		Taylor (1987)
magmatic	CO ₂		-8.0 to -5.0	Taylor (1986)
magmatic	CO ₂		-5.5 to -3.0	Taylor (1987)
metamorphic	H ₂ O	5.0 to 25		Taylor (1987)
metamorphic	CO ₂		-2.0 to 6.0	Taylor (1987)
meteoric (near Devil Peak)	H ₂ O	-12.8 to -12.1		Hershey (1989)
meteoric (near Devil Peak)	CO ₂		-9.3 to -7.6	Hershey (1989)

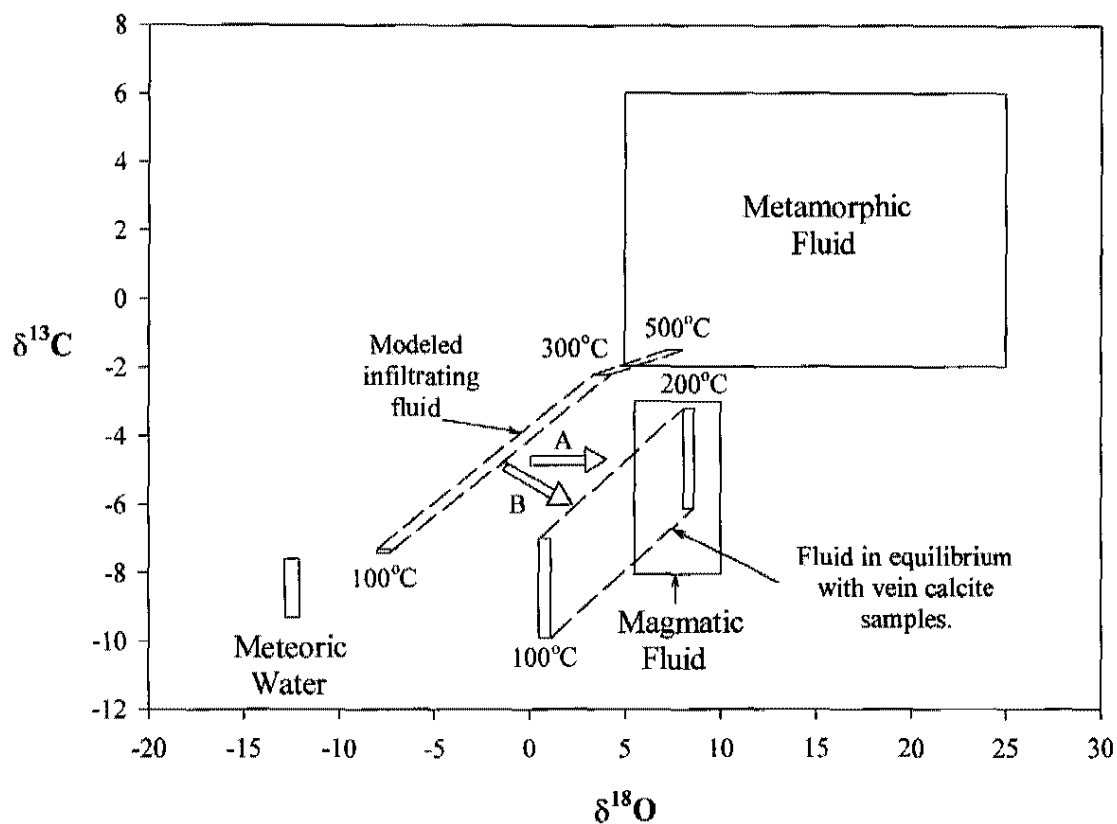


Figure 7-9. Possible sources of the hydrothermal fluid at Devil Peak. The modeled infiltrating fluid could be a mixture of meteoric water and metamorphic fluid. The fluid that deposited the vein calcites could have formed by an influx of carbon-free metamorphic water or by an influx of magmatic fluid. An influx of metamorphic water would increase only the $\delta^{18}\text{O}$ signature of the modeled infiltrating fluid, as shown by arrow A. An influx of magmatic fluid could increase the $\delta^{18}\text{O}$ signature and decrease the $\delta^{13}\text{C}$ signature of the modeled infiltrating fluid, as shown schematically by arrow B.

CHAPTER 8

SUMMARY AND CONCLUSIONS

Hydrothermal Alteration at Devil Peak

Hydrothermal alteration of the Monte Cristo Limestone along the southeast margin of the Devil Peak rhyolite plug is indicated by bleaching of the limestone, depletion of the O and C stable isotope signatures of the limestone, and deposition of minerals in fractures in the bleached limestone. Hydrothermal alteration was initiated by the intrusion of a rhyolite dike that parallels the southeast margin of the Devil Peak plug and/or by intrusion of the Devil Peak plug itself. Dolomitization of the most intensely altered limestones and deposition of Mg-bearing minerals in veins indicate that Mg-metasomatism accompanied hydrothermal alteration.

Presence of Open-Space Brucite at Devil Peak

Petrographic and thermodynamic studies confirm the presence of open-space brucite in veins at Devil Peak. Thin sections show laths of brucite that grew into open space. Thermodynamic diagrams constructed from published thermodynamic data indicate that reactions forming replacement brucite occur at temperatures higher than 180°C, the maximum temperature during and after mineral deposition at Devil Peak, or at unrealistically high X_{CO_2} . Furthermore, the thermodynamic diagrams show that periclase,

the mineral brucite most commonly replaces, could not have been present at Devil Peak because it forms only at temperatures above 180°C or at unreasonably high X_{CO_2} .

Conditions of Alteration at Devil Peak

Temperature

The formation of open-space chalcedony in veins early in the paragenetic sequence limits the temperature of the hydrothermal fluid during and after mineral deposition to less than 180°C. Fluid inclusion homogenization temperatures in a vein calcite sample record minimum trapping temperatures of 150 - 170°C for the majority of the fluid inclusions analyzed.

Hydrothermal Fluid Composition

A trend of decreasing C and O stable isotope signatures in the limestones that corresponds to increasing degree of alteration resulted from infiltration of the limestones by a hydrothermal fluid. Infiltration modeling of the depletion trend using the mass-balance method gives an X_{CO_2} of 0.15 - 0.16 for the hydrothermal fluid during early infiltration of the wall rocks. Temperature- X_{CO_2} diagrams suggest a maximum X_{CO_2} of 0.16 if the hydromagnesite in the veins formed by alteration of the brucite. Freezing point depressions of $\leq 0.6^\circ\text{C}$ in fluid inclusions in vein calcite indicate that $X_{\text{CO}_2} < 0.01$ and that $\text{NaCl} \leq 0.99$ wt. % for the fluid that deposited the calcite.

The paragenetic sequence of early chalcedony followed by serpentine, brucite, and hydromagnesite suggests that during mineral deposition the hydrothermal fluid may have contained more silica early and more Mg^{2+} later. Fluctuations in the temperature,

pressure, X_{CO_2} , and pH of the hydrothermal fluid also could have influenced the order in which these minerals precipitated.

Hydrothermal Fluid Source and Evolution

Mass-balance modeling of the isotopic depletion trend in the wall rocks shows the hydrothermal fluid that initially depleted the wall rocks had a minimum $\delta^{13}\text{C}$ signature of -7.4‰ to -1.5‰ and a maximum $\delta^{18}\text{O}$ signature of -8.0‰ to 8.0‰, indicating that the fluid was a mixture of meteoric water and metamorphic fluid. Vein calcites have higher $\delta^{18}\text{O}$ signatures than the altered limestones containing the veins, and were deposited by a fluid with a higher $\delta^{18}\text{O}$ than the fluid that depleted the limestones. The isotopic signature of the fluid that deposited the vein calcites was calculated to be $\delta^{13}\text{C} = -9.9\text{‰}$ to -3.2‰ and $\delta^{18}\text{O} = 0.5\text{‰}$ to 8.7‰ . This higher $\delta^{18}\text{O}$ fluid may have formed when an influx of high $\delta^{18}\text{O}$ fluid invaded the hydrothermal cell and mixed with the earlier infiltrating fluid, increasing its $\delta^{18}\text{O}$ signature. The high $\delta^{18}\text{O}$ fluid that invaded the system could have been magmatic fluid or metamorphic water. Dilution of the CO_2 in the early infiltrating fluid by the later magmatic fluid or metamorphic water may explain the lower X_{CO_2} indicated by the fluid inclusion study.

Possible Explanation for Rare Brucite Occurrence

Most brucite occurrences consist of replacement brucite that formed from periclase or dolomite in hydrothermal systems with peak alteration temperatures of at least 500°C . At Devil Peak, the hydrothermal fluid temperature during and after mineral deposition remained below 180°C , where brucite can form only by precipitation from solution. The

low temperature of mineral deposition may be a factor in the rare occurrence of open-space brucite at Devil Peak.

APPENDIX I

SAMPLE LIST

All of the samples analyzed for this thesis are cataloged in Table I-I (following pages). An X indicates the study (or studies) in which the sample was used. Locations for samples collected from areas outside the adits are plotted on plate 1. Locations for samples collected in the adits were not plotted due to the high sample density in the adits. Abbreviations: F.I. = fluid inclusion analysis, XRF = X-ray fluorescence spectrometry, XRD = X-ray diffraction analysis, U of W = University of Windsor, Ontario, Mm = Monte Cristo Limestone, Mmp = partly altered Monte Cristo Limestone. Note: of the two western adits, A is the westernmost adit and B is the easternmost adit.

Table I-I. Sample list.

Sample #	Type	Location	Thin Section	F.I.	Stable Isotopes	XRF	XRD UNLV	XRD U of W
DP24	unaltered ls	in Mm, on ridge in NE map area (400 m NE of eastern adit)			X	X		
DPL1	vein	eastern adit						X
DPL4	vein	eastern adit						X
DPL9	vein	eastern adit						X
DPL13	vein	eastern adit	X					
DPL14	vein	eastern adit					X	X
DPL14-1	vein	eastern adit	X					
DPL14-2	vein	eastern adit	X					
DPL14-fib	vein	eastern adit					X	
DPL14-gr	vein	eastern adit					X	
DPL14-wh	vein	eastern adit					X	
DPL14-M1	vein	eastern adit	X					
DPL14-M2	vein	eastern adit	X					
DPL21	vein	eastern adit						X
DPL25	vein	eastern adit					X	

Table I-I, continued.

Sample #	Type	Location	Thin Section	F.I.	Stable Isotopes	XRF	XRD UNLV	XRD U of W
DPL26	calcite vein	eastern adit	X	X	X			
DPL30	vein	eastern adit			X		X	
DPL30a	vein margin ls	eastern adit			X			
DPL31	highly altered ls	eastern adit			X	X		
DPL33	highly altered ls	eastern adit			X	X		
DPL34	unaltered ls	in Mm, 100 m NE of eastern adit			X	X	X	
DPL35	unaltered ls	in Mm, 100 m NE of eastern adit			X	X		
DPU2	unaltered ls	in Mm, on ridge between eastern and western adits			X	X	X	
DPU3	partly altered ls	in Mmp, 100 m SE of western adits			X	X		
DPUA2	vein	western adit A	X					
DPUA9	vein	western adit A						X
DPUA12	vein	western adit A	X					
DPUA17	vein	western adit A	X					
DPUA20	vein	western adit A						X

Table I-I, continued.

Sample #	Type	Location	Thin Section	F.I.	Stable Isotopes	XRF	XRD UNLV	XRD U of W
DPUA22	vein	western adit A			X		X	
DPUA23a	vein	western adit A					X	
DPUA24	highly altered ls	western adit A			X	X		
DPUA25	partly altered ls	western adit A			X	X		
DPUB15	vein	western adit B						X
DPUB22	vein	western adit B						X
DPUC6	unaltered ls	in Mm, on ridge between eastern and western adits			X	X		
DPV1	vein	eastern adit					X	
DPV2	vein	eastern adit					X	
RK-3	vein	eastern adit	X					
RK-4	vein	eastern adit	X					
RK12	vein	eastern adit	X					

APPENDIX II

CONSTRUCTION OF THERMODYNAMIC DIAGRAMS

Reactions 1-6 and 8 on the temperature- X_{CO_2} diagrams were plotted from pressure, temperature, and X_{CO_2} data calculated by THERMOCALC v. 2.4, a FORTRAN program created by Holland and Powell (1990). Reaction 7 was calculated “manually,” using Excel and Mathematica, because hydromagnesite is not in THERMOCALC’s database. The mineral stability diagrams were also calculated manually because THERMOCALC does not calculate the appropriate data for them.

The construction of T- X_{CO_2} diagrams and mineral stability diagrams requires the calculation of the Gibbs free energy of reactions and phases at elevated temperature and pressure. All of the diagrams use the same basic equations for calculating $\Delta G_{(T,P)}$. These equations and their derivation will be discussed first. A description of how the equations are used to construct each type of diagram will follow.

The following symbols will be used in this discussion:

G = Gibbs free energy in kJ/mol	f = fugacity
H = enthalpy in kJ/mol	ν = molar volume
S = entropy in kJ/mol-K	n = number of moles
T = temperature in Celsius or Kelvin as noted	ϕ = fugacity coefficient
V = volume in kJ/kbar-mol	A = Helmholtz energy
P = pressure in kbar	A = molar Helmholtz energy
C _p = heat capacity in kJ/mol-K	X = mole fraction
α = coefficient of thermal expansion in 1/K	
β = coefficient of isothermal compressibility in 1/kbar	

The Equation for Gibbs Free Energy at Elevated Temperature and Pressure

The Gibbs free energy of a phase or reaction at standard state temperature and pressure is given by

$$(1) \quad \Delta G_{(1,298)} = \Delta H_{(1,298)} - T\Delta S_{(1,298)}$$

(where the standard state temperature and pressure are 298.15 °C and 1 bar, respectively),

and by

$$(2) \quad dG = VdP - SdT$$

At temperatures and pressures higher than standard state, the change in Gibbs free energy with changing pressure and temperature must be determined, evaluated at the temperature and pressure of interest, and then added to $\Delta G_{(1,298)}$. Because the effects of temperature

and pressure changes are much greater on fluids than on solids, two different equations are used to “correct” the Gibbs free energy for elevated temperature and pressure:

for solid phases,

$$(3a) \quad \Delta G_{(T,P)} = \Delta H_{(298,1)} - T\Delta S_{(298,1)} + \int_{298}^T \Delta C_p dT - T \int_{298}^T (\Delta C_p/T) dT \\ + \Delta V_{(298,1)} P + \alpha \Delta V_{(298,1)} P(T-298) - 1/2 \beta \Delta V_{(298,1)} P^2$$

for fluid phases,

$$(3b) \quad \Delta G_{(T,P)} = \Delta H_{(298,1)} - T\Delta S_{(298,1)} + \int_{298}^T \Delta C_p dT - T \int_{298}^T (\Delta C_p/T) dT \\ + RT \ln f$$

Equations 3a and 3b are the basic equations used for calculating $\Delta G_{(T,P)}$ for P-T diagrams, T-X_{CO2} diagrams, and mineral stability diagrams.

Derivation of Equations 3a and 3b

The total Gibbs free energy of a phase or reaction at elevated temperature and pressure is

$$(4) \quad \Delta G_{(T,P)} = \Delta G_{(T)} + \Delta G_{(P)}$$

Temperature Dependence of Gibbs Free Energy

Nordstrom and Munoz (1994, p.105) describe the temperature dependence of Gibbs free energy. Given equation 1, the temperature portion of equation 4 becomes

$$(5) \quad \Delta G_{(T)} = \Delta H_{(T)} - T\Delta S_{(T)}$$

The enthalpy at the temperature of interest is given by

$$(6) \quad \Delta H_{(T)} = \Delta H_{(298)} + \int_{298}^T (\partial(\Delta H)/\partial T)_P dT,$$

and the variation in enthalpy with temperature is

$$(7) \quad (\partial(\Delta H)/\partial T)_p = \Delta C_p$$

Substituting equation 7 into equation 6 gives

$$(8) \quad \Delta H_{(T)} = \Delta H_{(298)} + \int_{298}^T \Delta C_p dT$$

The entropy at the temperature of interest is given by

$$(9) \quad \Delta S_{(T)} = \Delta S_{(298)} + \int_{298}^T (\partial(\Delta S)/\partial T)_p dT,$$

and the variation in entropy with temperature is given by

$$(10) \quad (\partial(\Delta S)/\partial T)_p = \Delta C_p/T$$

Substituting equation 10 into equation 9 yields

$$(11) \quad \Delta S_{(T)} = \Delta S_{(298)} + \int_{298}^T (\Delta C_p/T) dT$$

Substituting equations 8 and 11 into equation 5 results in

$$(12) \quad \Delta G_{(T)} = \Delta H_{(298)} + \int_{298}^T \Delta C_p dT - T \Delta S_{(298)} - \int_{298}^T (\Delta C_p/T) dT$$

Pressure Dependence of Gibbs Free Energy

Nordstrom and Munoz (1994, p. 100) describe the pressure dependence of Gibbs free energy. Because the Gibbs free energy of a reaction depends on both temperature and pressure, the differential form of the equation for Gibbs free energy can be written

$$(13) \quad dG = (\partial G/\partial P)_T dP + (\partial G/\partial T)_P dT$$

Comparing this equation with equation 2 shows that

$$(14) \quad (\partial G/\partial P)_T = V$$

Because we are interested in the change in Gibbs free energy, we need to recast equation 14 in terms of ΔG

$$(15) \quad (\partial \Delta G / \partial P)_T = \Delta V$$

The variation in Gibbs free energy with pressure is given by

$$(16) \quad \int_{P_1}^P \Delta G(P) = \Delta G_{(P)} - \Delta G_{(1)} = \int_{P_1}^P \Delta V dP$$

The Pressure Integral

Because the change in volume with change in pressure is so much greater for fluids than for solids, the pressure integral needs to be considered separately for fluids and solids:

for solids

$$(17a) \quad \int_{P_1}^P \Delta V dP = \int_{P_1}^P \Delta V_s dP$$

for fluids

$$(17b) \quad \int_{P_1}^P \Delta V dP = \int_{P_1}^P \Delta V_f dP$$

Solving the Pressure Integral for Solids (Modified from Holland and Powell (1990))

If the combined effects of temperature and pressure on volume are known, the pressure integral for solids can be solved. Powell and Holland (1985) have compiled thermal expansion (α) and isothermal compressibility (β) data for the minerals in their database. They fit the data to the following equations

$$(18) \quad \text{Thermal expansion: } \Delta V_{(1,T)} \approx \Delta V_{(1,298)} + \alpha \Delta V_{(1,298)}(T-298)$$

(19) Isothermal Compressibility: $\Delta V_{(P,298)} \approx \Delta V_{(1,298)} - \beta \Delta V_{(1,298)} P$

The combined effects of thermal expansion and isothermal compressibility for solids are

(20) $\Delta V_{s(T,P)} = \Delta V_{(1,298)} + \alpha \Delta V_{(1,298)} (T-298) - \beta \Delta V_{(1,298)} P,$

and the pressure integral for solids becomes

(21)
$$\int_1^P \Delta V_s dP = \int_1^P \Delta V_{(1,298)} dP + \int_1^P \alpha \Delta V_{(1,298)} (T-298) dP - \int_1^P \beta \Delta V_{(1,298)} dP$$

Evaluate:

(22)
$$\int_1^P \Delta V_s dP = \Delta V_{(1,298)} (P-1) + \alpha \Delta V_{(1,298)} (T-298) (P-1) - 1/2 \beta \Delta V_{(1,298)} (P^2-1)$$

It should be noted that Powell and Holland (1985) integrate from 0 to P, therefore equation 22 becomes

(23)
$$\int_0^P \Delta V_s dP = \Delta V_{(1,298)} P + \alpha \Delta V_{(1,298)} P (T-298) - 1/2 \beta \Delta V_{(1,298)} P^2$$

Robie and Hemingway (1995) and Helgeson et al. (1978) did not compile thermal expansion and isothermal compressibility data. If α and β are not known, equation 23 becomes

(24)
$$\int_0^P \Delta V_s dP = \Delta V P$$

Solving the Pressure Integral for Fluids

For fluids, we are interested in molar volume. Since

(25) $PV = RT$

The pressure integral for fluids becomes

$$(26) \quad \int_{P_1}^P \Delta V_{fl} dP = \int_{P_1}^P (RT/P) dP$$

Evaluate:

$$(27) \quad \int_{P_1}^P \Delta V_{fl} dP = \int_{P_1}^P (RT/P) dP = RT \ln P$$

Because we are dealing with non-ideal gases, P may be replaced by f , the fugacity

$$(28) \quad \int_{P_1}^P \Delta V_{fl} dP = RT \ln f$$

Combining equations 4, 12, and 23 and equations 4, 12, and 28 yields:

for solids

$$(29a) \quad \begin{aligned} \Delta G_{(T,P)} = & \Delta H_{(298)} - T \Delta S_{(298)} + \Delta G_{(1)} + \int_{298}^T \Delta C_p dT \\ & - \int_{298}^T (\Delta C_p/T) dT + \Delta V_{(1,298)} P + \alpha \Delta V_{(1,298)} P(T-298) \\ & - 1/2 \beta \Delta V_{(1,298)} P^2 \end{aligned}$$

for fluids

$$(29b) \quad \begin{aligned} \Delta G_{(T,P)} = & \Delta H_{(298)} - T \Delta S_{(298)} + \Delta G_{(1)} + \int_{298}^T \Delta C_p dT \\ & - \int_{298}^T (\Delta C_p/T) dT + RT \ln f \end{aligned}$$

Because $\Delta G_{(1)} = \Delta H_{(1)} - T \Delta S_{(1)}$, equations 29a and 29b become equations 3a and 3b:

for solids

$$(3a) \quad \begin{aligned} \Delta G_{(T,P)} = & \Delta H_{(298,1)} - T \Delta S_{(298,1)} + \int_{298}^T \Delta C_p dT - T \int_{298}^T (\Delta C_p/T) dT \\ & + \Delta V_{(298,1)} P + \alpha \Delta V_{(298,1)} P(T-298) - 1/2 \beta \Delta V_{(298,1)} P^2 \end{aligned}$$

for fluids

$$(3b) \quad \begin{aligned} \Delta G_{(T,P)} = & \Delta H_{(298,1)} - T \Delta S_{(298,1)} + \int_{298}^T \Delta C_p dT - T \int_{298}^T (\Delta C_p/T) dT \\ & + RT \ln f \end{aligned}$$

Heat Capacity

The equation used for ΔC_p depends on the thermodynamic data set being used.

For the P-T and T- X_{CO_2} diagrams, all thermodynamic data is from the Holland and Powell (1990) data set (extracted from THERMOCALC v. 2.4) except for hydromagnesite, which is from Helgeson et al. (1978). For the mineral stability diagrams, all data is from Robie and Hemingway (1995) except for hydromagnesite, which is from Helgeson et al. (1978).

For Holland and Powell (1990)

$$(30a) \quad \Delta C_p = a + bT + cT^{-2} + dT^{-0.5}$$

$$(31a) \quad \int_{298}^T \Delta C_p dT = \int_{298}^T (a + bT + cT^{-2} + dT^{-0.5}) dT = aT + 1/2bT^2 - cT^{-1} + 2dT^{0.5} \Big|_{298}^T$$

$$(32a) \quad \int_{298}^T \Delta C_p / T dT = \int_{298}^T (aT^{-1} + b + cT^{-3} + dT^{-1.5}) dT = a \ln T + bT - 1/2cT^{-2} - 2dT^{-0.5} \Big|_{298}^T$$

For Helgeson et al. (1978)

$$(30b) \quad \Delta C_p = a + bT - cT^{-2}$$

$$(31b) \quad \int_{298}^T \Delta C_p dT = \int_{298}^T (a + bT - cT^{-2}) dT = aT + 1/2bT^2 + cT^{-1} \Big|_{298}^T$$

$$(32b) \quad \int_{298}^T \Delta C_p / T dT = \int_{298}^T (aT^{-1} + b - cT^{-3}) dT = a \ln T + bT + 1/2cT^{-2} \Big|_{298}^T$$

For Robie and Hemingway (1995)

$$(30c) \quad \Delta C_p = a + bT + cT^{-2} + dT^{-0.5} + eT^2$$

$$(31c) \quad \int_{298}^T \Delta C_p dT = \int_{298}^T (a + bT + cT^{-2} + dT^{-0.5} + eT^2) dT = aT + 1/2bT^2 - cT^{-1} + 2dT^{0.5} + 1/3eT^3 \Big|_{298}^T$$

$$(32c) \quad \int_{298}^T \Delta C_p/T dT = \int_{298}^T (aT^{-1} + b + cT^{-3} + dT^{-1.5} + eT) dT = a \ln T + bT - 1/2cT^{-2} - 2dT^{-0.5} + 1/2eT^2 \Big|_{298}^T$$

Fugacity

While experimental fugacity data is plentiful, rarely has it been measured at all of the temperatures, pressures, and CO₂ contents of interest. Usually, the fugacities required for creating T-X_{CO₂} diagrams and mineral stability diagrams are calculated from an equation of state that is calibrated for the temperature and pressure range of interest.

The CORK Equation of State

The CORK (Compensated Redlich-Kwong) equation of state of Holland and Powell (1991) is the most recent and most accurate equation of state for the pressure and temperature region of interest of this study. Fortunately, this equation is the one used by THERMOCALC v. 2.4 (pers. comm., T.J.B. Holland, 1997). The CORK equation of state was also used for calculating the fugacities in reaction 7.

The CORK equation of state is

$$(33) \quad P = RT/(V - b) - a/T^{0.5}V(V + b)$$

where a and b are parameters that will be defined below. The equation used to calculate the fugacity coefficient from an equation of state is specific to that equation of state. For the CORK, the equation is the same one given by Redlich and Kwong (1949) in their original paper

$$(34) \quad \ln \phi = - \ln(Z - BP) - A^2/B[\ln(1 + BP/Z)] + Z - 1$$

where $\phi = f/P$, $A^2 = a/R^2T^{2.5}$, and $B = b/RT$

Derivation of the Equation for Calculating the Fugacity Coefficient

Most geochemical thermodynamic textbooks (Kyle, 1992, p. 203; Fletcher, 1993, p. 133; Nordstrom and Munoz, 1994, p. 132) derive the equation for calculating the fugacity coefficient with respect to pressure

$$(35) \quad \ln\phi = 1/RT \int_{P_0}^P (V - RT/P) dP = \int_{P_0}^P (Z - 1)/P dP,$$

but this form is only valid for volume-explicit equations of state. Most practical equations of state are pressure-explicit (Tester and Modell, 1997, p. 348). For pressure-explicit equations of state, the expression for $\ln\phi$ must be integrated with respect to volume. This can be done by deriving the expression for the fugacity coefficient with respect to Helmholtz energy. For simplicity in explanation, the case of a pure fluid phase will be considered (c.f. Tester and Modell, 1997, pp. 256, 274-277, and 351).

The fugacity coefficient can be calculated from the Helmholtz free energy by the equation

$$(36) \quad RT \ln\phi = (A - A^\circ) + n[\partial(A - A^\circ)/\partial n_{(T,V)}]$$

where $A - A^\circ$ is the Helmholtz energy departure function for the equation of state. The Helmholtz energy departure function is given by

$$(37) \quad (A - A^\circ)_{(T,V)} = \int_{\infty}^V (P - RT/V) dV + RT \ln(V^\circ/V)$$

Substituting the CORK equation of state (equation 33) for P results in

$$(38) \quad (A - A^\circ)_{(T,V)} = \int_{\infty}^V [RT/(V - b) - a/T^{0.5}V(V + b) - RT/V] dV + RT \ln(V^\circ/V)$$

Integrate:

$$(39) \quad (A - A^\circ)_{(T,V)} = RT \ln(V - b) \Big|_V^\infty - a/T^{0.5}b(\ln V - \ln(V + b)) \Big|_V^\infty \\ - RT \ln V \Big|_V^\infty + RT \ln(V^\circ/V)$$

Evaluate:

$$(40) \quad (A - A^\circ)_{(T,V)} = RT \ln(\infty - b) - RT \ln(V - b) - a/(T^{0.5}b) \ln \infty + \\ a/(T^{0.5}b) \ln V + a/(T^{0.5}b) \ln(\infty + b) - a/(T^{0.5}b) \ln(V + b) \\ - RT \ln \infty + RT \ln V + RT \ln V^\circ - RT \ln V$$

Rearranging equation 40 gives

$$(41) \quad (A - A^\circ)_{(T,V)} = RT \ln[V^\circ/(V - b)] + (a/T^{0.5}b) \ln[V/(V + b)] \\ + RT \ln[(\infty - b)/\infty] + (a/T^{0.5}b) \ln[(\infty + b)/\infty]$$

Because $(\infty + b)/\infty \cong 1$ and $(\infty - b)/\infty \cong 1$, $RT \ln[(\infty - b)/\infty] = 0$ and

$(a/T^{0.5}b) \ln[(\infty + b)/\infty] = 0$; therefore, equation 41 can be simplified to

$$(42) \quad (A - A^\circ)_{(T,V)} = RT \ln[V^\circ/(V - b)] + (a/T^{0.5}b) \ln[V/(V + b)],$$

which is the Helmholtz energy departure function for the CORK equation of state. To calculate the fugacity coefficient, equation 42 needs to be converted to molar quantities.

Given that $\nu = nV$ and $\nu^\circ = nV^\circ$:

$$(43) \quad (A - A^\circ)_{(T,\nu,n)} = RT \ln[V^\circ/(V - b) * n/n] + (a/T^{0.5}b) \ln[V/(V + b) * n/n],$$

and

$$(44) \quad (A - A^\circ)_{(T,\nu,n)} = RT \ln[\nu^\circ/(\nu - bn)] + (a/T^{0.5}b) \ln[\nu/(\nu + bn)]$$

Partial differentiation with respect to n gives

$$(45) \quad (A - A^\circ)_{(T,\nu,n)} = bRT/(\nu - bn) - a/T^{0.5}(\nu + bn)$$

Substituting equations 42 and 45 into equation 36 yields

$$(46) \quad RT \ln \phi = RT \ln[V^\circ/(V - b)] + (a/T^{0.5}b) \ln[V/(V + b)] \\ + n(bRT/(\nu - bn) - a/T^{0.5}(\nu + bn))$$

Dividing by RT and multiplying by n results in

$$(47) \quad \ln \phi = \ln[V^\circ/(V - b)] + (a/RT^{1.5}b) \ln[V/(V + b)] + b/(V - b) - a/RT^{1.5}(V + b)$$

The last two terms become $Z - 1$ because $P = RT/(V - b) - a/T^{0.5}V(V + b)$ (the CORK equation) and $Z = PV/RT$ (for $n = 1$), which leaves

$$(48) \quad \ln \phi = \ln[V^\circ/(V - b)] + (a/RT^{1.5}b) \ln[V/(V + b)] + Z - 1$$

Substituting $Z = PV/RT$ (for $n = 1$), $V^\circ = RT/P$, $A^2 = a/R^2T^{2.5}$, and $B = b/RT$ into equation 48 and rearranging gives equation 34

$$(34) \quad \ln \phi = -\ln(Z - BP) = A^2/B[\ln(1 + BP/Z)] + Z - 1$$

The fugacity coefficient of a component in a mixture can be similarly calculated, yielding the equation

$$(49) \quad \ln \phi_i = (Z - 1)B_i/B_m - \ln(Z - B_m P) - A_m^2/B_m[2A_i/A - B_i/B_m] \ln(1 + B_m P/Z)$$

Substituting $A^2 = a/R^2T^{2.5}$, and $B = b/RT$, equation 49 becomes

$$(50) \quad \ln \phi_i = (Z - 1)b_i/b_m - \ln(Z - b_m P/RT) - [a_m/(RT^{1.5}b_m)][2(a/a_m)^{0.5} - b/b] \ln(1 + (b_m P/RT)/Z)$$

where, for the CORK equation of state (as given by Holland and Powell (1991)):

$$a_i = a_{\text{H}_2\text{O}} \text{ or } a_{\text{gas}} \text{ or } a_{\text{CO}_2}$$

$$b_i = b_{\text{H}_2\text{O}} \text{ or } b_{\text{CO}_2}$$

$$a_{\text{H}_2\text{O}} \text{ (for } T < 673\text{K)} = 1113.4 - 0.88517(673-T) + 4.53 \times 10^{-3}(673-T)^2 - 1.3183 \times 10^{-5}(673-T)^3$$

$$a_{\text{H}_2\text{O}} \text{ (for } T < 673\text{K)} = 1113.4 - 0.22291(T-673) - 3.8022 \times 10^{-4}(T-673)^2 + 1.7791 \times 10^{-7}(T-673)^3$$

$$a_{\text{gasH}_2\text{O}} \text{ (for } T < 673\text{K)} = 1113.4 + 5.8487(673-T) - 2.137 \times 10^{-2}(673-T)^2 + 6.8133 \times 10^{-5}(673-T)^3$$

$$a_{CO_2} = 741.2 - 0.10891 \times 10^{-6}T - 3.4203 \times 10^{-4}T^2 \text{ for } 373 < T < 1873K$$

$$a_m = a_{mix} \text{ or } a_{gasmix}$$

$$a_{mix} = a_{H_2O}X_{H_2O}^2 + a_{CO_2}X_{CO_2}^2 + 2X_{H_2O}X_{CO_2}(a_{H_2O}a_{CO_2})^{0.5}$$

$$a_{gasmix} = a_{gasH_2O}X_{H_2O}^2 + a_{CO_2}X_{CO_2}^2 + 2X_{H_2O}X_{CO_2}(a_{gasH_2O}a_{CO_2})^{0.5}$$

$$b_{H_2O} = 1.465$$

$$b_{CO_2} = 3.057$$

$$b_m = b_{H_2O}X_{H_2O} + b_{CO_2}X_{CO_2}$$

$$P = P_1 \text{ or } P_{sat}$$

$$P_1 = \text{pressure of interest}$$

$$P_{sat} = \text{saturation pressure} = -13.627 \times 10^{-3} + 7.29395 \times 10^{-7}T^2 - 2.34622 \times 10^{-9}T^3 \\ + 4.83607 \times 10^{-15}T^5 \text{ for } T < 695$$

and T is in Kelvin

(Note: The mixing rules (a_{mix} , a_{gasmix} , and b_{mix}) are from Kerrick and Jacobs, 1981.)

Calculating Fugacities

Equation 50 is used to calculate the fugacity coefficients for the fluid phase in reaction 7 and in the mineral stability diagrams. The calculation of the fugacity coefficients is not straightforward, as explained in the appendix of Holland and Powell (1991):

1. For $T > 695K$, the fugacity coefficients for H_2O and CO_2 are calculated separately from equation 50. For H_2O , a_{H_2O} and a_{mix} are used.
2. At temperatures below 695K, P_{sat} should be calculated.

3. For $T < 695\text{K}$ and $P < P_{\text{sat}}$, the fugacity coefficients for H_2O and CO_2 are calculated separately from equation 50. For H_2O , $a_{\text{gasH}_2\text{O}}$ and a_{gasmix} are used if $T < 673\text{K}$, and $a_{\text{H}_2\text{O}}$ and a_{mix} are used if $T > 673\text{K}$.
4. For $T < 695\text{K}$ and $P > P_{\text{sat}}$, the fugacity coefficients for H_2O and CO_2 are calculated separately from the equation

$$(51) \quad \ln\phi_i = \ln\phi_1 - \ln\phi_2 + \ln\phi_3$$

where

-- $\ln\phi_1$ for H_2O or CO_2 is calculated from equation 50 using $a_{\text{gasH}_2\text{O}}$,

a_{gasmix} , and P_{sat} . P_{sat} should also be used to calculate Z.

-- $\ln\phi_2$ for H_2O or CO_2 is calculated from equation 50 using $a_{\text{H}_2\text{O}}$,

a_{mix} , and P_{sat} . P_{sat} should also be used to calculate Z.

-- $\ln\phi_3$ for H_2O or CO_2 is calculated from equation 50 using $a_{\text{H}_2\text{O}}$,

a_{mix} , and P_i . P_i should also be used to calculate Z.

Once the fugacity coefficient has been determined, the fugacity can be calculated by

$$(52) \quad f_i = e^{\ln\phi_i} X_i P$$

Temperature - X_{CO_2} Diagrams

Reactions plot as lines on temperature- X_{CO_2} diagrams. The line represents the T - X_{CO_2} conditions across which one mineral assemblage converts to another. At the T - X_{CO_2} conditions along the line, all minerals involved in the reaction are stable. The products and reactants are in equilibrium; thus the Gibbs free energy of the reaction is equal to zero.

The condition that $\Delta G_{r(T,P)} = 0$ is the basis for calculating reaction 7 on the T- X_{CO_2} diagrams in this study. In Excel, the Gibbs free energies of brucite and hydromagnesite were calculated at the temperature and pressure of interest, using the thermodynamic data of Holland and Powell (1990) (extracted from THERMOCALC) for brucite, and of Helgeson et al. (1978) for hydromagnesite. The heat capacity, enthalpy, and entropy were calculated for CO_2 at the temperature and pressure of interest using thermodynamic data extracted from THERMOCALC. All of the parameters required for calculating the fugacity coefficient of CO_2 using equation 50 (e.g. a_{H_2O} , a_{mix} , etc.) were also calculated in Excel at the temperature and pressure of interest. The CORK equation of state of Holland and Powell (1991) was rearranged to solve for volume

$$(53) \quad PV^3 - RTV^2 - V(bRT + b^2P - a/T^{0.5}) - ab/T^{0.5} = 0$$

Because this is a cubic equation in volume, the equation was solved in Mathematica. The fugacity was then calculated in Excel from equation 50 using the volume calculated from equation 53, and the Gibbs free energy for CO_2 was calculated from equation 3.

Once the Gibbs free energies of all of the reactants and products were calculated, the Gibbs free energy of the reaction was determined by

$$(54) \quad \Delta G_{r(T,P)} = \Delta G_{(T,P)products} - \Delta G_{(T,P)reactants}$$

Solving equations 54 (and the equations leading up to it) for the condition $\Delta G_{r(T,P)} = 0$ was an iterative process. For the T- X_{CO_2} diagrams, P was held constant for the entire series of calculations, an X_{CO_2} was chosen, a T was guessed, and $\Delta G_{r(T,P)}$ was calculated as described above. If $\Delta G_{r(T,P)} \neq 0$, another T was guessed and the process repeated until $\Delta G_{r(T,P)} = 0$.

Mineral Stability Diagrams

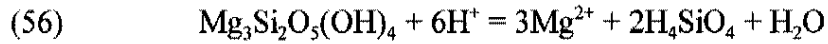
Mineral dissolution reactions plot as lines on mineral stability diagrams. The axes on the diagrams are chosen to be the log of the activities of certain system components that will allow all of the minerals of interest to be plotted on a single diagram. Diagrams constructed at a single temperature show the chemical conditions under which the minerals will precipitate from or dissolve into solution, while diagrams constructed at multiple temperatures, e.g. Figure 6-3, show the entire temperature range (as well as the chemical conditions) over which the minerals will precipitate from solution. Diagrams showing multiple temperatures are simply many single-temperature diagrams combined.

For these mineral stability diagrams used in this study, $\log a\text{Mg}^{2+}/(a\text{H}^+)^2$ and $\log a\text{H}_4\text{SiO}_4$ were chosen as axes. The diagrams were constructed by writing dissolution reactions for each possible phase in the system. The $\Delta G_{r(T,P)}$ was calculated in Excel and Mathematica for each reaction at the T, P, and X_{CO_2} of interest as described in the previous section. The difference here is that for the mineral stability diagrams, $\Delta G_{r(T,P)}$ need not equal 0, and the diagrams are calculated at constant T, P, and X_{CO_2} ; thus no iteration is necessary, and $\Delta G_{r(T,P)}$ for each reaction is calculated only once at each T, P, and X_{CO_2} of interest. The log of the equilibrium constant for each reaction was then calculated from $\Delta G_{r(T,P)}$ using the equation

$$(55) \quad \log K = - \Delta G_{r(T,P)} / (2.303RT)$$

An equation for log K was also written in terms of concentrations of the reactants and products. The two equations for log K were set equal to each other and simplified, and the resulting equation was rearranged in a form that can be plotted on an x,y graph with

$x = \log a\text{H}_4\text{SiO}_4$ and $y = \log a\text{Mg}^{2+}/(a\text{H}^+)^2$. For example, for serpentine, the dissolution reaction is



For serpentine at 150°C, 100 bars, and $X_{\text{CO}_2} = 0.01$, $\Delta G_{\text{T,P}} = 157017.5 \text{ J/mol-K}$.

$$\log K = (157017.5 \text{ J/mol-K}) / (2.303 * 8.31451 \text{ J/K-mol} * 423 \text{ K}) = 19.4.$$

According to the Law of Mass Action,

$$(57) \quad \log K = \log [(a\text{Mg}^{2+})^3(a\text{H}_4\text{SiO}_4)^2(a\text{H}_2\text{O})] / [(a\text{Mg}_3\text{Si}_2\text{O}_5(\text{OH})_4)(a\text{H}^+)^6]$$

but serpentine and water are pure substances, so $a\text{Mg}_3\text{Si}_2\text{O}_5(\text{OH})_4 = 1$ and $a\text{H}_2\text{O} = 1$, and

$\log a\text{Mg}_3\text{Si}_2\text{O}_5(\text{OH})_4$ and $\log a\text{H}_2\text{O} = 0$. Thus

$$(58) \quad \log K = \log (a\text{Mg}^{2+})^3(a\text{H}_4\text{SiO}_4)^2 / (a\text{H}^+)^6 = 19.4$$

Rearranging,

$$(59) \quad 3 \log (a\text{Mg}^{2+}) / (a\text{H}^+)^2 = 2 \log a\text{H}_4\text{SiO}_4 + 19.4$$

and

$$(60) \quad \log (a\text{Mg}^{2+}) / (a\text{H}^+)^2 = 0.67 \log a\text{H}_4\text{SiO}_4 + 6.5$$

Equation 60 plots on Figure 6-4 with a slope of 0.67 and a y-intercept of 6.5.

APPENDIX III

STABLE ISOTOPE MODELING

Relationship Between F_{carbon} and F_{oxygen} in Silicate-

Absent Rayleigh Decarbonation

Silicate-absent Rayleigh decarbonation occurs by the reaction



For this reaction,

$$(1) \quad F_{\text{carbon}} = (C_i - C_d)/C_i, \text{ and}$$

$$(2) \quad F_{\text{oxygen}} = (3C_i - 2C_d)/3C_i$$

as decarbonation occurs, where F_{carbon} = the fraction of carbon remaining in the wall rock, F_{oxygen} = the fraction of oxygen remaining in the wall rock, C_i = the initial number of carbon atoms in the wall rock before decarbonation began, and C_d = the number of carbon atoms lost to decarbonation. Rearranging equation 2 to solve for C_d gives

$$(3) \quad C_d = 1.5 * C_i * (1 - F_{\text{oxygen}}).$$

Substituting equation 3 into equation 1 yields

$$(4) \quad F_{\text{carbon}} = (C_i - 1.5 * C_i * (1 - F_{\text{oxygen}}))/C_i.$$

Simplifying this equation results in

$$(5) \quad F_{\text{carbon}} = 1.5 * F_{\text{oxygen}} - 0.5.$$

The Mass-Balance Equation and

Fluid-to-Rock Ratios

The mass-balance equation and the equation for calculating fluid-to-rock ratios in a closed system are given by Taylor (1974). The mass-balance equation is

$$(6) \quad F\delta_{\text{fl}}^i + R\delta_r^i = F\delta_{\text{fl}}^f + R\delta_r^f,$$

where F = the atom percent of fluid oxygen or carbon in the total system, R = the atom percent of exchangeable rock oxygen or carbon in the bulk system, δ_{fl}^i and δ_r^i = initial δ value in the fluid and rock, respectively, and δ_{fl}^f and δ_r^f = final δ value in the fluid and rock, respectively, after exchange. Derivation of the equation for fluid-to-rock ratios from the mass-balance equation is straightforward. Rearranging equation 6 gives

$$(7) \quad F/R_{\text{closed}} = (\delta_r^f - \delta_r^i)/(\delta_{\text{fl}}^i - \delta_{\text{fl}}^f)$$

Substituting $\Delta = \delta_r^f - \delta_{\text{fl}}^f$ gives the equation for fluid-to-rock ratios

$$(8) \quad F/R_{\text{closed}} = (\delta_r^f - \delta_r^i)/(\delta_{\text{fl}}^i - \delta_r^f + \Delta)$$

Derivation of the Open System Equation for Fluid-to-Rock

Ratios (Modified from Gregory et al., 1989)

For the mass-balance method, a system is considered open when very tiny portions of fluid infiltrate the wall rock, equilibrate completely, then leave the system. This behavior can be described by the differential equation

$$(9) \quad R(d\delta_r) = -(\delta_r - \delta_{\text{fl}}^i)dF$$

Substituting $\Delta = \delta_r - \delta_{\text{fl}}^i$ yields

$$(10) \quad R(d\delta_r) = -(\delta_r - \Delta - \delta_{\text{fl}}^i)dF$$

Rearrange,

$$(11) \quad dF/R = - d\delta_r / (\delta_r - \Delta - \delta_{\text{fl}}^i)$$

integrate both sides,

$$(12) \quad \int_0^F dF/R = - \int_{\delta_{\text{fl}}^i}^{\delta_{\text{fr}}^i} d\delta_r / (\delta_r - \Delta - \delta_{\text{fl}}^i)$$

and evaluate:

$$(13) \quad F/R|_0^F = - \ln(\delta_r - \Delta - \delta_{\text{fl}}^i) \Big|_{\delta_{\text{fl}}^i}^{\delta_{\text{fr}}^i}$$

$$(14) \quad F/R_{\text{open}} = \ln[(\delta_r^i - \Delta - \delta_{\text{fl}}^i) / (\delta_r^f - \Delta - \delta_{\text{fl}}^i)]$$

Equation 14 is equal to $\ln(F/R_{\text{closed}} + 1)$. Proving this requires some rearranging and substitution. Multiplying inside the parentheses in equation 14 by $(-1/-1)$ gives

$$(15) \quad F/R_{\text{open}} = \ln[(\delta_{\text{fl}}^i - \delta_r^i + \Delta) / (\delta_{\text{fl}}^i - \delta_r^f + \Delta)]$$

Separating the fraction into two terms and adding δ_r^f to one term while subtracting it from the other results in

$$(16) \quad F/R_{\text{open}} = \ln[(\delta_r^f - \delta_r^i) / (\delta_{\text{fl}}^i - \delta_r^f + \Delta)] + (\delta_{\text{fl}}^i - \delta_r^f + \Delta) / (\delta_{\text{fl}}^i - \delta_r^f + \Delta)$$

Substituting equation 8 into equation 16 and simplifying yields

$$(17) \quad F/R_{\text{open}} = \ln(F/R_{\text{closed}} + 1)$$

Infiltration Modeling

Calculating the Depleted Signatures

Rearranging equations 8 and 14 (or 17) will give the equations required for calculating the depleted wall rock signatures:

for $\delta^{18}\text{O}$, closed system

$$(18) \quad \delta^{18}\text{O}_r^f = (F/R_o)(\delta^{18}\text{O}_{\text{fl}}^i + \Delta_{\text{cal-H}_2\text{O}}) + \delta^{18}\text{O}_r^i / (F/R_o + 1)$$

for $\delta^{18}\text{O}$, open system

$$(19) \quad \delta^{18}\text{O}_r^f = ((\delta^{18}\text{O}_r^i - \delta^{18}\text{O}_{\text{fl}}^i - \Delta_{\text{cal-H}_2\text{O}})/e^{F/R_o}) + \delta^{18}\text{O}_{\text{fl}}^i + \Delta_{\text{cal-H}_2\text{O}}$$

where $\Delta_{\text{cal-H}_2\text{O}} = 2.78 \times 10^6 T^{-2} - 2.89$ (O'Neil et al., 1969), and F/R_o is the fluid-to-rock ratio for $\delta^{18}\text{O}$, and

for $\delta^{13}\text{C}$, closed system

$$(20) \quad \delta^{13}\text{C}_r^f = (F/R_c(\delta^{13}\text{C}_{\text{fl}}^i - \Delta_{\text{CO}_2\text{-cal}}) + \delta^{13}\text{C}_r^i)/(F/R_c + 1)$$

for $\delta^{13}\text{C}$, open system

$$(21) \quad \delta^{13}\text{C}_r^f = ((\delta^{13}\text{C}_r^i - \delta^{13}\text{C}_{\text{fl}}^i - \Delta_{\text{CO}_2\text{-cal}})/e^{F/R_c}) + \delta^{13}\text{C}_{\text{fl}}^i - \Delta_{\text{CO}_2\text{-cal}}$$

where $\Delta_{\text{CO}_2\text{-cal}} = -2.988 \times 10^6 T^{-2} = 7.6663 \times 10^3 T^{-1} - 2.4612$ (Bottinga, 1968), and F/R_c is the fluid-to-rock ratio for $\delta^{13}\text{C}$.

(Note: Bottinga's data is presented as $\Delta_{\text{CO}_2\text{-cal}}$; $\Delta_{\text{CO}_2\text{-cal}} = -\Delta_{\text{cal-CO}_2}$.)

Fluid-to-rock ratios for $\delta^{18}\text{O}$ and $\delta^{13}\text{C}$

The link between the equations for $\delta^{18}\text{O}_r^f$ and $\delta^{13}\text{C}_r^f$ is, of course, the fluid-to-rock ratios. It is important to note that $F/R_o \neq F/R_c$ for several different reasons. First, CO_2 has two atoms of oxygen to exchange per unit volume of CaCO_3 , while H_2O has only one atom of oxygen to exchange per unit volume of CaCO_3 . Second, the oxygen in H_2O exchanges with three atoms of oxygen per unit volume of CaCO_3 , while the carbon in CO_2 exchanges with only one carbon atom per unit volume of CaCO_3 . Finally, the carbon in CaCO_3 exchanges only with CO_2 , which comprises a small percentage of the fluid, while the oxygen in CaCO_3 exchanges with both H_2O and CO_2 . The fluid-to-rock ratio for $\delta^{18}\text{O}$ can be converted to the fluid-to-rock ratio for $\delta^{13}\text{C}$ by the equation

$$(22) \quad F/R_c = F/R_o * (1 + X_{CO_2}) * 3 * X_{CO_2}$$

where the $(1 + X_{CO_2})$ term accounts for the “extra” oxygen atom in CO_2 (e.g., for an X_{CO_2} of 0.1, 90% of the fluid flowing through the rock contains one oxygen atom per molecule, while 10% of the fluid contains two oxygen atoms per molecule; thus the rock interacts with an “additional” 10% oxygen atoms); the 3 compensates for the 3:1 ratio of oxygen to carbon atoms in $CaCO_3$; and the X_{CO_2} accounts for the fraction of the fluid that actually interacts with the carbon in $CaCO_3$.

The Modeling Method

The isotopic signatures of the unaltered, partly altered, and highly altered wall rock samples were plotted on a $\delta^{18}O$ - $\delta^{13}C$ diagram in Excel. The average isotopic signature of the unaltered limestones was used as the starting composition for the modeled wall rocks. The object of the modeling was to produce a curve that began at the unaltered limestone samples and passed through the partly altered limestone samples and the highly altered limestone samples. The equations were set up in Excel, the $\delta^{13}C$, $\delta^{18}O$, and X_{CO_2} values of a hypothetical infiltrating fluid were guessed, an F/R_o was chosen, and the $\delta^{13}C$ and $\delta^{18}O$ signature of the modeled wall rock was calculated. The modeled wall rock signatures were calculated at values of F/R_o that increased by 0.5 to simulate the progression of infiltration. The calculated $\delta^{18}O$ and $\delta^{13}C$ signatures were plotted on the $\delta^{18}O$ - $\delta^{13}C$ diagram and compared with the actual $\delta^{18}O$ and $\delta^{13}C$ signatures of the depleted wall rock samples. The $\delta^{13}C$, $\delta^{18}O$, and X_{CO_2} of the hypothetical infiltrating fluid was adjusted until the modeled depleted signatures matched the actual depleted signatures.

Calculating the Isotopic Signatures of

Hypothetical Vein Calcites

The isotopic signatures of hypothetical vein calcites deposited by the modeled fluids were calculated using the equation

$$(23) \quad \delta_{\text{cal}} = [(\delta_{\text{fl}} + 1000)/\alpha_{\text{fl-cal}}] - 1000$$

where $\alpha_{\text{fl-cal}}$ is the fractionation factor between the fluid and calcite for ^{13}C or ^{18}O . The fractionation factor was calculated from $\Delta_{\text{H}_2\text{O-cal}}$ and $\Delta_{\text{cal-CO}_2}$ using the equation

$$(24) \quad \alpha = e^{\Delta/1000}$$

Equation 23 is simply the defining equation for the fractionation factor rearranged. The fractionation factor is defined as

$$(25) \quad \alpha_{\text{a-b}} = (\delta_{\text{a}} + 1000)/(\delta_{\text{b}} + 1000)$$

The $\Delta_{\text{H}_2\text{O-cal}}$ and $\Delta_{\text{CO}_2\text{-cal}}$ data are from O'Niel et al., 1969, and Bottinga, 1968, respectively. (Bottinga's data is presented as $\Delta_{\text{CO}_2\text{-cal}}$, and $\Delta_{\text{CO}_2\text{-cal}} = -\Delta_{\text{cal-CO}_2}$.)

REFERENCES CITED

- Armstrong, R.L., 1970, Geochronology of Tertiary igneous rocks, eastern Basin and Range province, western Utah, eastern Nevada, and vicinity, U.S.A.: *Geochimica et Cosmochimica Acta*, v. 34, p. 203-232.
- Baumgartner, L.P., and Rumble, D., III., 1988, Transport of stable isotopes: I: Development of a kinetic continuum theory for stable isotope transport: *Contributions to Mineralogy and Petrology*, v. 98: p. 417-430.
- Blattner, P., and Lassey, K.R., 1990, Transport of stable isotopes, kinetics, dispersive advection, and the 'isotopic fronts' of Baumgartner and Rumble (1988): *Contributions to Mineralogy and Petrology*, v. 105, p. 486-490.
- Bottinga, Y., 1968, Calculation of fractionation factors for carbon and oxygen exchange in the system calcite-carbon dioxide-water: *Journal of Physical Chemistry*, v. 72, p. 800-808.
- Brown, P.E., Bowman, J.R., Kelly, W.C., 1985, Petrologic and stable isotope constraints on the source and evolution of skarn-forming fluids at Pine Creek, California: *Economic Geology*, v. 80, p. 72-95.
- Bucher-Nurminen, K., 1982, On the mechanism of contact aureole formation in dolomitic country rock by the Adamello intrusion (northern Italy): *American Mineralogist*, v. 67, p. 1101-1117.
- Burchfiel, B.C., Fleck, R.J., Secor, D.T., Vincelette, R.R., and Davis, G.A., 1974, Geology of the Spring Mountains, Nevada: *Geological Society of America Bulletin*, v. 85, p. 1013-1022.
- Carpenter, A.B., 1967, Mineralogy and petrology of the system CaO-MgO-CO₂-H₂O at Crestmore, California: *American Mineralogist*, v. 52, p. 1341-1363.
- Carr, M.D., 1978, Structure and stratigraphy of the Goodsprings District, southern Spring Mountains, Nevada [Ph.D. dissertation], Houston, Texas, Rice University, 155 p.
- Carr, M.D., and Pinkston, J., 1987, Geologic map of the Goodsprings District, southern Spring Mountains, Clark County, Nevada: U.S.G.S. Miscellaneous Field Studies Map MF-1514, scale 1:24000, 1 sheet.

- Cartwright, I., and Weaver, T.R., 1993, Fluid-rock interaction between syenites and marbles at Stephen Cross Quarry, Quebec, Canada: petrological and stable isotope data: *Contributions to Mineralogy and Petrology*, v. 113, p. 533-544.
- De Vivo, B., and Frezzotti, M.L., 1994, Fluid inclusions in minerals: methods and applications: Short Course of the Working Group (IMA) "Inclusions in Minerals," Virginia Polytechnic Institute and State University, 376 p.
- Deines, P., and Gold, D.P., 1969, The change in C and O isotopic composition during contact metamorphism of the Trenton Limestone by the Mount Royal pluton: *Geochimica et Cosmochimica Acta*, v. 33, p. 421-424.
- Ferry, J.M., 1989, Contact metamorphism of roof pendants at Hope Valley, Alpine County, California, USA: *Contributions to Mineralogy and Petrology*, v. 101, p. 402-417.
- Fletcher, P., 1993, *Chemical thermodynamics for Earth Scientists*: New York, John Wiley & Sons, 464 p.
- Fournier, R.O., 1985, The behavior of silica in hydrothermal solutions, *in* Berger, B.R., and Bethke, P.M., eds., *Geology and geochemistry of epithermal systems*: Society of Economic Geologists Reviews in Economic Geology, v. 2, p. 45-61.
- Gans, W.T., 1974, Correlation and redefinition of the Goodsprings Dolomite, southern Nevada and eastern California: *Geological Society of America Bulletin*, v. 85, p. 189-200.
- Gregory, R.T., Criss, R.E., and Taylor, H.P., 1989, Oxygen isotope exchange kinematics of mineral pairs in closed and open systems: applications to problems of hydrothermal alteration of igneous rocks and Precambrian iron formations: *Chemical Geology*, v. 75, p. 1-42.
- Gribble, C.D., and Hall, A.J., 1985, *A practical introduction to optical mineralogy*: Boston, George Allen & Unwin, 249 p.
- Goldstein, R.H., and Reynolds, T.J., 1994, Systematics of fluid inclusions in diagenetic minerals: *SEPM Short Course* 31, 199 p.
- Guilbert, J.M., and Park, C.F., Jr., 1986, *The geology of ore deposits*: New York, W.H. Freeman and Company, 985 p.
- Hazzard, J.C., 1937, Paleozoic section in the Nopah and Resting Springs Mountains, Inyo County, California: *California Division of Mines and Geology Bulletin*, v. 33, p. 273-339.

- Hazzard, J.C., and Mason, J.F., 1936, Middle Cambrian formations of the Providence and Marble Mountains, California: *Geological Society of America Bulletin*, v. 47, p. 220-240.
- Hedenquist, J.W., and Henley, R.W., 1985, The importance of CO₂ on freezing point measurements of fluid inclusions: evidence from active geothermal systems and implications for epithermal ore deposition: *Economic Geology*, v. 80, p. 1379-1399.
- Helgeson, H.C., Delany, J.M., Nesbitt, H.W., and Bird, D.K., 1978, Summary and critique of the thermodynamic properties of rock-forming minerals: *American Journal of Science*, v. 78-a, 229 p.
- Hershey, R.L., 1989, Hydrogeology and hydrogeochemistry of the Spring Mountains, Clark County, Nevada [M.S. Thesis]: Las Vegas, University of Nevada, 237 p.
- Hewett, D.F., 1931, Geology and ore deposits of the Goodsprings Quadrangle, Nevada: U.S. Geological Survey Professional Paper 162, 172 p.
- Hewett, D.F., 1956, Geology and ore deposits of the Ivanpah Quadrangle, Nevada and California: U.S. Geological Survey Professional Paper 275, 172 p.
- Holland, H.D., and Malinin, S.D., 1979, The solubility and occurrence of non-ore minerals, *in* Barnes, H.L., ed., *Geochemistry of hydrothermal ore deposits*: New York, John Wiley & Sons, 798 p.
- Holland, T.J.B., and Powell, R., 1990, An enlarged and updated internally consistent thermodynamic dataset with uncertainties and correlations: the system K₂O-Na₂O-CaO-MgO-MnO-FeO-Fe₂O₃-Al₂O₃-TiO₂-SiO₂-C-H₂-O₂: *Journal of Metamorphic Geology*, v. 8, p. 89-124.
- Holland, T., and Powell, R., 1991, A Compensated-Redlich-Kwong (CORK) equation for volumes and fugacities of CO₂ and H₂O in the range 1 bar to 50 kbar and 100-1600°C: *Contributions to Mineralogy and Petrology*, v. 109, p. 265-273.
- JCPDS, 1980a, Mineral Powder Diffraction File Search Manual: Joint Committee on Powder Diffraction Standards, International Centre for Diffraction Data, 484 p.
- JCPDS, 1980b, Mineral Powder Diffraction File: Joint Committee on Powder Diffraction Standards, International Centre for Diffraction Data, 1168 p.
- Kerrick, D.M., and Jacobs, G.K., 1981, A modified Redlich-Kwong equation for H₂O, CO₂, and H₂O-CO₂ mixtures at elevated pressures and temperatures: *American Journal of Science*, v. 281, p. 735-767.

- Klein, C., and Hurlbut, C.S., Jr., 1985, *Manual of mineralogy*: New York, John Wiley & Sons, 596 p.
- Kyle, B.G., 1992, *Chemical and process thermodynamics*: Englewood Cliffs, New Jersey, Prentice Hall, 567 p.
- Longwell, C.R., Pampeyan, E.H., Bowyer, B., and Roberts, R.J., 1965, *Geology and mineral deposits of Clark County, Nevada*: Nevada Bureau of Mines Bulletin, v. 62, 177 p.
- Nabelek, P.I., 1991, Stable Isotope Monitors, *in* Kerrick, D.M., ed., *Contact Metamorphism: Mineralogical Society of America Reviews in Mineralogy*, v. 26, p.396-435.
- Nabelek, P.I., Labotka, T.C., O'Neil, J.R., and Papike, J.J., 1984, Contrasting fluid/rock interaction between the Notch Peak granitic intrusion and argillites and limestones in western Utah: evidence from stable isotopes and phase assemblages: *Contributions to Mineralogy and Petrology*, v. 86, p. 25-34.
- Nesse, W.D., 1991, *Introduction to optical mineralogy*: New York, Oxford University Press, 335 p.
- Nordstrom, D.K., and Munoz, J.L., 1994, *Geochemical thermodynamics*: Boston, Blackwell Scientific Publications, 493 p.
- O'Neil, J.R., Clayton, R.N., and Mayeda, T.K., 1969, Oxygen isotope fractionation in divalent metal carbonates: *Journal of Chemical Physics*, v. 51, p. 5547-5558.
- Phillips, W.R., and Griffen, D.T., 1981, *Optical mineralogy: the non-opaque minerals*: San Francisco, W.H. Freeman and Company, 677 p.
- Powell, R., and Holland, T.J.B., 1985, An internally consistent thermodynamic dataset with uncertainties and correlations: 1. Methods and a worked example: *Journal of Metamorphic Geology*, v. 3, p. 327-342.
- Redlich, O., and Kwong, J.N.S., 1949, On the thermodynamics of solutions. V. An equation of state. Fugacities of gaseous solutions: *Chemical Reviews*, v. 44, p. 233-244.
- Robie, R.A., and Hemingway, B.S., 1995, *Thermodynamic properties of minerals and related substances at 298.15 K and 1 bar (10⁵ Pascals) pressure and at higher temperatures*: U.S. Geological Survey Bulletin 2131, 461 p.
- Secor, D.T., Jr., 1962, *Geology of the central Spring Mountains, Nevada* [Ph.D. dissertation]: Stanford, California, Stanford University, 152 p.

- Sverjensky, D.A., 1981, Isotopic alteration of carbonate host rocks as a function of water to rock ratio -- an example from the Upper Mississippi Valley Zinc-Lead District: *Economic Geology*, v. 76, p. 154-157.
- Taylor, B.E., 1986, Magmatic volatiles: Isotopic variation of C, H, and S, *in* Valley, J.W., Taylor, H.P., Jr., and O'Neil, J.R., eds., *Stable isotopes in high temperature geologic processes: Mineralogical Society of America Reviews in Mineralogy*, v. 16, p. 185-224.
- Taylor, B.E., 1987, Stable isotope geochemistry of ore-forming fluids, *in* Kyser, T.K., ed., *Short course in stable isotope geochemistry of low temperature fluids: Mineralogical Association of Canada Short Course Handbook*, v. 13, p. 337-445.
- Taylor, B.E., and Bucher-Nurminen, K., 1986, Oxygen and carbon isotope and cation geochemistry of metasomatic carbonates and fluids -- Burgell aureole, Northern Italy: *Geochimica et Cosmochimica Acta*, v. 50, p. 1267-1279.
- Taylor, H.P., Jr., 1974, The application of oxygen and hydrogen isotope studies to problems of hydrothermal alteration and ore deposition: *Economic Geology*, v. 69, p. 843-883.
- Taylor, H.P., Jr., 1977, Water/rock interactions and the origin of H₂O in granitic batholiths: *Journal of the Geological Society of London*, v. 133, p. 509-558.
- Tester, J.W., and Modell, M., 1997, *Thermodynamics and its applications: Upper Saddle River, New Jersey, Prentice Hall*, 936 p.
- Turner, F.J., and Weiss, L.F., 1965, Deformational kinks in brucite and gypsum: *Proceedings of the National Academy of Sciences in the United States of America*, v. 52, p. 359-364.
- Valley, J.W., 1986, Stable isotope geochemistry of metamorphic rocks, *in* Valley, J.W., Taylor, H.P., Jr., and O'Neil, J.R., eds., *Stable isotopes in high temperature geologic processes: Mineralogical Society of America Reviews in Mineralogy*, v. 16, p. 445-489.
- Walker, J.D., Beaufait, M.S., and Zelt, F.B., 1980, Cenozoic structural and volcanic history of the Devil Peak area, southern Spring Mountains, Nevada [Senior Thesis]: Cambridge, Massachusetts Institute of Technology, 29 p.

VITA

Graduate College
University of Nevada, Las Vegas

Rhonda Knupp

Home Address:

4857 Fiesta Way
Las Vegas, NV 89121

Degrees:

Bachelor of Science, Geology, 1994
Sonoma State University

Special Honors and Awards:

Scroungers Scholarship, 1994
Barrick Fellow, 1995
Bernada E. French Scholarship, 1995
Bernada E. French Scholarship, 1996

Publications:

Knupp, R.L, and Metcalf, R.V., 1997, Hydrothermal alteration associated with the Miocene Devil Peak intrusion, Clark County, Nevada: Geological Society of America Abstracts with Programs, v. 29, no. 6, p. 157.

Thesis Title: The origin of brucite in hydrothermally altered limestone near Devil Peak, Nevada

Thesis Examination Committee:

Chairperson, Dr. Rodney V. Metcalf, Associate Professor of Geology
Committee Member, Dr. Eugene I. Smith, Professor of Geology
Committee Member, Dr. Jean S. Cline, Associate Professor of Geology
Committee Member, Dr. Brett Riddle, Associate Professor of Biology

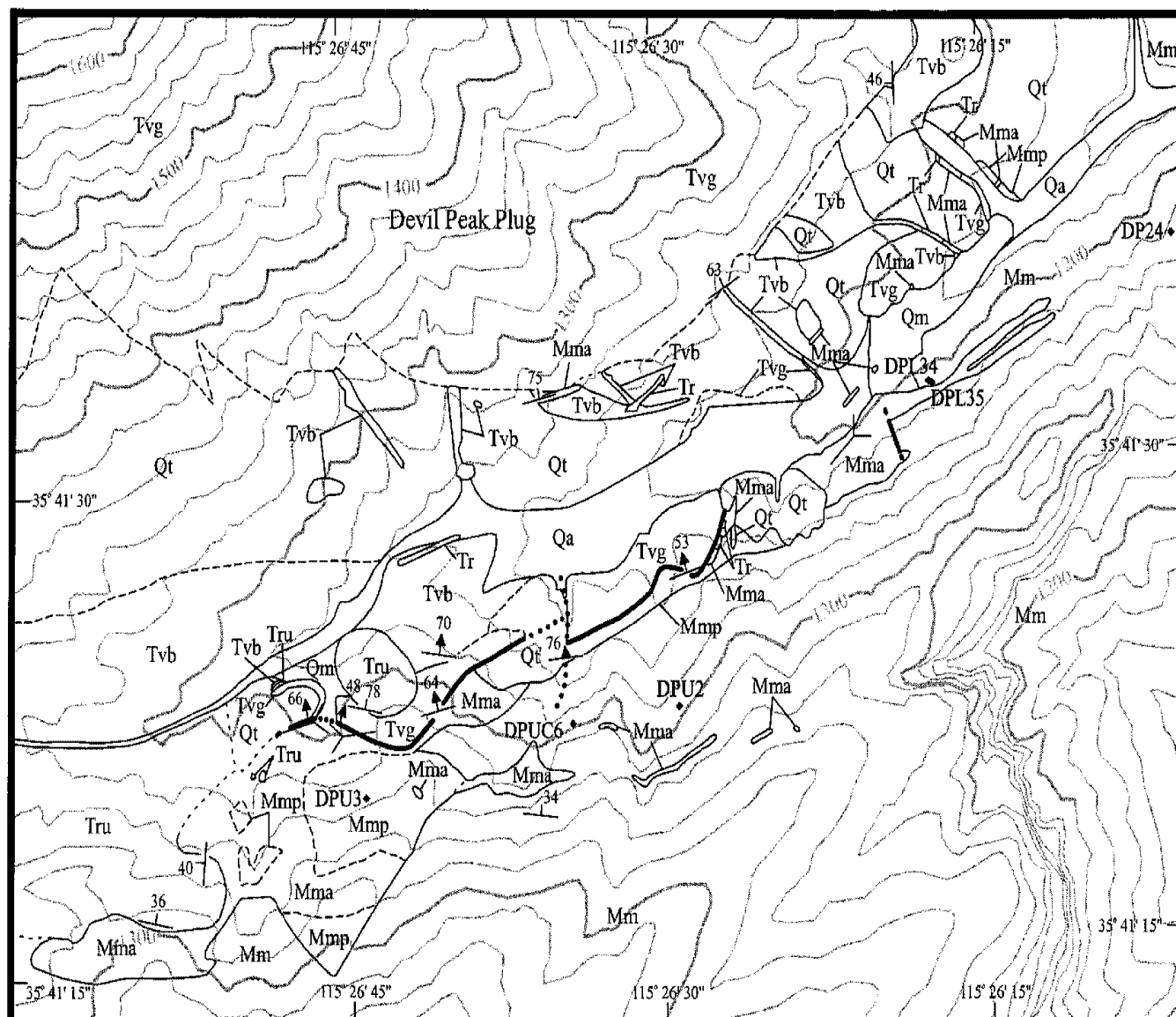
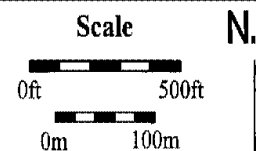


Plate 1. Geologic map of the southeast Devil Peak area. Base map U.S.G.S. State Line Pass 7.5-minute quadrangle. Contour interval 20 m.



Units		
Quaternary	Qm	man-made disturbance
	Qa Qt	alluvium, talus
Tertiary	Tru	red and brown rhyolite and rhyolite breccia
	Tr	intrusive rhyolite, undivided
	Tvb	gray debris flows and flow breccias
	Tvg	gray intrusive rhyolite
Mississippian	Mma	altered Monte Cristo Limestone
	Mmp	partly altered Monte Cristo Limestone
	Mm	Monte Cristo Limestone

Symbols	
/	contact
...	contact, approximately located
/	fault
...	fault, inferred
↗	strike and dip of beds
↗	strike and dip of contact
↗	strike and dip of fault plane
↗	trend and plunge of slickenlines

